University of California
Santa Barbara

Optical and Chemical Responses of Nanostructured Films

A dissertation submitted in partial satisfaction
of the requirements for the degree

Doctor of Philosophy
in
Chemistry

by

Jose Navarrete Jr

Committee in charge:

Professor Martin Moskovits, Co-Chair
Professor Galen D. Stucky, Co-Chair
Professor Stephen K. Buratto
Professor Javier Read de Alaniz
Professor Michael Gordon

September 2017

The Dissertation of Jose Navarrete Jr is approved.

Professor Stephen K. Buratto

Professor Javier Read de Alaniz

Professor Michael Gordon

Professor Galen D. Stucky, Committee Co-Chair

Professor Martin Moskovits, Committee Co-Chair

September 2017

Optical and Chemical Responses of Nanostructured Films

To my parents, Tina and Jose Navarrete. You made so many sacrifices to allow me to chase my dreams, I hope I've made you proud

Acknowledgements

This journey through many years of schooling would not have been possible without the support of my friends and family. With this in mind, I'd like to acknowledge all the people that have helped and supported me throughout my life to achieve this goal.

I'd like to start off by thanking those that inspired and believed in me starting with my time at Glen Rose High School. I'd like to thank Mandy Locke, my French and English teacher for multiple years. Your passion for teaching and your genuine interest in our success is something that has stuck with me throughout all these years. You never gave up on your students and you continued to challenge us to become our best selves. I can never thank you enough for all that you did. To my band director, Aaron Martin. I'm not sure if I can really put to words how you shaped me to become the person I am today. I hope your current and future students come to appreciate all that you teach them, you truly are an inspiring person and I'm forever grateful for our time together at Glen Rose. Many thanks to the friends at the LDL Foundation for your continuous support for all the students of Glen Rose High School. Your dedication and efforts with aiding students achieve their dreams goes unnoticed, you truly are an amazing organization.

To my friends at Texas State, y'all have been nothing short of amazing and supportive as I packed up my bags and headed to California for grad school. To my boys, "Los Primos", Gabe, Ty, and Xavi. We got to cheer together, be roommates, and share many crazy and fun memories. We've been through it all and I look forward to many more years of friendship. Love you guys.

To my friends at UCSB, you all made it worth it. First, many thanks to the wonderful postdocs I initially got to work with, Mubeen and Sylvia, for taking me under your wing. My journey would not have been possible without y'all. To my labmates, Tracy, Katherine, Katie, Will, and Brian. Slowly but surely, we made it through. I'll forever

cherish the memories we made whether it was ranting about life or chatting science, you are all amazing people and I can't wait to see what the future holds for all of you. Sean, Bi, Ryan, Zach, and Jimmy, we came in together and had some crazy times, it's been an amazing ride and I'm so grateful to have you all by my side throughout grad school.

To the Swole Patrol, Khoi, David, Belt, Dylan, Alphas, and Slayer. I had an awesome time training with you guys at the RecCen at UCSB! Khoi, you especially inspired me every day with your willingness to learn and positive attitude, you're going to do great things in graduate school! David, your calves were always a weakness but you always had a strong heart, keep it going! Stay strong guys! To my circle of Alphas, Kenny, Barnes, Christian, Matt, Edward, and Naveen. Good things always come to an end, but this was an end I never wanted to see. You guys have been amazing friends, support group, bagel and donut partners, golf buddies, and everything a guy would need of their friends. Whether we're kicking it during morning bagels, or eating lunch at nano, you guys were always there listening tentatively to my problems or were there to humble me by roasting me. You guys are freakin' awesome and I'm so glad UCSB brought us together. Each one of you have had such a huge impactment on my life and I will always cherish our time together.

A special thank you to my hairstylist Katherine. Getting a haircut and having my eyebrows waxed became a highlight when I started going to your salon. You're such a kind-hearted person and I'll greatly miss our shared talks and laughter.

To my UCSB cheer team. I've been with y'all since my first year of graduate school and it was such an honor to be your official coach for the last year. You all tested my patience and pushed me to the limit, but I wouldn't have traded y'all for anything in the world. It was an amazing ride and I'm beyond grateful that y'all let me be part of it. It was definitely hard leaving you guys as I move on to the next chapter of my life, but I know y'all are going to do amazing things.

To the California Allstars Rangers team. Coach Brandon and Didi, y'all embraced me from the start and were always supportive of my academic career. I'm sure to this day you still don't understand why I'm so weird, stubborn, and act the way I do, but just know that I have so much respect for all that you do and I look forward to another amazing year together. Ries, it was awesome to finally have met you after hearing so much about you from the countless athletes you have coached. You truly are an amazing and inspiring person and it was such an honor and pleasure to share the mat with you this past year. I love you so much and I can't wait to make countless more memories, this upcoming year will definitely be one for the ages! Adrian, Randy, Nathan, Mitch, Justin, Emily, Kimberly Anne, Jesus, Iliana, Sara, and Annagail, thank you for all the amazing memories this past year. We definitely started from nothing and made it into something truly special. The eight stitches on my face (thanks Annagail), getting hit trying to catch y'all in pyramids, and countless hours driving was worth it for all of you. Love you all so much.

To some special friends. Scott and Lauren, we started our journey together as roommates and neighbors during our time at Texas State. It's no coincidence we all ended up on the west coast together. Y'all always treated me as family and were always there for me during my early struggles of graduate school. It really means so much to have friends like you in my life that are constantly supporting and encouraging me to be the best I can be. I can never thank you enough. It was an honor to be part of your wedding day and I look forward to many years of happiness together. Love y'all! Brandon and Emily, we met through interesting circumstances and it's been such a blast since then. We've been through tough times together, but we've always managed to pull through and make the best of every situation. No matter what I was going through, you always filled me with positivity and support. Thank you for making me a big part of your lives by always welcoming me as one of your own. I knew I could always turn to you with anything and

you would be there to do everything in your power to help me. I can't thank you enough for all that you've done for me. Love the both of you so much.

Sam and Chris, my two undergraduates. Y'all are freakin' amazing and I don't know what I would have done without y'all. Chris, you were always positive and excited about everything and you never ceased to amaze me with your skills, you are going to do amazing things at Stanford and I look forward to reading about your successes. Sam, I had so much fun working alongside you and I'm sure you'll never understand it but you really are an amazing and talented young man. Keep working hard and best of luck to whichever graduate school you decide to attend.

To my advisor, Professor Martin Moskovits. Your patience and genuine care for not only your students but others as well, is something that I will always greatly admire. It has been an absolute honor working alongside you. I honestly could not have made it through graduate school without your support. Anytime I was down about an experiment or lack of results, you would always patiently guide me and do whatever you could to help me get back on track. I never felt alone on this journey knowing I had an advisor like yourself. Thank you for everything and I hope I make you proud.

Lastly, to my family. To my seesters, Mimi and Kitty, you are the best sisters I could ever ask for. You truly are my best friends and I love you so much. We've supported each other through our times during and after college. You always checked up on me to make sure I was surviving and always made sure I was happy. Love you both so much. My parents, Jose and Tina, you made so many sacrifices for me to make it this far. You would take on second jobs to support me and the sisters during our time in college. I know it's been a rough ride, but I hope you can look back and not regret a single second of it. Through it all, I did all this for you as I hope to give you the future you've always dreamed about. We did this journey together, I love you so much and I can't wait to enjoy the rest of our lives together.

I'm not able to individually address everyone, but thank you to anyone that I have met during my time at Texas State and UCSB. I've made some amazing memories and I'm so grateful I got to share it with all of you. Thank you and Eat 'em up Cats and Go Gauchos!

Curriculum Vitæ

Jose Navarrete Jr

Education

2017	Ph.D. in Chemistry, University of California, Santa Barbara Co-advisors: Professors Martin Moskovits and Galen D. Stucky *Optical and Chemical Responses of Nanostructured Films*
2012	B.S. in Chemistry, Texas State University-San Marcos Advisor: Professor William J. Brittain *Functionalization of SiO_2 nanoparticles with spiropyran derivatives*

Research Experience

University of California-Santa Barbara

Investigated optical properties of plasmonic nanocomposites by effective-medium approximations through fabrication and modeling

Fabricated thin film oxide back-gated transistors for studies of surface chemistry reactions

Developed a novel method for sputtering patterned oxides at substrate temepratures > 500 K to significantly lower leakeage currents and minimize substrate damage

Texas State University-San Marcos

Optimized synthetic and charaterization platform for clicked sprioprayan derivates onto silica nanoparticles

Developed a 'draw and compute' interface for molecular dynamics and DFT calculations of conductive polymers

Mentor Experience

Head mentor for students in the California Alliance for Minority Participation (CAMP) and UC-Leadership Excellence Through Advanced Degrees (UCLEADS) Program

Directly mentored Christopher Siefe, now a graduate student in the Materials Department at Stanford, and Samuel Alcantar, currently applying to graduate schools

Publications, Posters, and Presentations

Navarrete, J., Siefe, C., Alcantar, S., Belt, M., Stucky, G.D., Moskovits, M. (2017). Merely measuring the UV-Vis spectrum of gold nanoparticles can change their charge state. *submitted*

Elucidating nano-electrostatics through effective-medium approximations, University of California Chemical Symposium, Los Angeles, California, March 2017

Lee,W., **Navarrete, J.**, Evanko, B., Stucky, G.D., Mubeen, S., Moskovits, M. (2016). A plasmonic liquid photovoltaic cell with greatly improved power conversion efficiency. *Chem. Comm.*, 52(92), 13460-13462

Sarkar, D., Xie, X., Kang, J., Zhang, H., **Navarrete, J.**, Moskovits, M., Banerjee, K. (2015). Functionalization of transition metal dichalcogenides with metallic nanoparticles: Implications for doping and gas-sensing. *Nano Letters*, 15(5), 2852-2862

Emerging Frontiers in Plasmonics: Nanostructures for Solar Energy Conversion and Catalysis, 3rd International Conference on Frontiers of Plasmonics, Xiamen, China, April 2014

Departmental Service

Head committee member for the 3rd Annual Chemistry Graduate Student Symposium, 2014
Head committee member for the Chemistry Student Seminar Series, 2013-2015
Volunteer, Materials Research Laboratory, 2013
Committee member for the 2nd Annual Chemistry Graduate Student Symposium, Spring 2013
Commitee member for the Chemistry Student Seminar Series, 2012

Awards

Center for Science Partnerships (CSEP) Outstanding Graduate Student Mentor, UCSB, Spring 2016
Outstanding Service to the Chemistry Department, UCSB, Spring 2016
Best Poster, 3rd International Conference on Frontiers of Plasmonics, Xiamen, China, April 2014
Partnership in International Research and Education in Electron Chemistry and Catalysis at Interfaces Fellow, UCSB, August 2013-2015
Smith-Whelms College of Science Award, Texas State, May 2011
Outstanding Junior Chemistry Major, Texas State, May 2011

Abstract

Optical and Chemical Responses of Nanostructured Films

by

Jose Navarrete Jr

When illuminated with visible light, nanostructured noble metals exhibit a strong plasmon resonance at wavelength, λ_p, that has been shown to be sensitive to its size, structure, the dielectric properties of the surrounding medium, and charge density. The tunability of the plasmon resonance has allowed metal nanosystems to be fabricated with resonances matching the solar spectrum for us in plasmon promoted catalysis, plasmonic photovoltaics, and surface-enhanced raman spectroscopy. Here we use UV-Visible spectroscopy to track the shifts of the plasmon resonances from an array of gold nanoparticles buried under metal oxide layers of varying thickness when in contact with one of two bulk metals: aluminum or silver. By assuming the array of gold nanoparticles and metal-oxide layers to be an optically homogenous film of core-shell particles on a substrate, we developed a Maxwell-Garnett effective medium approximation to extract reliable optical parameters for the gold nanoparticles, yielding their charge state before and after contact with the bulk metal.

Based on the optical parameters extracted from our model, we find the magnitude of charge transfer from the bulk metal to the gold nanoparticle is independent of the work function of the bulk metal. Furthermore, when gold is used as the bulk layer in contact with the gold nanoparticles, we measured an appreciable amount of charge transfer to the gold nanoparticles, failing to support the well-established model for electrostatic contact electrification. Instead, we attribute the charge transfer to the so called plasmoelectric effect, an optically induced charge transfer mechanism, in which the gold nanoparticle

modifies its charge density to allow its resonant wavelength to match that of the incident light. We show, however, that in our devices the Schottky barriers between the metals and the metal oxide layers create a rectification effect that favors electron transfer from the bulk metal to the nanoparticles over the reverse effect.

Contents

Chapter 1

Introduction

When illuminated with visible light, nanostructured noble metals exhibit a strong plasmon resonance at a wavelength λ_p, Figure 1.1 and Figure 1.2. [1, 2]. The effect on λ_p of size [3, 4], geometry [2, 5], surrounding medium [6], and electrochemical charging [7, 8] have beeen well documented and the agreement between experiment and theory is generally very good. The above-mentioned tunability has allowed metal nanosystems to be fabricated with resonances matching the solar spectrum and subsequently used in plasmon promoted catalyis [9], surface-enhanced raman spectrosocopy [10], and the development of plasmonic photovoltaics [11, 12]. More recently, shifts in λ_p were observed on metallic nanostructures due to an optically induced change in carrier density [13], further expanding the functionality and applicability of metallic nanostructures.

In short, we will be utilizing the plasmonic properties of gold nanoparticles to explore various applications including the development of an optical model that utilizes the Maxwell-Garnett effective medium approximation to describe the optical response of thin film composite comprised of gold nanoparticles and various metal oxide dielectric materials. This model was then used as a method of probing the electronic state of the gold nanoparticles when in electrical contact with various bulk metals to eluci-

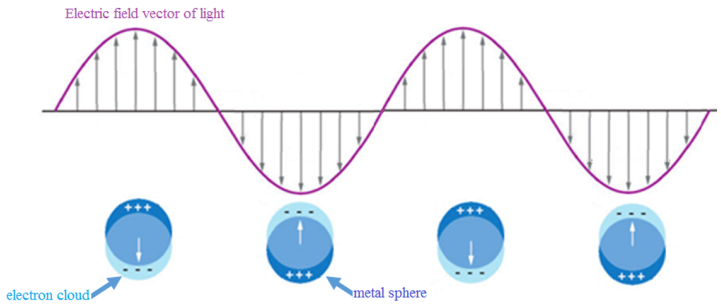

Figure 1.1: The collective oscillation of conduction electrons in a nanostructured metal sphere in phase with incident light.

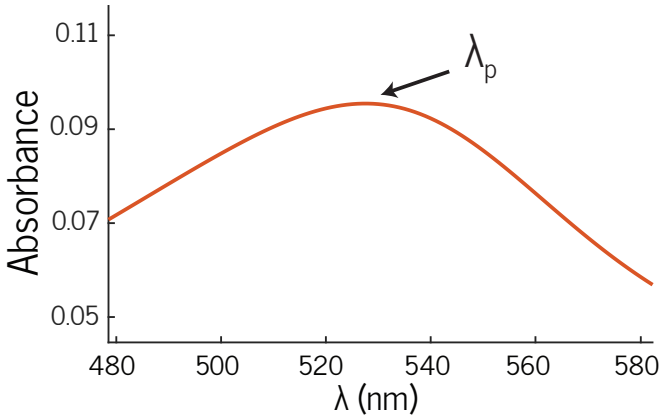

Figure 1.2: UV-Visible spectra illustrating the position of the absorbance maximum as a result of the plasmon resonance of noble metals within the visible spectrum.

date the electrostatic effect of bulk metals within nanometer range of gold nanoparticles, showing that classical electrostatics will fail to predict charge transfer when coupling plasmonic nanoparticles with bulk materials. Finally, we will lay the groundwork towards the development of an electronically controlled heterogenous catalytic platform where we demonstrate what appears to be a layer thickness dependent behavior towards oxidizing and reducing gases.

Scope of this thesis

Optical modeling of plasmonic thin film composites

We first report the optical properties of nanostructured media comprised of gold nanoparticles buried under nano-layers of dielectric (TiO_2, SiO_2, Al_2O_3). By developing an effective medium model in which the gold/dielectric phase is assumed to be a Maxwell-Garnett film comprised of core-shell particles, we are able to extract reliable optical parameters by UV-Vis spectroscopy from which the electron density in the gold nanoparticles is realiably determined. We determined that there is no measureable charge transfer occurring between the gold nanoparticle and the dielectric medium and show that our model holds for layer thicknesses of the dielectric oxide up to 10 nm.

Elucidating charge transfer dynamics through surface plasmon resonance and MG-EMA

When metallic nanoparticles are placed in electrical contact with other materials, such as metal-oxide or metallic films, charge redistribution between the participating material takes place to allow the Fermi energies of the participating materials to be equal. [14–16]. Choosing materials with either higher or lower Fermi energy levels relative

to the energy level of the nanoparticle, it is possible to charge the nanoparticle positively or negatively. Furthermore, it has been shown experimentally that the magnitude of the charge redistribution is proportional to the difference in the Fermi energy levels between the work functions of the nanoparticle and the contacting materials [17], allowing one to modify, in this way, the electronic properties of the nanoparticle for possible applications in catalysis and plasmonics.

Here, we show that under illumination, we find the charge transfer to the gold nanoparticles from the metallic bulk layer to be independent of the bulk metal's work-function, thus rejecting an explanation based on a purely electrostatic approximation in which the difference of energy levels of the constitutent materials is the primary mechanism for charge redistribution in the system. Instead, the major mechanism for charge accumulation can be successfully attributed to the plasmoelectric effect in which the charge transfer is favored towards from the bulk metal to the nanoparticle, thereby inducing an overall net negative charge on the particle. We attribute this net negative charge to the Schottky barriers within between the metals and the metal oxide layers creating a rectification effect that favors electron transfer from the bulk metal to the nanoparticles over the reverse effect.

Towards a gate-tunable heterogenous catalytic platform

Inspired by prior research group members where they showed the kinetics of surface reactions on a tin oxide nanowire can be modified by an external gate potential when the nanowire is configured as a field-effect transistor, we sought to expand this idea to a TiO_2 thin film transistor where we hope to control heterogenous catalytic reactions by simply tuning the charge density of the thin film through the gate potential.

We show for layer thicknesses between 15-25 nm of TiO_2, deposited through various

methods including thermal oxidation of titanium, atomic layer deposition, and sputter deposition, that the films exhibit unusual behavior in that oxygen gas appears to be reducing its surface, significantly contradicting the known properties of TiO_2. We show this no longer is the case for sputtered TiO_2 films of thickness greater than 50 nm. Furthermore, upon configuring a 20 nm TiO_2 film into a field-effect transistor, we determined there was no significant or obvious difference in its electronic properties from that of significantly thicker layers. These properties have led us to believe there must be some physical parameter that has not yet either been considered or well understood that is influencing such anomlous behaviors at ultrathin regimes.

Chapter 2

Optical modeling of plasmonic thin film composites

2.1 Introduction and background information

The optical and electrical properties arising from mixtures of metallic nanostructures and dielectric media have allowed for unique properties not possible from their pure constitutents. By tailoring the volume fractions of the participating materials, it has become possible to obtain a wide range of properties simply by changing the relative amounts of each materials. A particular colorful example is that of medieval era staind glass resulting from metallic particles embedded in the transparent material as shown by the SEM micrograph in Figure 2.1.

Although quite apparent to a user with a powerful imaging technique such as SEM, there was much debate as how to approximate the optical response of such mixtures. Then, in 1904, Maxwell Garnett developed a theoretical solution which was eloquently simple but immensly powerful to describe the a complex mixture, such as metallic structures within a film, as a homogenous effective medium. [19] The formula, so-called the

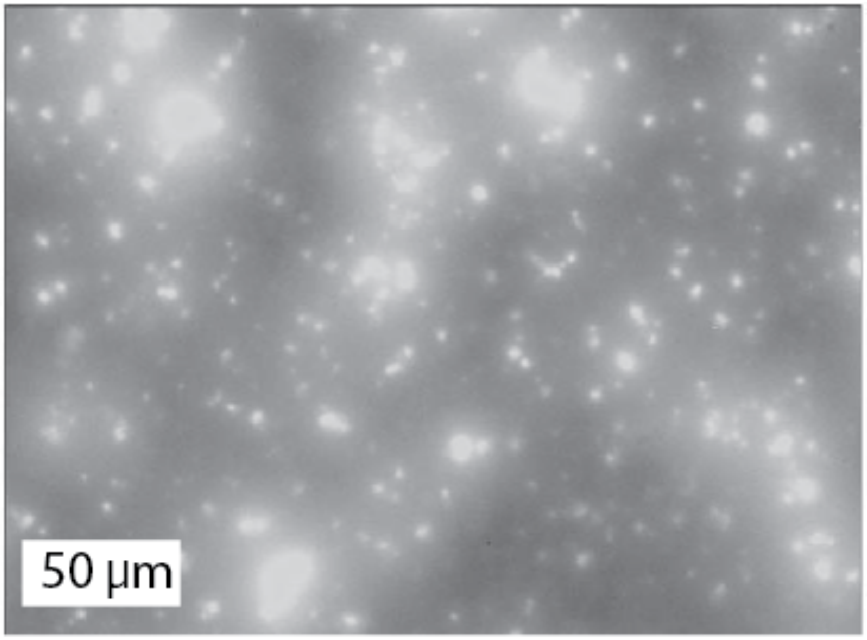

Figure 2.1: SEM micrograph of staind glass. Reprinted with permission from [18].

Maxwell Garnett effective medium approximation, simply allowed one to calculate the effective permittivity (effective medium) of a complex mixture solely based on the volume fractions of the individual constituents within the complex solution or film. There exists an extensive amount of literature regarding the derivation and applicability of the Maxwell-Garnett approximation, therefore only the major keypoints and topics will be discussed.

The Maxwell-Garnett effective medium approximation for arbitrary spherical inclusions within a host media yields the following equation,

$$\epsilon_{MG} = \epsilon_h \frac{1 + 2f\frac{\epsilon_i - \epsilon_h}{\epsilon_i + 2\epsilon_h}}{1 - f\frac{\epsilon_i - \epsilon_h}{\epsilon_i + 2\epsilon_h}}, \tag{2.1}$$

where ϵ_h is the effective dielectric function of the host medium, ϵ_i is the dielectric function of the inclusions within the host medium, and f is the volume fraction of the inclusions

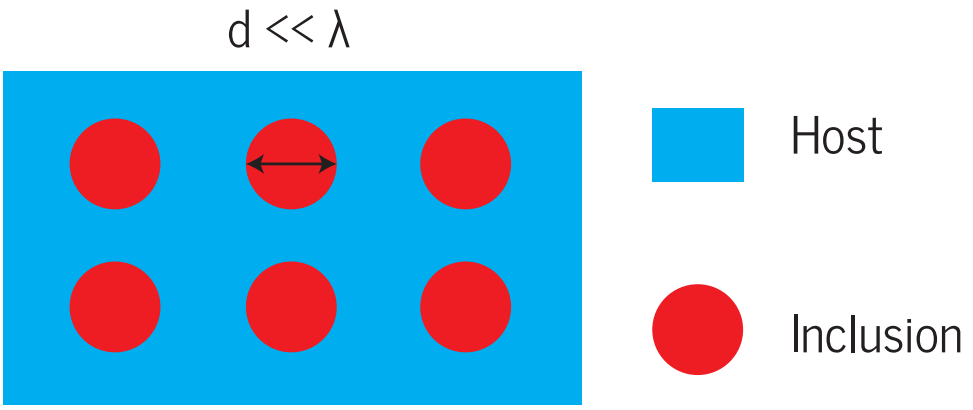

Figure 2.2: Top view schematic for a Maxwell-Garnett film where the spherical inclusions are of diameter d and are significantly smaller than the wavelength of light, λ.

within the host medium.

In Equation 2.1, the expression $\frac{\epsilon_i - \epsilon_h}{\epsilon_i + 2\epsilon_h}$ is in fact the polarizability of a sphere in a host medium, given by,

$$\alpha = 4\pi r^3 \frac{\epsilon - \epsilon_h}{\epsilon + 2\epsilon_h}, \tag{2.2}$$

where Equation 2.2 explicitly considers the volume of the individual sphere, while Equation 2.1 contains the volume term within the volume fraction f.

Equation 2.2, known as the Clausius-Mossotti relation or the Lorentz-Lorenz equation, derives from the Lorentz molecular theory of polarization where the system considers a collection of point-like polarizable atoms to describe the dielectric function of the material. [20, 21] This relationship was discovered independently by Lorentz and Lorenz while an analogous formula for static fields describing insulators was derived by Clausius and Mossotti. [22]

While both approaches stem from very different first principles, they both achieve the ability to compute the the macroscopic dielectric function of a mixture made up of inclusions (spheres, disk, whatever shape one chooses). The effective medium approximations are most effective when the inclusions are significantly smaller than the wavlength light

being used to investigate the system, as illustrated in Figure 2.2.

Equation 2.1 can be rearranged to the following form:

$$\frac{\epsilon_{MG} - \epsilon_h}{\epsilon_{MG} + 2\epsilon_h} = f\frac{\epsilon_i - \epsilon_h}{\epsilon_i + 2\epsilon_h}, \tag{2.3}$$

where if we assume the composite mixture contains inclusions made of different materials with permittivities ϵ_n $(n = 1, 2, .., N)$, can generalize as,

$$\frac{\epsilon_{MG} - \epsilon_h}{\epsilon_{MG} + 2\epsilon_h} = \sum_{n=1}^{N} f_n\frac{\epsilon_n - \epsilon_h}{\epsilon_n + 2\epsilon_h}. \tag{2.4}$$

This allows one to consider a composite of multiple components.

While there are many examples using Maxwell-Garnett approximation, I will primarily focus on a few examples that have laid the groundwork for our proposed devices.

As demonstrated by Charles R. Martin and co-workers, the Maxwell-Garnett approximation was able to some-what successfully describe the optical properties of a metal-insulator composite comprised of varying metal volume fractions prepared by depositing gold into porous aluminum oxide membranes. [23] Although close inspection of their measured spectra and calculated spectra may cause one to claim invalidates to the Maxwell-Garnett approach, they showed the spectra was somewhat consistent considering the large gold particles (on the order of 0.3 to 3 microns) relative to the wavelength of the incident light and the interparticle spacing was relatively large. This becomes important when considering significant scattering effects, an effect not considered by the Maxwell-Garnett approach. They also claim that the infrared spectra are not completely amenable to the quasi-static approach approximation, an approximation that states that if the particle dimensions and their mutual separation distances are small relative to the wavelength of light, scattering effects can be considered negligible. This was confirmed by the inabil-

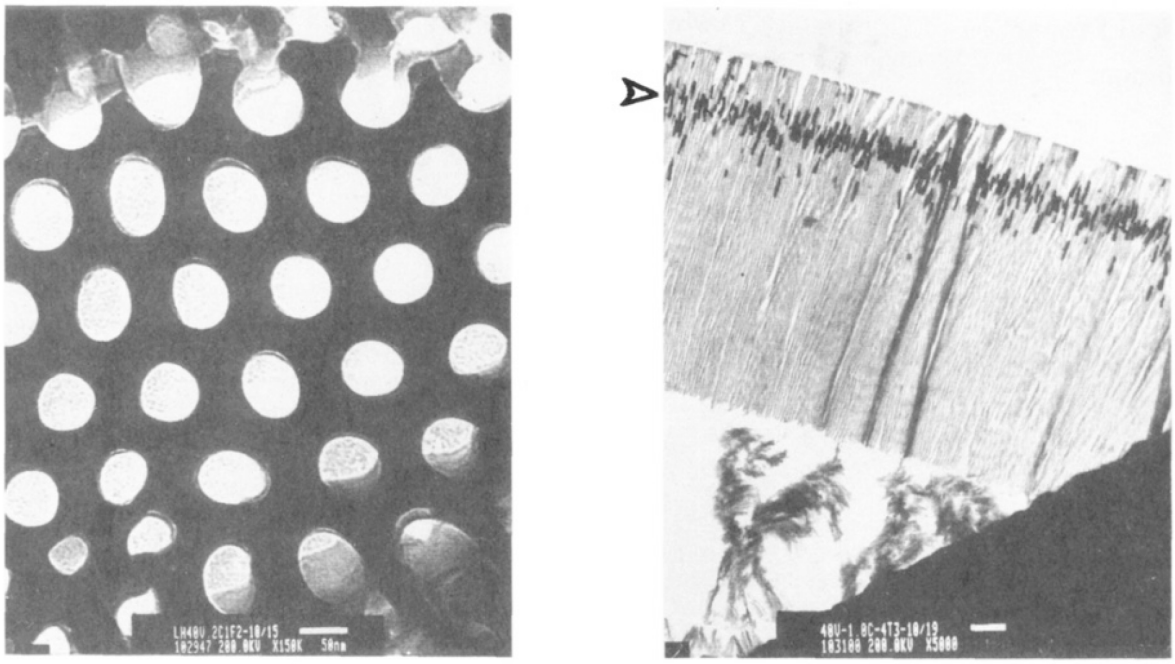

Figure 2.3: Alumina template by Charles R. Martin and co-workers. [24]

ity to match the Maxwell-Garnett calculation to their measured spectra with infrared radiation. Therefore, to circumvent the issues with such large nanoparticles relative the incident wavelength, they prepared an anodic template with significantly smaller pores, on the order of 50 nm diameter pores. [24] With significantly smaller gold dimensions, they were able to successfully prepare a composite of gold and porous alumina template that can be tuned to various levels of optical transparencies within the visible spectrum, Figure 2.3. They were then able to to confirm these spectra were in agreement with the predictions of Maxwell-Garnett, thus confirming their prior hypothesis that reducing the dimensions of the metallic componenet would yield significantly better agreement with the Maxwell-Garnett approximation, shown by Figure 2.4.

The worked demonstrated by Martin and coworkers showed that Maxwell-Garnett is an appropriate approximation for calculating the optical spectra of metal/dielectric composites. Their work demonstrated the following:

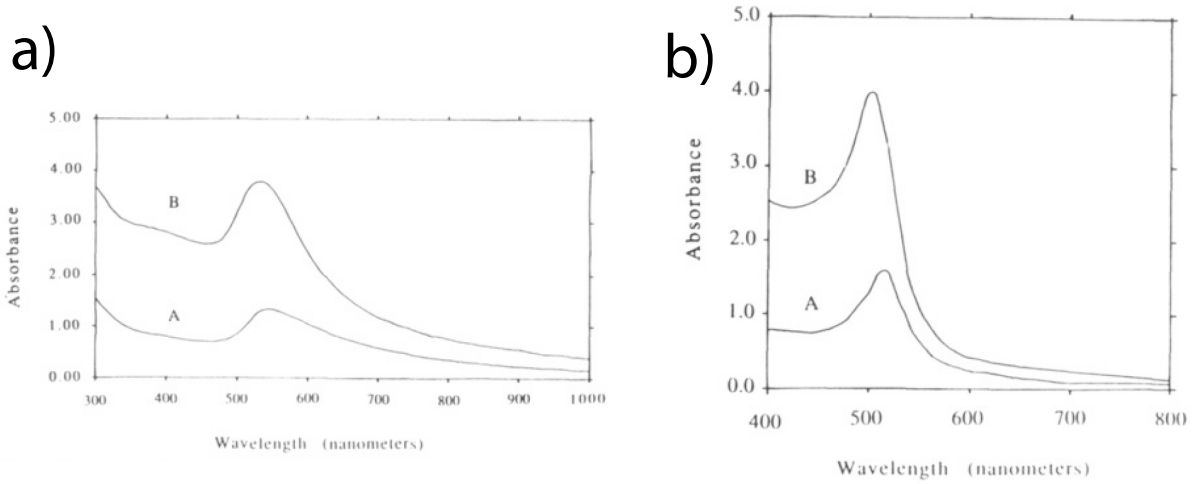

Figure 2.4: a) Measured and b) calculated spectra of metallic spheres adapted from [24]

1. Maxwell-Garnett will most effectively predict optical spectra in the visible region when using particles significantly smaller than the wavelength of light, up to 50 nm, as expected by the criteria laid out with previous studies.

2. Maxwell-Garnett will underestimate the transmittance when using structures on the order of microns for infrared radiation, due to the scattering and coupling effects between the structures.

3. They claim the approximation will yield the best fits when the particle is less than $0.16\times\lambda_p$, there λ_p is the wavelength of maximum absorption of the particle.

In more recent studies, Demir and coworkers studied the extinction of ceria@silica (ceria core, silica shell) hybrid particles embedded in polystyrene composites, Figure 2.5. [25] In this work, they were able to successfully lower scattering by attempting to index match the core ceria to the polystyrene material with a silica shell.

While the scattering processes and their results are outside of the scope of this thesis, they demonstrated that the Maxwell-Garnett approximation successfully accounted for their measured spectra when considering the system to be a set of core-shell particles

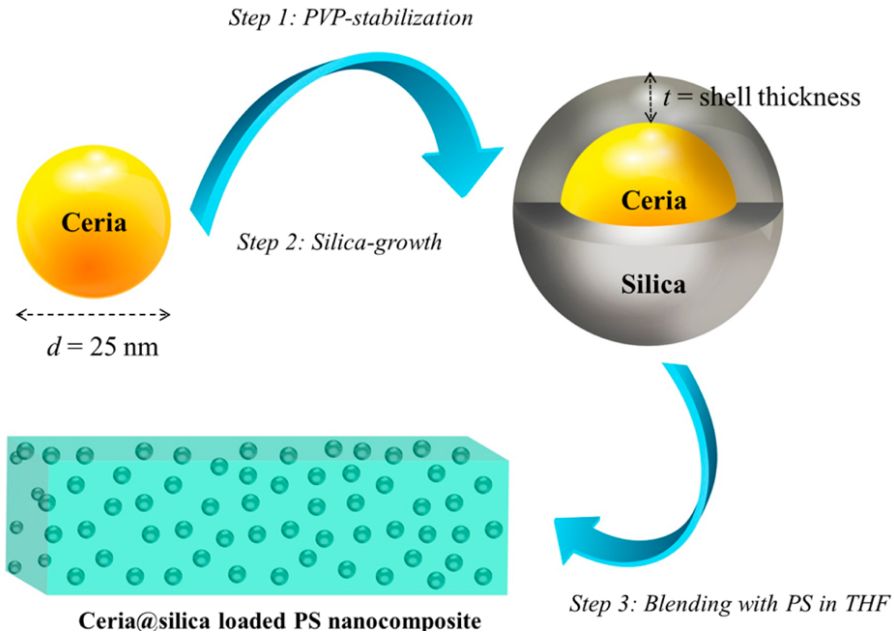

Figure 2.5: Schematic illustrating the core-shell particles embedded in polystyerene. Adapted from [25]

embedded in polystyrene. This core-shell type configuration will be of great use as we will also require such an approximation for our system.

Moving forward with our configuration, we wish to study composite films fabricated by foundry friendly techqniques with a 'bottom up' approach, as in, we will begin with a bare substrate and grow all constituents from this substrate, whereas a 'top down' approach typically begins with all constituents in place and selective etching is used to define features and isolate devices.

A schematic of the sample we will investigate is shown in Figure 2.6. The device architecture consists of gold nanoparticles grown on a quartz substrate, followed by deposition of one of three oxides, Al_2O_3, SiO_2, or TiO_2. The sample will be analyzed by UV-Vis spectroscopy and the Maxwell-Garnett approximation will be employed for modeling the system.

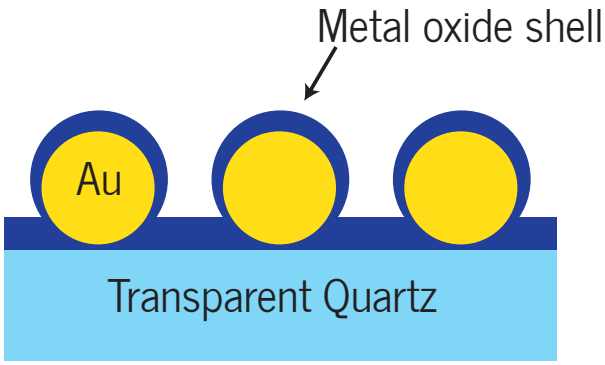

Figure 2.6: Basic schematic of proposed device; include are gold nanoparticles with a metal oxide shell on a transparent quartz substrate.

2.2 Device fabrication and methods

All films under investigation in this thesis work were grown on quartz substrate 1.7 mm thick. High quality quartz is typically greater than 99% transparent in the visible region while having minimal loss throughout the ultraviolet spectrum. Before dicing, the 5×5 cm quartz plate was coated with LOL 2000 (a lift off layer typically used in lithography processes) on both sides. No hot bake was required as the LOL 2000 adhered quite nicely to the quartz substrate, furthermore, we wanted the LOL 2000 to be removed as easily as possible in later steps after dicing. Quartz substrates were diced into 1×1.5 cm pieces and cleaned throughouly in acetone, isopropanol, and deionized (DI) water. If residual LOL 2000 was left after the solvent cleanings, soaking in NMP Rinse (commercial photoresist stripper) at 50 °C would properly remove the residual layer. Although further solution phase techniques are typically employed to ensure the surface of the quartz is free of contamination, we found these further solution cleaning processes did not have a significant impact on the quality of the spectra we obtained. Upon final DI rinse quartz substrates were plasma cleaned in an oxygen descum chamber (Gasonics) in 300 mTorr oxygen at 100 W substrate bias power to ensure any organic residues were removed. Substrates were then placed on 110 °C hotplate in a photolithography hood to remove

any residual water for the surface.

Substrates were then immediately mounted to the carrier plate for electron beam deposition of the gold nanparticles. Samples could be left in storage for weeks without seeing an negligible degradation of the optical spectra. A thin gold film of 2 nm mass thickness was deposited by electron beam evaporation at a rate of 0.1 Å/s. Electron beam evaporation was done on a Temescal electron beam evaporation system. The system has a home-built load-lock system that allows for quick pumping between samples with approximately 5×10^{-8} torr ultimate base pressure, although typically base pressures tend to be at around 9×10^{-7} torr. Overnight pumping would really be required to achieve the ultimate base pressure, although there is not significant difference film quality when depositing at the base pressure mentioned above. It was critical to perform the deposition at a slow rate to ensure large 'globs' would not form on the surface. This was noticed when we initially attempted to deposit gold at 1.0 Å/s causing unreproducible gold depositions. Therefore, by carefully ramping the electron beam until the desired rate is achieved, reproducible substrates were obtained. Upon the completion of the gold deposition, substrates were annealed at 500 °C for 10 minutes in 5 slm N_2 in a rapid thermal annealing tool (RTA) by AET . Although the RTA tool could achieve high anneal ramp rates, we choose a 10 minute ramp up time to the annealing setpoint to minimize any thermal stresses on the materials due to high ramp rates.

As can be seen in Figure 2.7, there is a significant difference in the morphology of the gold nanoparticles from the as-deposited film to the annealed film. When initially deposited, the gold film tends to form what appears to be an irregular array of islands lacking uniform size and shape dispersed throughout the substrates. However, upon annealing, the film transforms from irregular shaped islands to nanoparticles evenly disperesed throughout the substrate. This technique for forming naoparticles has been used by others in our lab and continue to be a simple and clean method for fabricating

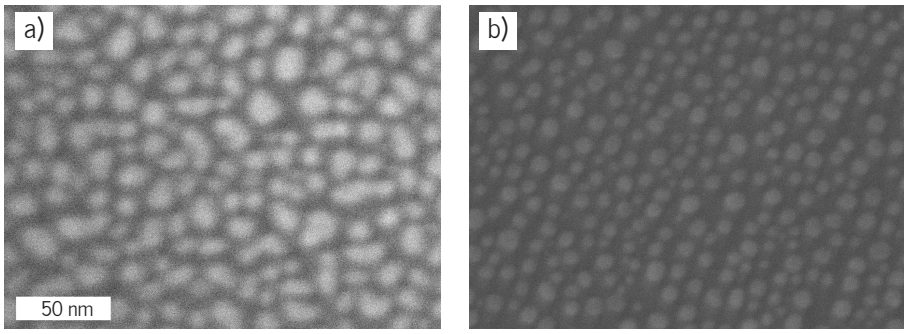

Figure 2.7: SEM micrograph of 2 nm mass thickness gold deposited by e-beam evaporation a) before annealing and b) after annealing at 500 °C for 10 minutes in 5 slm N_2 yielding in gold particles with radius ≈5nm.

nanoparticles on the surface. [26] Although we are employing a non-traditional method for fabricating gold nanoparticles, this technique has been shown has a suitable method for depositing gold nanoparticles for plasmonic photovoltaics, therefore not making it competely absolete if ever needed for such technologies. [27] No further surface treatments were performed on the gold nanoparticles upon annealing.

Upon annealing the gold nanoparticle on quartz substrates, the samples were loaded onto a 6 inch Si carrier wafer. If the carrier wafer appeared to be very worn from many ALD uses, one could run about 30 cycles of whichever ALD recipe was being used for deposition. This prevented any unwanted flaking of the carrier wafer during deposition on to the active substrates as these flakes could potentially land on the substrate and destroy the surface.

The ALD provided in the nanofab at UCSB is the FlexAl Atomic Layer Deposition system from Oxford Instruments. This system is capable of performing plasma-enhanced depositions as well as water based depositions for for the precise growth of ultra-thin oxides and nitrides. Growing films by ALD allows for the self-limiting layer by layer growth process which ensure we have very reproducible film qualitty. Although the system can accommodate sample temperatures up to 550 °C we chose to run our depositions at 300

°C as other users in the nanofab have reported this to be the best and most reproducible temperature for growth with the ALD system. Furthermore, the staff at the nanofab has done a pretty nice job with making sure the growth rates and film quality quite stable. ALD was also chosen due to its demonstrated conformal coverage of nanostructures for deposited layer thicknesses down to 1 nanometer. Other deposition techniques, such as e-beam, sputtering, and plasma-enhanced chemical vapor deposition (PECVD), tend to follow nucleated growth mechanisms that tends to not fair well with nanostructured materials. Although some e-beam deposition techniques have been shown to have ideal surface coverage. With all these considerations, ALD was the obvious choice due to its many ideal properties. Although the substrate temperature of 300 °C can cause issues if one chooses to use photolithography procedures to define deposition areas on their substrate since the resist can decompose and contaminate the deposition chamber, there have been demonstrations of using a hard-mark technique using a silicon nitride and chromium mask to define feature and has been shown to be stable up to 600 °C.

For the work presented in this dissertation, we will be focusing on three metal-oxides available on the ALD system: TiO_2, SiO_2, Al_2O_3. Although all three of these materials are used as dielectrics for insulating purposes, they actually afford a wide range of electrical and optical properties from which we can choose. TiO_2 has a high index of refraction, approximately 2.4 at 633 nm wavlengths, and has a relatively high relative static dielectric constant of approximately 80 and a wide bandgap of approximately 3.2 eV. [28] SiO_2 has a relatively low index of refraction of approximately 1.5-1.6, static dielectric constant of 3.9 and bandgap of 1.1 eV. Al_2O_3 has a large 7.0 eV bandgap, static dielectric constant of 9, and an index of refraction of approximately 1.76. The absolute value for these above mentioned properties can vary extensively depending on the deposition parameters, the source quality, substrate temperature, etc. Variations for all will not be addressed in this work, but will be mentioned when such issues arise throughout device fabrication and

analysis. Details regarding the growth process such as organometallic precursors, growth rate, and index of refraction can be found in the appendix.

For all of the above mentioned oxides, layer thickness ranging from 1.5 to 7 nm was deposited onto the gold nanoparticle substrates. Ellipsometric measurements to determine oxide layer thickness was obtained from both a bare silicon monitor wafer and a wafer with a Au/Ti layer (3000/100 Å). We did this to ensure there were no significant differences in the growth rates between the silicon wafer, from which the standard process was characterized, and the bare gold substrate (since we are growing on gold nanparticles). Ellipomsetry (JA Woolam Inc.) confirmed similar growth rates although the indices of refraction varied slightly from the gold and silicon substrates. The model used for fitting was a Cauchy transparent optical model that follows, $n(\lambda) = A + \frac{B}{\lambda^2} + \frac{C}{\lambda^4} + ...$, where n is the refractive index, λ, is the wavelength, and A, B, C, are coefficients determined empirically. The model used was provided by the nanofab staff during the qualification of the Oxford ALD instrument. Details for the Cauchy parameter and the ellipomsetry program used for fitting can be found in the appendix. Furthermore, the Woolllam software provided powerful methods for developing an optical model based on unique architectures and materials, something to consider when developing novel optical materials. Note to users who will be using ALD deposition: although it's not advised to develop recipes different from the standrard recipes provided by the staff, due to possible accidental contamination and writing recipes incorrectly, some users change the standard recipe. Issues have come up a few times when a user will improperly adjust a recipe and cause the deposition to give terrible quality films. Therefore, for critical depositions where you're limited in samples and need to be completely sure the deposition will yield proper films, it is suggested running a test deposition on a silicon monitor wafer that will yield a few nanometers of the desired material. Confirm deposition by ellipomsetry and ensure the index of refraction and growth rates follow those provided

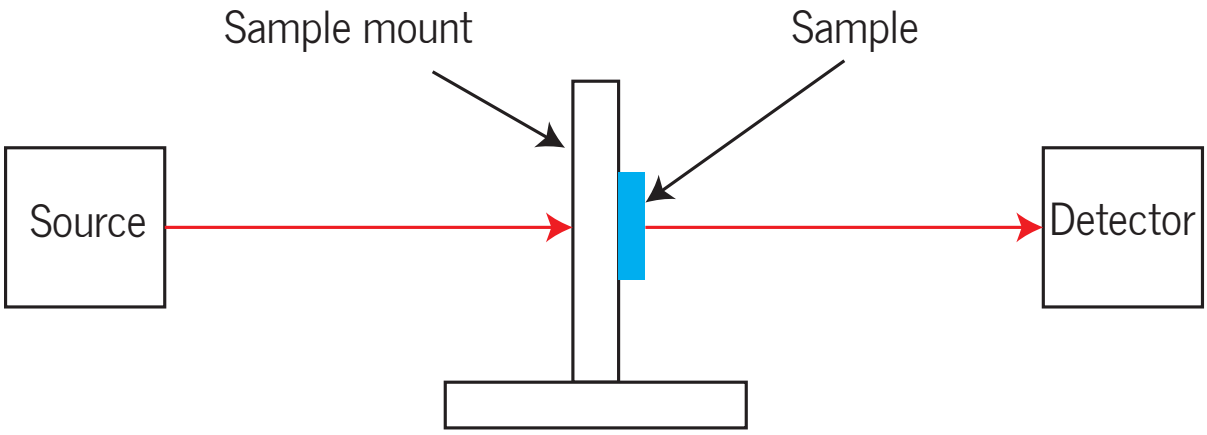

Figure 2.8: Simplified schematic of optical path for transmission measurements, not shown are the internal components of the spectrometer which include the chopper, several optical elements, and the reference beam.

by the standard recipes. This practice will also ensure there is plenty of metal-organic precurors as the film quality will begin to significantly deviate when the precursor bottles are nearing low levels.

Deposition of the oxides will yield a significant color change on the gold substrates, something that should be of no surprise due to the visible activity of the gold nanoparticles. Visual inspection of uniformity can confirm whether the deposition was a success as you can see 'blotches' across the substrate if the growth did not proceed successfully. These film imperfections appear to occur randomly, haven't really been able to pinpoint exactly what causes the poor quality deposition. Furthermore, once all the film thicknesses and index of refraction have been confirmed by measuring the film grown on the silicon wafer by ellipsometry, transmission measurements were obtained for all samples (Varian Cary 500 UV-Vis-NIR spectrometer), Figure 2.8.

Spectra were then fitting using a Matlab based least squares program where the fit adjusted primarily in the region dominated by the plasmon resonance of the gold nanoparticle (550-720 nm), details of the fit will be discussed in the results section.

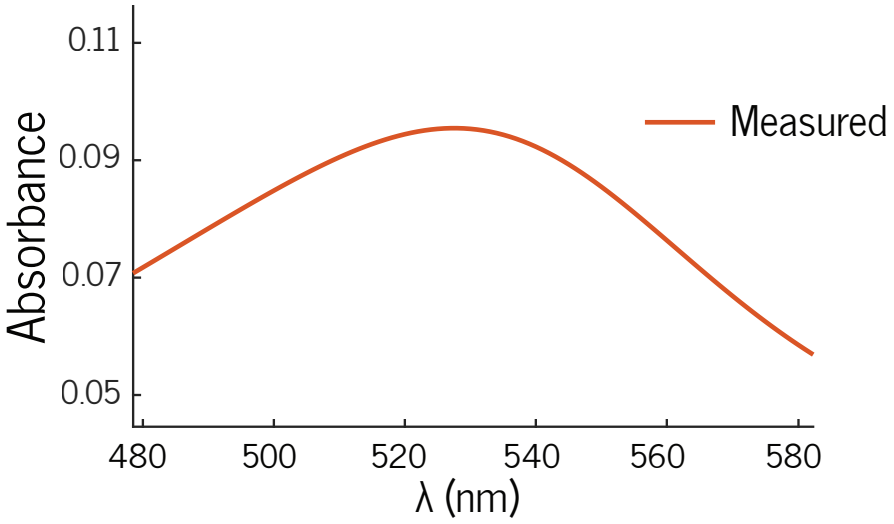

Figure 2.9: UV-Vis spectra of r = 5 nm bare gold nanoparticles on 1.7 mm quartz substrates exhibiting a strong resonance at approximately 525 nm wavelength.

2.3 Results and Discussion

To set forth a baseline for our modeling program, we begin by analyzing bare gold nanoparticles on a quartz substrate as mentioned in the methods section. We first obtained a spectra for our bare gold nanoparticles on the quartz substrate. These particles were approximately 10 nm in diameter and were well dispersed on the substrate, as confirmed in Figure 2.7.

A strong plasmon resonance is observed at approximately 525 nm, agreeing with prior observations for the resonance of gold on similar substrates. Not surprising, this resonance was relatively strong considering only a film of 2 nm mass deposited gold was used, this can be attributed to the the relatively close packing of the gold nanoparticles on the substrate, even if their total layer thickness is on the order of 10 nm.

Maxwell-Garnett effective medium aproximation for bare Au-NPs

We will now develop the model for the bare gold nanoparticles. As mentioned beforehand, a prerequisite for using the Maxwell-Garnett effective medium approximation is

that the inclusion, in this case, the Au-NPs, must be significantly smaller than the wavelength of light being used to interrogate the film. This requisite prevents the light from 'seeing' two separate phases if the inclusion becomes large, therefore, eliminating the use of an effective medium to describe the optical properties of this film. These requisites are shown in Figure 2.2. For our system, the gold nanoparticles are approximately 10 nm in diameter, and are not percolating (well dispersed and not in contact with one another), allowing the film to be described as a Maxwell-Garnett film.

To determine the effective dielectric function of the effective medium film comprised of the gold nanoparticles in air, we first begin with the generalized Maxwell-Garnett equation, [29]

$$\left(\frac{\epsilon_{eff} - \epsilon_h}{\epsilon_{eff} + \kappa\epsilon_h}\right) = f\left(\frac{\epsilon_i - \epsilon_m}{\epsilon_i + \kappa\epsilon_m}\right) \tag{2.5}$$

where ϵ_{eff} is the effective complex dielectric function of the film, ϵ_h is the dielectric function of the host media (in this case, air), ϵ_i is the dielectric function of the inclusion (Au-NPs), κ is the screening parameter, and f is the volume fraction of the inclusion in the host. The screening parameter, κ, is related to the Lorentz depolarization factor, L, given by,

$$\kappa = \frac{(1 - L)}{L}.$$

The screening parater is determined by the shape and the orientation of the nanoparticles with respect to the external electric field. Since our particles are spherical, $L = 1/3$ and $\kappa = 2$. However, for long elliptical cylinders, their orientation with respect to the external field becomes significantly more important as the depolarization factor approaches close to zero when the cyclinder is oriented along the electrical field. This then simplifies Equation 2.5 to the following,

$$\left(\frac{\epsilon_{eff} - \epsilon_{air}}{\epsilon_{eff} + 2\epsilon_{air}}\right) = f\left(\frac{\epsilon_{Au} - \epsilon_{air}}{\epsilon_{Au} + 2\epsilon_{air}}\right) \tag{2.6}$$

The complex dielectric function for gold, ϵ_{Au}, can be expressed as follows,

$$\epsilon_{Au}(\omega) = 1 - \frac{\omega_p^2}{\omega^2 + i\omega\gamma} + \sum_j^N \frac{a_j}{\omega_{0j}^2 - \omega - i\omega\Gamma_j} + \epsilon_\infty. \tag{2.7}$$

The function consists of a drude term describing the contribution of the conduction electrons, a number of Lorentzians which account for the contribution of interband transitions primarily to the UV-Vis region of the spectrum and a constant accounting for the trailing contribution from transitions in the far UV. The plasma frequency, ω_p, is the bulk metal frequency and γ the scattering rate in the Drude model. The bulk metal plasma frequency, ω_p, is related to the electron density in the nanoparticle, N, as follows,

$$\omega_p^2 = \frac{Ne^2}{m\epsilon_0}, \tag{2.8}$$

and m is the effective mass of the electron, e is the elementary charge, and ϵ_0 is the permittivity of free space. The dielectric function for air (ϵ_{air}) is assumed to be equal to unity. The values for the Lorentzian sums were fitted versus the optical constant values provided by Johnson and Christy and are provided in the Appendix A.1. [30]

Upon solving for the effective dielectric function for the nanoparticle/air film, one obtained a complex dielectric function of the following form, $\tilde{\epsilon}(\omega) = \epsilon_1 + i\epsilon_2$. This complex dielectric function is then converted to its complementary complex index of refraction, $\tilde{n} = n - ik$, as follows,

$$n = \sqrt{(\epsilon_1 + \sqrt{(\epsilon_1^2 + \epsilon_2^2)})/2} \tag{2.9}$$

$$k = \sqrt{(-\epsilon_1 + \sqrt{(\epsilon_1^2 + \epsilon_2^2)})/2}, \tag{2.10}$$

to formulate the complex index of refraction for the effective medium film as $\tilde{n} = n - ik =$

$\tilde{n}_{MG}$ in Figure 2.11. Although not shown, it is important to note that, generally, both n and k are strongly dependent on the frequency of the light, therefore, a more complete expression can be written as $\tilde{n}(\omega) = n(\omega) - ik(\omega)$. The complex index of refraction of air, $\tilde{n}_{Air}$ is assumed to be 1, and the complex index of refraction of quartz, $\tilde{n}_{quartz}$, is assumed to be 1.50. Lacking an imaginary component for the complex index of rerfraction for both air and quartz indicates that both materials are lossless in the spectral region of interest.

For a two layer system with incident light normal to the interface, illustrated in Figure 2.10, the Frensel coefficients as well as the reflectance, R, and transmittance, T, can be written as,

$$r_{12} = \frac{n_1 - n_2}{n_1 + n_2} \tag{2.11}$$

$$t_{12} = \frac{2n_1}{n_1 + n_2} \tag{2.12}$$

$$R = |r|^2 \tag{2.13}$$

$$T = \frac{n_2}{n_1}|t|^2. \tag{2.14}$$

Since all of our measurements are performed with light at normal incidence to the interface, there is no need to designate the polarization (s or p). General formulas for the Frensel coefficients at angles other than normal to the interface and for particular polarizations can easily be found in the literature. [22]

However, the reflectance and transmittance of our system, comprised of several layers, becomes a little more complex. We first begin by addressing the individual Fresnel coefficients for reflections at the interface and propagation through the layer. When the complex index of refraction for the materials shown in Figure 2.11 are known, assuming

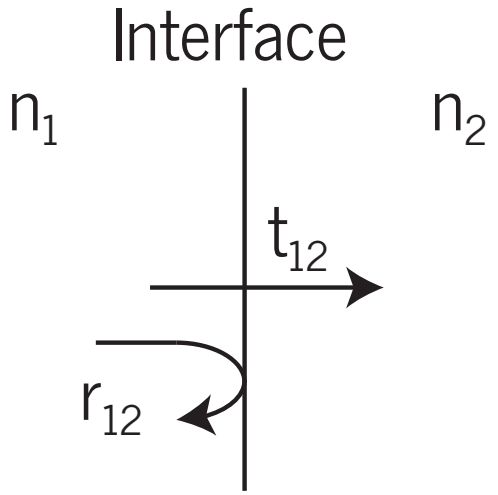

Figure 2.10: Schematic of a two layer system with light at normal incidence to the interface between two materials of index refraction, n_1 and n_2.

normal incidence the Fresnel coefficients can be expressed as follows,

$$r_{12} = \frac{n_1 - n_2}{n_1 + n_2} \tag{2.15}$$

$$r_{23} = \frac{n_2 - n_3}{n_2 + n_3} \tag{2.16}$$

$$r_{34} = \frac{n_3 - n_4}{n_3 + n_4} \tag{2.17}$$

$$t_{12} = \frac{2n_1}{n_1 + n_2} \tag{2.18}$$

$$t_{23} = \frac{2n_2}{n_2 + n_3} \tag{2.19}$$

$$t_{34} = \frac{2n_3}{n_3 + n_4} \tag{2.20}$$

When considering wave propagation through a multilayer stack, the transfer matrix formulation can be used to simplify the calculation and allow one to easily calculate the transmittance and reflectance for a multilayer stack. [31] The general transmission (T_{ij})

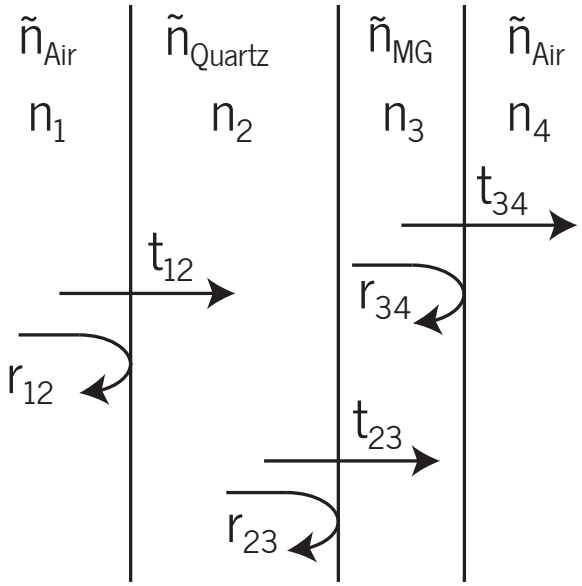

Figure 2.11: Schematic illustrating the propagation of light various transmission (through the layers) and reflection (at boundaries) Fresnel coefficients needed for accurately describing the optical properties of these films. The subscripts indicate the layer numer order sequentially from left to right where air is assumed to be infinite.

matrix for a wave between two layers, i and j, is given by,

$$T_{ij} = \frac{1}{t_{ij}} \begin{bmatrix} 1 & r_{ij} \\ r_{ij} & 1 \end{bmatrix} \tag{2.21}$$

where t_{ij} and r_{ij} are the complex reflection and transmission Fresnel coefficients for layers i and j. For a wave propagating through layer i is given by,

$$T_i = \begin{bmatrix} e^{j\phi} & 0 \\ 0 & e^{-j\phi_i} \end{bmatrix} \tag{2.22}$$

where

$$\phi_i = \left(\frac{2\pi L_i}{\lambda} \right) \tilde{n}_i \cos\theta_i, \tag{2.23}$$

and L_i is the length of propagation through layer i, $\tilde{n}_i$ is the complex index of refraction

of layer i and θ_i is the angle of propagation through layer i.

Multilayered systems can be constructed simply by matrix multiplying the basic components shown above for each layer interface and propagation through layers to yield a transmission matrix of the following form,

$$T = \begin{bmatrix} T_{11} & T_{21} \\ T_{21} & T_{11} \end{bmatrix} \tag{2.24}$$

which can be converted the more useful scattering matrix, S, by the following relationship,

$$S = \begin{bmatrix} S_{11} & S_{21} \\ S_{21} & S_{22} \end{bmatrix} = \frac{1}{T_{11}} \begin{bmatrix} T_{21} & \det T \\ 1 & -T_{12} \end{bmatrix} \tag{2.25}$$

where now, $r_{12} = S_{11}$, $t_{12} = S_{21}$, $r_{21} = S_{22}$, and $t_{21} = S_{12}$, thereby simplifying the calculation for transmittance and reflectance. Further analysis and examples can be found in Chapter 3 of *Diode Lasers and Photonic Integrated Circuits* by Larry Coldren and coworkers. [31]

A Matlab least squares script was used for fitting the spectra data obtained from UV-Vis where the least squares minimization was performed in the spectral region where the plasmon resonance of the gold nanoparticle dominated for a MG film of thickness $d = 2 \times r$, where r is the radius of the nanoparticle.

As shown in Figure 2.12, the agreement between the measured and calculated spectra track very nicely with no significant deviations from the measured spectra. The parameters of primary interest are those pertaining to the complex dielectric function of the gold nanoparticle, in particular, ω_p, a measure of the charge density of the material, and γ, a measure of the resistivity of the metal due to bulk and surface scattering effects. The dielectric function is shown below again for reference.

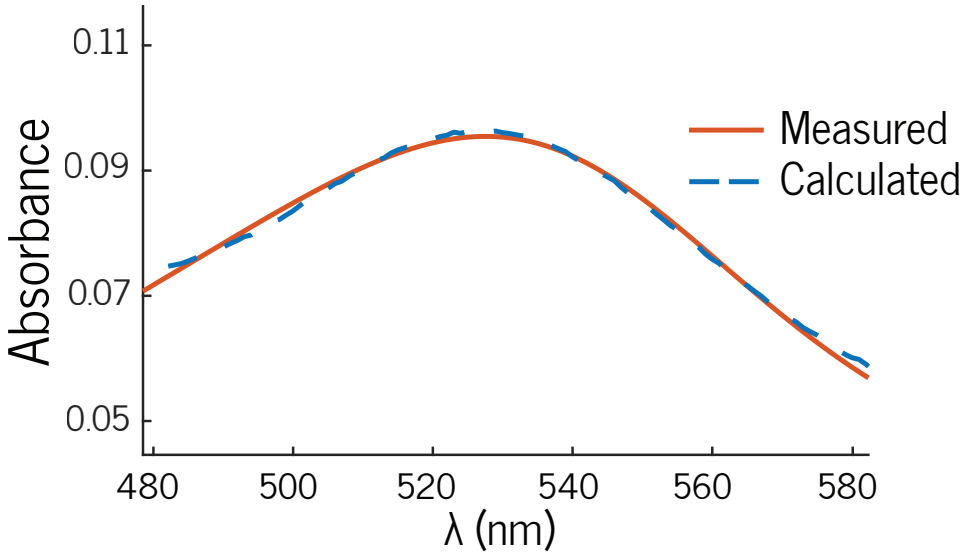

Figure 2.12: Least squares minimization assuming a Maxwell-Garnett effective medium film of a layer comprised of an array of 10 nm diameter gold nanoparticles on quartz.

$$\epsilon_{Au}(\omega) = 1 - \frac{\omega_p^2}{\omega^2 + i\omega\gamma} + \sum_j^N \frac{a_j}{\omega_{0j}^2 - \omega - i\omega\Gamma_j} + \epsilon_\infty$$

From the proposed model assumming the array of gold nanoparticles to be a Maxwell-Garnett effective medium film, values of ω_p and γ were determined to be 8.99 eV and 0.281 eV, respectively. The value obtained for ω_p of 8.99 eV reasonably agrees with the bulk value for gold, 9.1 eV. However, value for γ was exctracted for our system, showed significant deviation from the bulk value of γ for gold, 0.0757 eV. The scatteing parameter, γ, can be written as follows,

$$\gamma = \frac{\nu_F}{l}, \tag{2.26}$$

where ν_F is the Fermi velocity of the material and l is the electron mean free path for the material. Although not obvious from above, γ exhibits a size dependency that will strongly affect the imaginary component of the dielectric function, which is the dominant

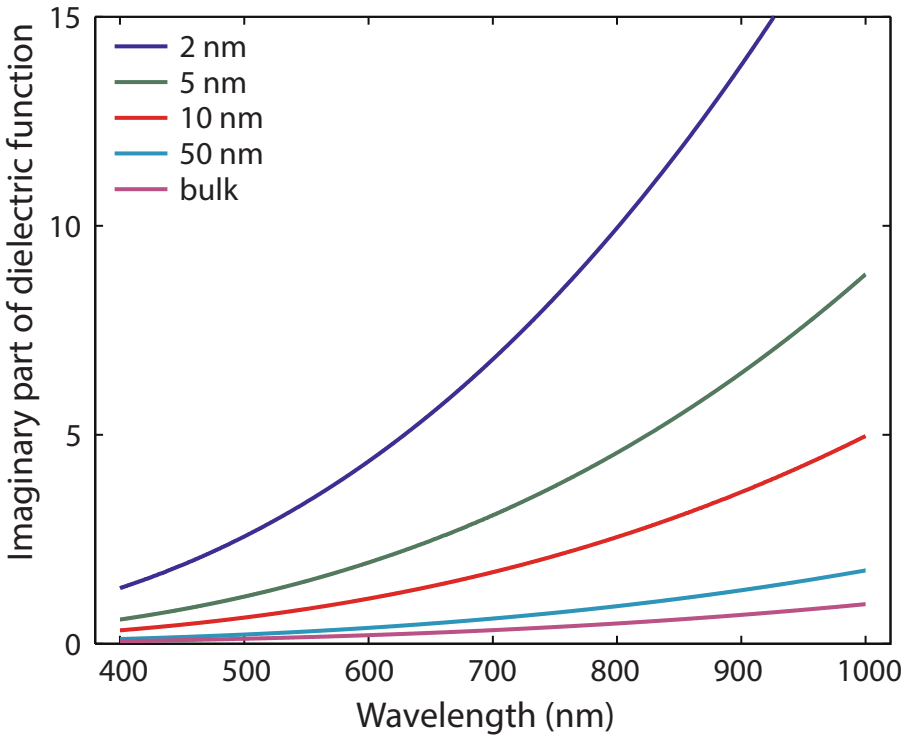

Figure 2.13: Size dependency of the imaginary component of the dielectric function for silver. Reprinted with permission from *Optical Metamaterials* by Shalaev and Cai. [29]

component of the dielectric function attributed to the interaction with optical frequencies for noble metals.. The imaginary component of the dielectric function can be shown by expansion of the complex dielectric function, assuming a Drude model with contributing interband transitions, as follows:

$$\epsilon(\omega) = \epsilon'_\omega + i\epsilon'_\omega = \epsilon_\infty - \frac{\omega_p^2}{\omega^2 + i\gamma\omega} = \epsilon_\infty - \frac{\omega_p^2}{\omega^2 + \gamma^2} + i\frac{\omega_p^2\gamma}{\omega\left(\omega^2 + \gamma^2\right)} \tag{2.27}$$

As shown in Figure 2.13, there is a clear dependency of the imaginary component of the dielectric function with respect to the size of the noble metal. This increase in the imaginary component when the metal is nanostructured is due to the change in γ. As mentioned beforehand, γ, is a measure of the scattering rate (damping, resisitivity, etc.) that needs to be size corrected when the metal is structured to the order of 10's of nm's.

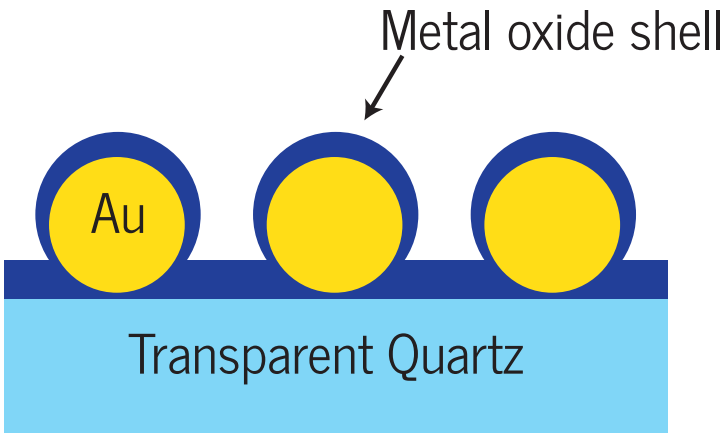

Figure 2.14: Basic schematic of proposed device; include are gold nanoparticles with a metal oxide shell on a transparent quartz substrate.

Therefore, γ can be corrected as follows,

$$\gamma = \gamma_B + A\frac{\nu_F}{R}, \tag{2.28}$$

where γ_B is the bulk scattering rate, R is the nanoparticle radius, and A is a geometrical parameter taken to be unity for spherical nanoparticles, giving a value of 0.256 eV for a nanoparticle of 5 nm radius, in close agreement with the 0.281 eV obtained through our model. When accounting for the approximations and assumptions made with this system, the model does a sufficiently adequate job of describing the effective layer while extracting meaningful values of ω_p and γ.

Now that the proposed model has shown to be adequate to accurately describe the spectra of bare Au-NPs, we wish to expand this model to a system comprised of Au-NPs buried under nano-layers of atomic layer deposited (ALD) metal-oxides.

As mentioned in the methods, we chose three metal-oxides, TiO_2, SiO_2, and Al_2O_3, to yield a structure schematically shown in Figure 2.14.

We first began by fabricating samples consisting of either 2 nm of Al_2O_3, TiO_2, or 1.5 nm of SiO_2 deposited onto an array of 5 nm radius gold nanoparticles on a quartz

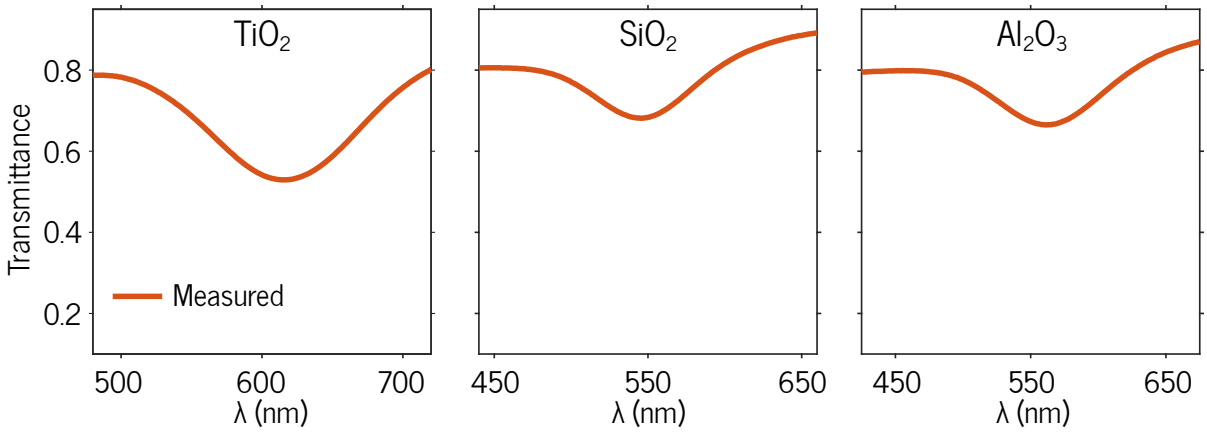

Figure 2.15: Measured spectra consisting of gold nanoparticles with its respective metal-oxide shell.

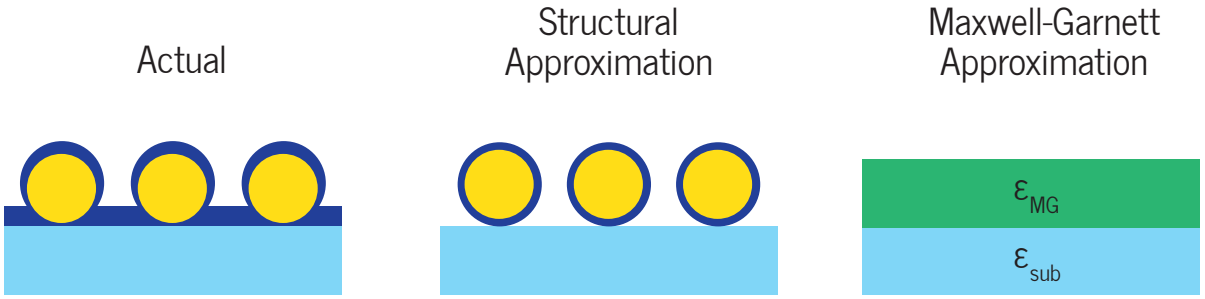

Figure 2.16: Structural approximation used to reduce the Au-NP and metal-oxide film to an array of core-shell nanoparticles on a quartz substrate.

substrate. The resulting spectra are shown in Figure 2.15.

The system becomes slightly more complex as now we have two inclusions (Au-NP and metal-oxide layer) that must be taken into account with the Maxwell-Garnett approximation. Unfortunately, the Maxwell-Garnett approximation only considers one inclusion into a host media. Although we could use the Bruggememan effective medium approximation, where one can take any sum of inclusions as long as their volume fractions are known, we chose to instead, perform a structural approximation to simplify the nanoparticle/metal-oxide phase to an array of core-shell nanoparticles on a quartz substrate, illustrated by Figure 2.16.

By allowing the nanoparticle/metal-oxide phase to be approximated as an array of core-shell nanoparticles, we can follow a similar method as used for the bare Au-NPs. The effective dielectric function, ϵ_{MG}, for the Maxwell-Garnett film composed of gold nanoparticles and the oxide coating as seen in Figure 2.16, is given by,

$$\epsilon_{MG} = \epsilon_m \left(\frac{1 + 2f_{cs}\ \beta}{1 - f_{cs}\ \beta} \right), \tag{2.29}$$

where ϵ_m is the dielectric function of the host media (air, silver, or aluminum), f_{cs} is the volume fraction of the core (ϵ_1) - shell (ϵ_2) particle within the host medium, and β, which is proportional to the polarizability, α, of the Au/dielectric core-shell particles is defined by the following equation,

$$\alpha = r^3 \frac{(\epsilon_2 - \epsilon_m)(\epsilon_1 + 2\epsilon_2) + f(\epsilon_1 - \epsilon_2)(\epsilon_m + 2\epsilon_2)}{(\epsilon_2 + 2\epsilon_m)(\epsilon_1 + 2\epsilon_2) + f(2\epsilon_2 - 2\epsilon_m)(\epsilon_1 - \epsilon_2)} = r^3\beta. \tag{2.30}$$

where ϵ_2 (the dielectric function of the metal-oxide shell) is assumed to be constant within the region of interest. The volume fraction f, not to be confused for the volume fraction used for the Maxwell-Garnett expression (f_{CS}), is the volume fraction of the core within the core-shell defined as, $f = \frac{(r_1)^3}{(r_2)^3}$, where r_1 is the radius of the gold nanoparticle and r_2 is the sum of the radius of the nanoparticle and the layer thickness (t) of oxide deposited. Therefore, if $f = 1$ (gold nanoparticle), Equation 2.30 reduces to,

$$\alpha = \frac{\epsilon_1 - \epsilon_m}{\epsilon_1 + 2\epsilon_m} \tag{2.31}$$

and when $f = 0$ (metal-oxide particle),

$$\alpha = \frac{\epsilon_2 - \epsilon_m}{\epsilon_2 + 2\epsilon_m}. \tag{2.32}$$

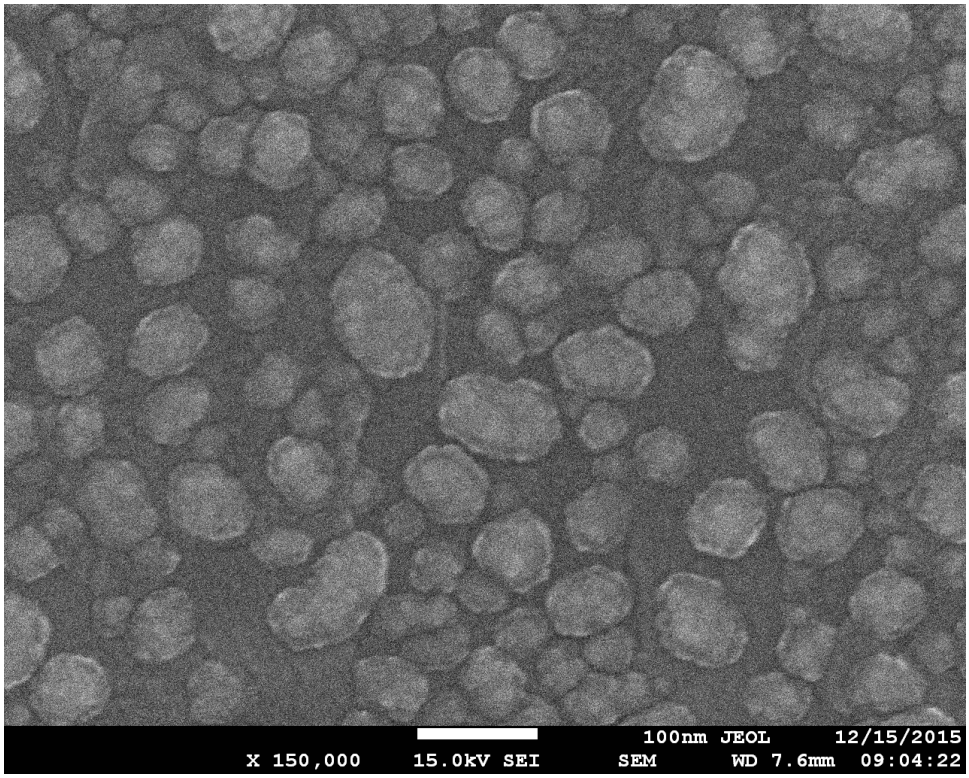

Figure 2.17: 7 nm TiO_2 deposited on gold nanoparticles.

The fit adjusted, and therefore determined the following parameters: the dielectric function, ϵ_1 of the gold core from which we wish to extract the value of ω_p (among others). This was done by using the function for ϵ_1 which contains among the adjustable parameters those we seek,

$$\epsilon_1(\omega) = 1 - \frac{\omega_p^2}{\omega^2 + i\omega\gamma} + \sum_j^N \frac{a_j}{\omega_{0j}^2 - \omega^2 - i\omega\Gamma_j} + \epsilon_\infty. \tag{2.33}$$

The fitted spectra (Figure **??**) by using ϵ_{MG} yields very nice agreement with the measured spectra for the three oxides used as capping layers for the gold nanoparticles when the nanoparticle/metal-oxide phase is assumed to be a film of thickness $d = 2\times r + t$, where $r = 5$ nm (radius of gold nanoparticle) and t is the layer thickness of metal-oxide deposited. As expected, the observed red-shift of λ_p tracks the index of refraction of the

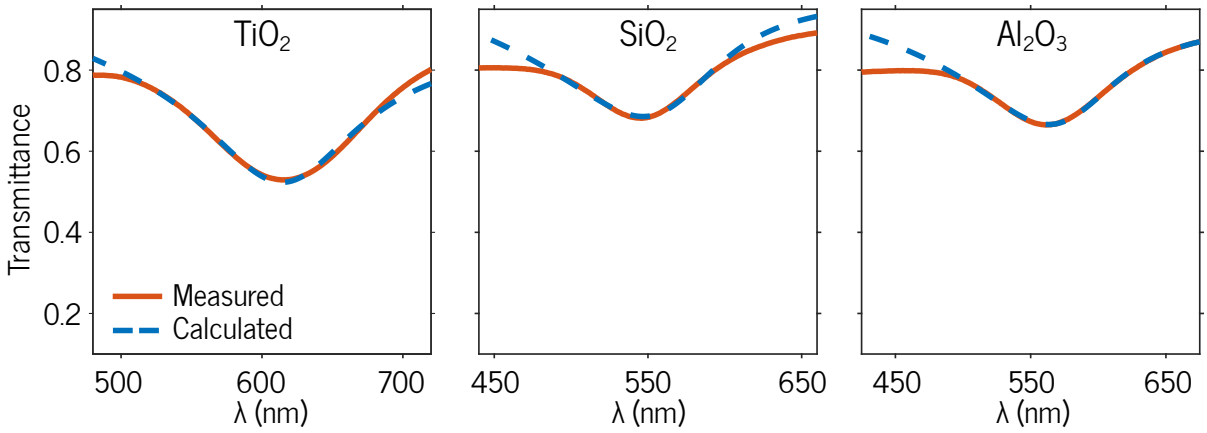

Figure 2.18: Measured optical spectra of Au — metal-oxide core-shell nanoparticles with similar shell thicknesses, 2 nm for TiO_2 and Al_2O_3 and 1.5 nm for SiO_2. Calculated spectra based on our proposed model showed very nice agreement with the measured spectra when performing a minimization around the plasmon resonance of the gold nanoparticle.

shell materials, n (SiO_2) = 1.5, n (Al_2O_3) = 1.7, n (TiO_2) = 2.4. The index of refraction of the shell materials was assumed to be constant within the spectral region of interest. The following values of ω_p (of Au-NPs) were returned from the fits obtained (Figure **??**): 9.0 eV for samples produced with TiO_2 and Al_2O_3 and 8.99 eV for the sampe fabricated with SiO_2. The scattering rates (γ) were determined to be in the 0.350-0.480 eV range which were somewhat higher than the uncoated gold nanoparticles. Samples for thicker shell layers for TiO_2, SiO_2, and Al_2O_3, were alos measured (Table 2.1).

As shown in Table 2.1, there is no obvious deviation in the values of ω_p from the expected value of 9.1 eV. Although we attempted to 'fix' what had appeared to be wrong values of ω_p for the Au-NPs with Al_2O_3 shells, the values were reproducible from batch to batch and we could not determine a proper explanation as to why the values were varying with shell thickness.

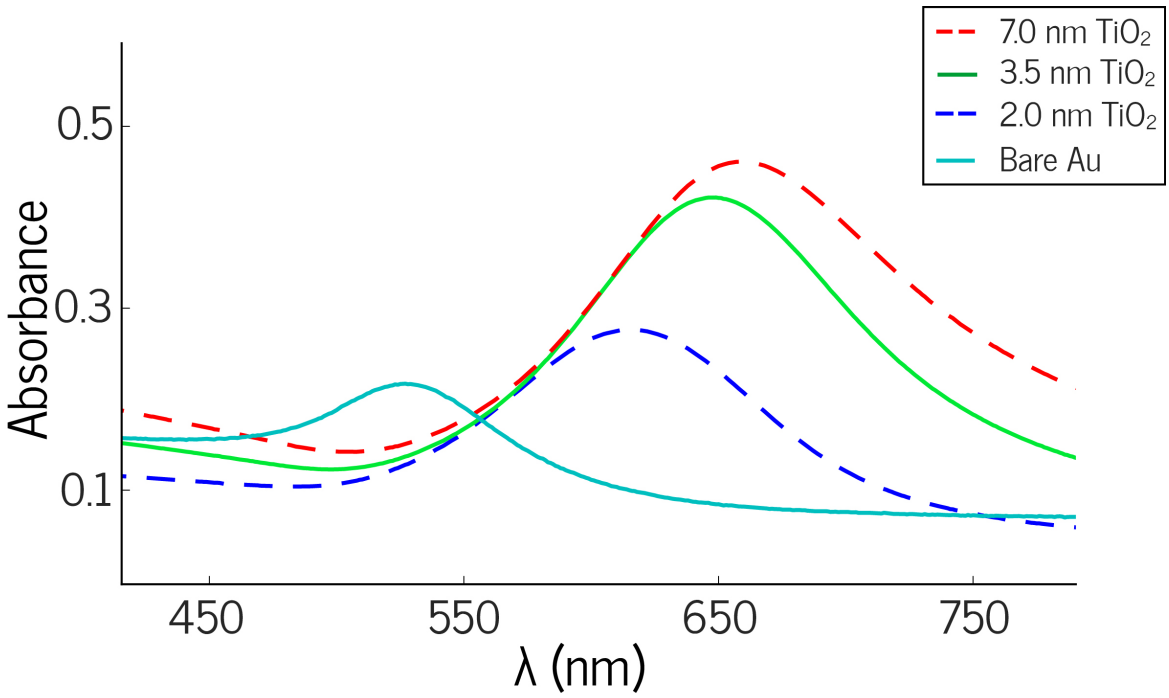

Figure 2.19: Transmission spectra for core-shell gold nanoparticles with various TiO_2 layer thicknesses.

Table 2.1: Extracted optical parameters of gold (ω_p and γ) as determined by the fitting algorithm with respect to the various film thicknesses of oxide, include as well are the volume fractions of the core-shell particles used in the Maxwell-Garnett calculation.

	nm (oxide)	ω_p	γ	$f_{C\text{-}S}$
Al_2O_3	2	9	0.350	0.6
	5.5	9.43	0.356	0.84
	10	9.24	0.275	0.95
SiO_2	1.5	8.99	0.381	0.47
	3.5	9	0.337	0.74
	7	9	0.331	0.9
TiO_2	2	9	0.481	0.57
	4	9.1	0.446	0.8
	7	9.1	0.464	0.9

2.4 Conclusions

By using a structural approximation of the gold nanoparticle / metal-oxide phase as an array of core-shell particles on a quartz substrate, we were able to employ a Maxwell-Garnett approximation to describe the effective dielectric function of the phase. We found no significant deviation of the optical parameters for the gold nanoparticles including finding γ values that were reasonable after adjusting for their size.

Because the diameter of the gold nanoparticles are on the order of 10 nanometers, it would interesting to see if this model would hold for large particles that are more applicable to plasmonic devices. Corrections may need to be used to account for increased scattering, as well as possible coupling between neighboring nanoparticles, thus expanding the versatility of this model to architectures that are of great interest those developing plasmonic based devices.

Chapter 3

Elucidating charge transfer dynamics through surface plasmon resonance and MG-EMA

3.1 Motivation and background

The magnitude and direction of charge transfer between two dissimilar materials has been throughly documented and well understood. [1] By using band diagrams proposed by electrostatics, one can predict and obtain qualitative trends when attempting to model charge transfer, as shown by Figure 3.1. Electrostatics, as the name implies, provides reasonable predictions when the electrical components are time-invariant. The system will become significantly more comlex when considering time dependent electrical fields due to the introductin of phase differences between the waveforms of the electrical fields. [22]

The electron energy levels of materials, synonymously called workfunction, Fermi level, electrochemical potential, thermodynamic potential, (depending on the field of

study and with slight modificaitons to the specific defintions), allows one to tailor the charge transfer between the materials.

Figure 3.1 shows the relative energy levels between three constituent materials where two dissimilar metals are placed in contact with an insulating material. As an arbritray reference point, E_{vac} is typically used the 'zero' energy for the electron. Typically called the 'vacuum level', this energy refers to the energy of a free stationary electron that is placed outside of any material within a perfect vacuum, or it can be defined being closer to the surface, or in another definition, it can be takenly infinitely apart from the material to where it no longer 'feels' the material. [1] This level is simply used as a method for aligning the energy levels between dissimilar materials, Figure 3.1, and provides very nice agreement between its use and experiments. The metals shown in Figure 3.1, with workfunctions ϕ_{m1} and ϕ_{m2} retain their intrinsic properties when placed far enough from each other to the point where they do not feel the difference in the electron energy levels, we can assume an infinite (although not physically meaningful) distance to assure they do not interact. We can then place a non-conducting (dielectric) material between the two metals to which the two metals will make direct contact with, shown by the equilibrium position in Figure 3.1.

Dielectrics will typically have various dielectric strengths associated with their electrical properties; the material can be characterized by their inability to transfer charge, or it can be see as how polarized the material can become before permanently modifying its structure to allow charge flow at high enough voltages, called the breakdown voltage. Upon reaching the breakdown voltage, the material irreversibly modifies itself since now the localized non-conducting electrons have become unbound from their nucleus. Dielectrics also have a Fermi level, not shown in Figure 3.1, which typically lies slightly below the middle of the bandgap (E_g) of the material. Because the Fermi level of the dielectric can vary extensively, we use the electron affinity χ which is the energy from

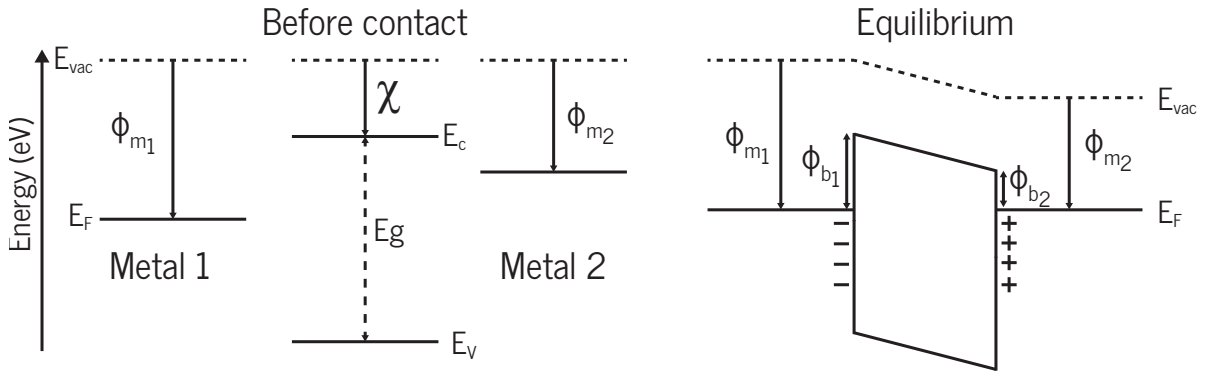

Figure 3.1: Energy levels of participating materials where ϕ_{m1} is greater than ϕ_{m2} with an insulator of electron affinity χ before participating materials are brought into close proximity of one another and after contact when the Fermi levels equilibrate throughout the participating materials resulting in a redistribution of charges.

the vacuum level to the conduction band (E_c) of the dielectric to align the energy levels between the materials.

Upon contact between all three constituent materials, charge transfer from the lower workfunction ϕ_{m2} metal to the higher workfunction metal (ϕ_{m1}) occurs to equalize the Fermi levels throughout all the materials. As shown in Figure 3.1, Metal 1 now retains excess negative charge due to the difference between the Fermi levels between the two metals, resulting in a build-in potential between the two materials. Qualitatively, the magnitude of charge transfer will track with the difference between the workfunctions of the materials as well as the thickness of the dielectric being used. The magnitude of the charge transfer is also dependent on the contact area between the two conductors where one can assume a parallel plate capacitor configuration where both metal electrodes are two flat plates with a film of dielectric between the plates or even a configuration where one metal is embedded in the other metal with a dielectric shell, the latter typically providing the most charge transfer per unit area. [32] By using the energy levels and certain numerical approximations, one can obtain a reasonable value for the magnitude of the charge transfer expected from such systems. However, it can be significantly complex

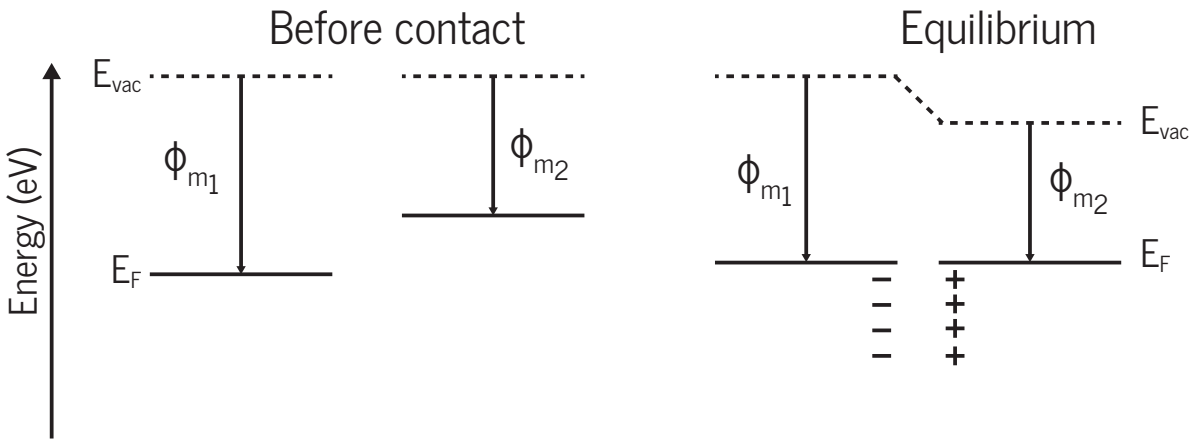

Figure 3.2: Charge transfer resulting from two dissimilar metals brought close to contact

when considering Fermi level pinning due to surface defects, Schotty junction formation between a metal and semiconductor, free charge carriers available in the dielectric, etc. Therefore, emperical methods for determining charge transfer are typically necessary to determine the true electrostatic interactions between dissimilar materials especially for a metal-insulator-metal (MIM) architecture, although appropriate approximations can be determined numerically. [33]

Figure 3.2 schematically shows charge transfer resulting from two dissimilar metals in direct contact with one another. As was shown in Figure 3.1, contact between the two materials will result in charge redistribution throughout the system. However, unlike in the case of the MIM strucutre (Fig. 3.1), the potential difference between the two metals upon contact cannot directly be determined upon contact as the charges will redistribute and a measured potential of 0 V will be determined if one tries to directly probe the surface potential due to the higly conducting nature of the metals. Instead, as Lowell demonstrated, one can accurately obtain the electrostatic charge transfer between two dissimilar conductors by bringing the materials into contact, separating them at a particular rate, and measuring their charge. [34] As expected, he determiend the surface charge was proprotional to the contact potential difference (difference in workfunction

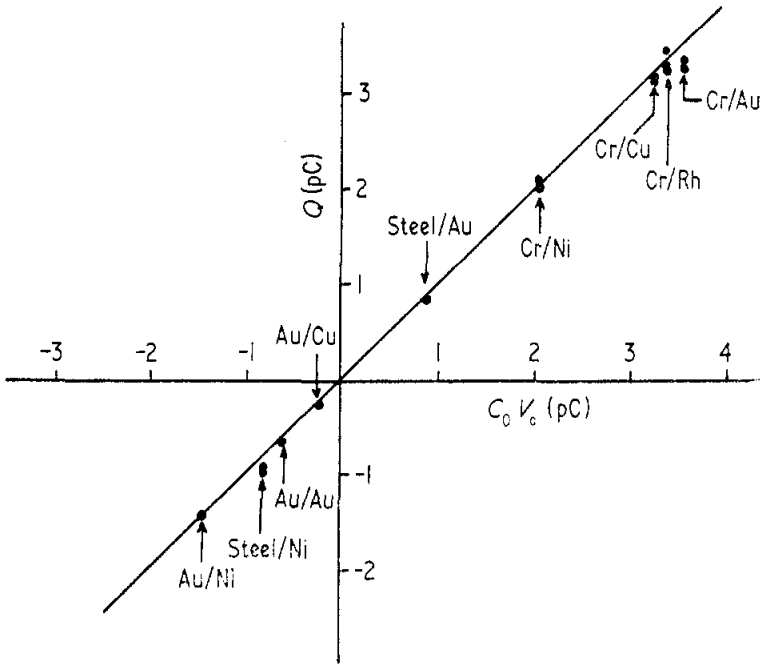

Figure 3.3: Charge, Q, measured on the spheres after separating the two conductive materials with various combinations of metals being shown. Adapted from [34].

values) of the two conductors, Figure 3.3. More importantly, he determined the charge was not affected by the velocity of separation, in contrast to prior findings.

The importance of contact electrification becomes increasingly important when designing micro and nano systems. For example, understanding the Schottky junction, a junction between a metal and semiconductor, was and continues to be an area of extensive research. The Schottky junction at the electrical contacts has caused many issues in transistosr devices due to its rectifying behavior at the contacts, causing the current-voltage current to be non-linear. This of course was unacceptable for the proper engineering of particular devices prompting throuough studies into understanding and eliminating the Schottky junction for particular devices. Although the Schottky junction was detrimental to various devices, it proved useful as a diode due to its rectifying behavior as well as an electron filter for plasmonic devices due to the build-in potential. [35, 36]

Understanding the electronic interactions in nanostructured plasmonic devices, such

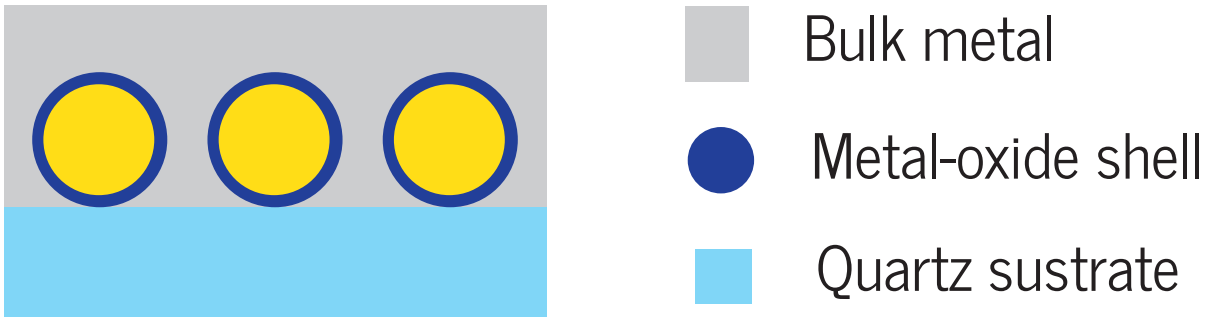

Figure 3.4: Schematic illustrating a gold nanoparticle in contact with a dissimilar bulk metal (Al — Ag — Au) through a metal-oxide shell, similar to the samples shown in Chapter 2.

as those in plasmonic photovoltaics, has beeen shown to play a significant role in the performance and efficiency of these devices. [12] With this in mind we were interested in constructing a sample where we could probe the electronic state of a nanostructured metallic nanoparticle, purely by measuring the plasmon resonance of the nanoparticle. We proposed the following schematic:

By using the same methods as used in Chapter 2, we can then probe the plasmon resonance of the gold nanoparticles by reflectance UV-Vis spectroscopy, and employ the model we developed to extract ω_p for the gold nanoparticles. By determining ω_p, we are then able to correllate changes in electron density with modifications made to the architecture of the sample shown in Figure 3.4. For example, how will the magnitude of charge transfer change when we use an aluminum bulk layer as compared to a silver bulk layer? Electrostatics can provide a reasonable approximation when comparing two dissimilar materials and by taking advantage of the sensitivity of the plasmon resonance of the gold nanoparticles due to the change in electron density, we can then determine the charge transfer by employing said methods.

For example, Zhang and coworkers were able to measure the change in the work-function of gold nanoparticles supported on a degenerately doped n-type silicon wafer separated by an organic bi-layer, Figure 3.5. [17]

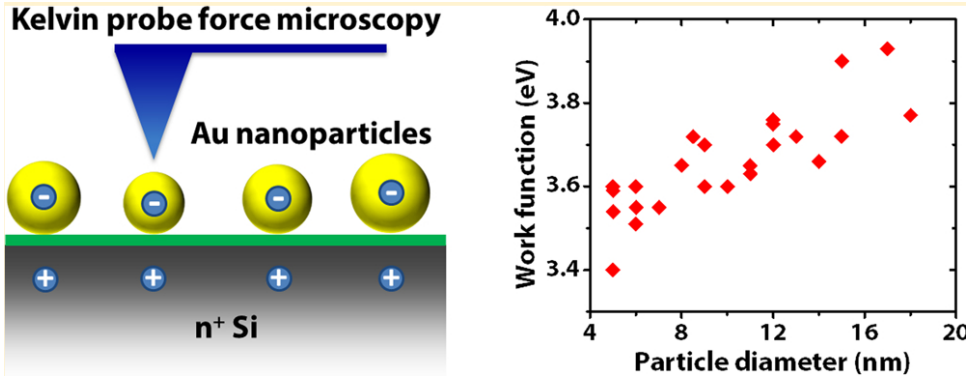

Figure 3.5: Schematic illustrating

With this basic device architecture, Zhang and coworkers were able to determine the electrostatic interactions at the nanoscale between the Si wafer and the gold nanoparticles. Due to the difference in the Fermi levels, they were able to employ Kelvin probe force microscopy to study the workfunction of the gold nanoparticles as a function of the oxide thickness of the Si wafer and the diameter of the gold nanoparticles. They determined the workfunction of the Au was size dependent and deviates strongly from that of bulk Au, the change being attributed to the difference in Fermi levels. Furthermore, they demonstrated the classical electrostatic model involving charge transfer between dissimilar materials was robust in prediciting the net negative charging of the gold nanoparticles, Figure 3.6.

Although the work by Zhang and coworkers primarily focused on the workfunction changes of the gold nanoparticles for sensing applications, their seminal work demonstrated that the predictions of classical electrostatics still holds true for nanostructured metals in contact with bulk like materials. Although such calculations may require further fine tuning for an exact numerical calculcation, which will typically deviate from actual measurements due to many factors, such approximations can be used successfully to tailor plasmonic systems where one would want to control the intrinsic charge transfer due to the difference in workfunctions of the materials.

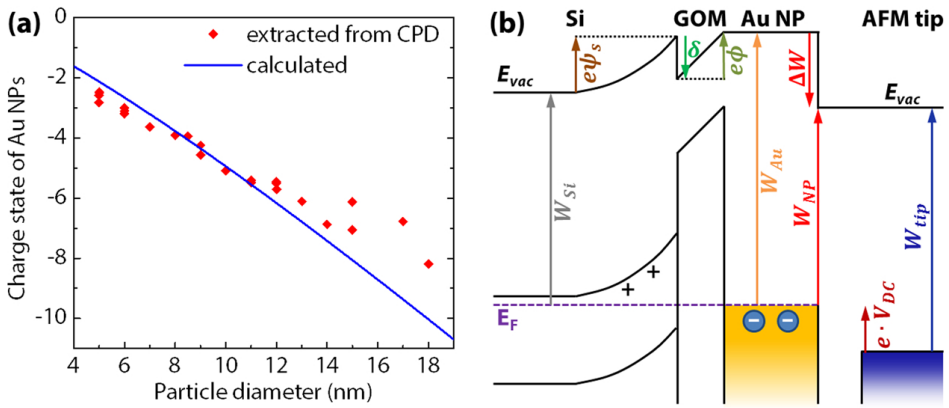

Figure 3.6: Device schematic, workfunction values and determined charge state of the gold nanoparticles from KPFM. Printed with permission from [17]

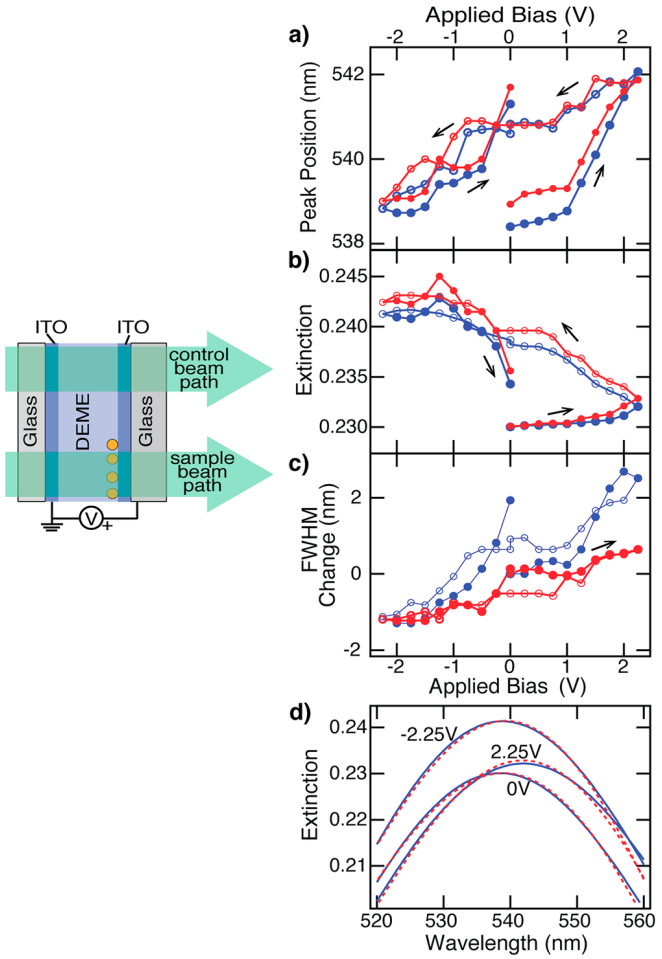

Figure 3.7: Experimental (blue) and simulation (red) results for various applied biases for the sample shown, +2.25, 0 , and -2.25 V. Reprinted with permission from [8].

Atwater and coworkers performed an experiment where they tuned the dielectric response of an array of gold nanoparticles under electrochemical bias, thus altering the charge state of the gold nanoparticle by charging or discharging the nanoparticle with an external source, Figure 3.7. [8]

Their method for probing the charge state of the nanoparticles was by monitoring the UV-Vis spectra of the nanoparticles under varying applied biases. Because the plasmonic response of metal nanoparticles are sensitive to the charge density, they were able to model the shifts of the plasmon resonance and attribute such shifts to the charging and discharging of the nanparticles. In fact, they were able to extract optical parameters, such as ω_p, that confirmed the change in the dielectric function of the gold nanoparticles. Their extensive work also corrected for the change in the index of refraction of the surrounding medium due to the applied bias and dampening effects.

Brown and coworkers were able to use a full wave electromagnetic simulation to model the optical response of the gold nanoparticles, for detailed analysis refer to [8], where they included a variable thickness conducting shell with modified dielectric function to account for the surface charging of the nanoparticles. They were demonstrated good fits with their modeling process even with the applied bias.

Similar work was performed by various contributors in the Mulvaney research group where they investigated the change in the optical response of single goldnanorods as well as silver nanoparticle films with varying applied potentials. [7, 37]

Their work, similar to the experiments Brown and coworkers performed, demonstrated the tunable response of the optical spectra of the plasmonic metals by electrochemical methods by using conventional dark-field spectroscopy providing further evidence that the plasmon resonance is indeed sensitive to the electron density of the nanostructured metal.

For our sample, we will use ebeam evaporated gold nanoparticles as the plasmonic

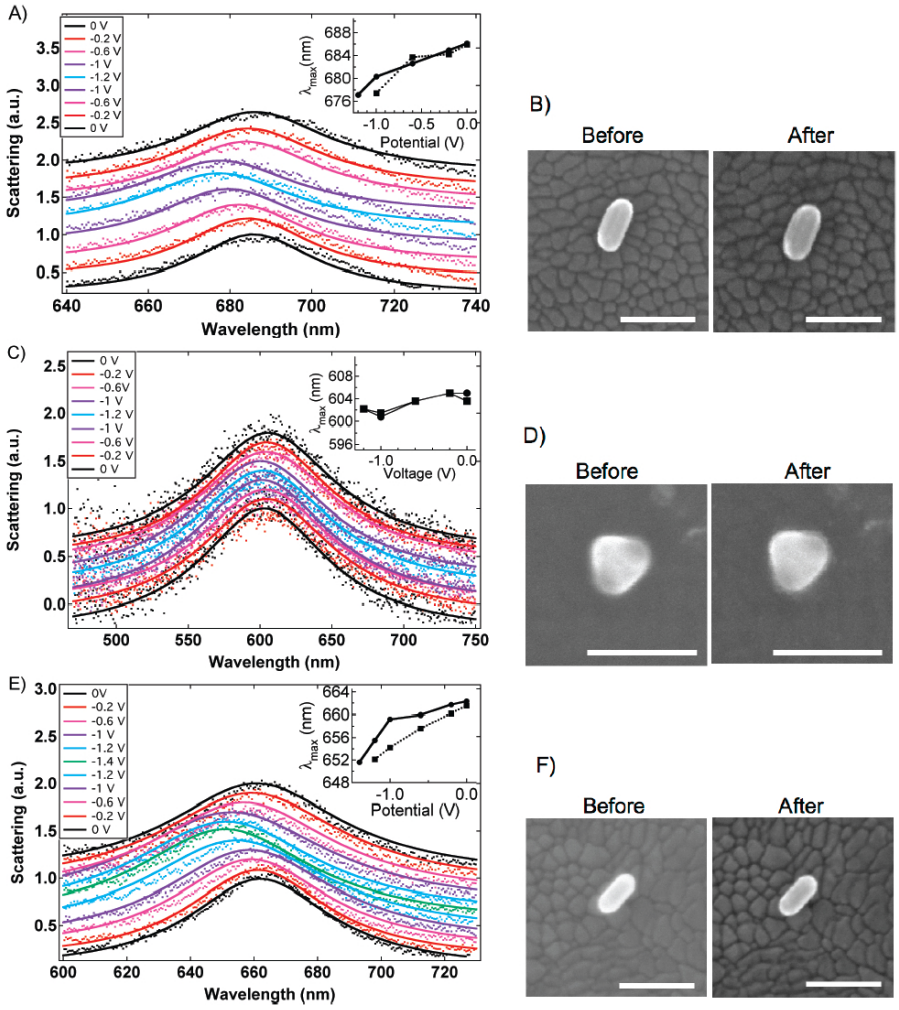

Figure 3.8: Scattering spectra resulting of the gold nanoparticles due to the various electrochemical potentials applied to the substrate along with their corresponding SEM images of the particles measured. Adapted from [7]

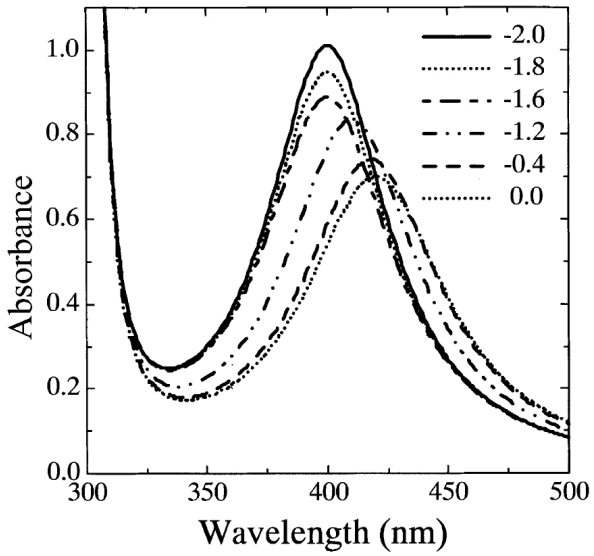

Figure 3.9: Spectra of Ag nanoparticle films as a function of the applied potential. Adapted from [37]

component within our system for which we can use our proposed Maxwell-Garnett effective medium approximation we used in Chapter 2 to extract optical parameters relevant to the dielectric function of the gold nanoparticles. We will then deposit various layer thicknesses of TiO_2, SiO_2, or Al_2O_3 followed by a bulk layer of ebeam deposited silver, aluminum, or gold. By varying the bulk layer, we can determine if the intrinsic differences in the Fermi levels between the gold nanoparticles and the bulk metal do indeed dominate the measurables changes in electron density, represented by an increase in ω_p before and after the addition of bulk metal, since $\omega_p \propto \sqrt{N}$ where N is the electron density of the gold nanoparticle.

3.2 Device fabrication and Experimental Methods

Fabrication for these devices followed the same initial steps as for the devices in chapter 2. Only difference was after obtaining the transmission spectra, we capped the nanoparticle/dielectric phase with 2500 $\mathring{A}$ of the following metals: silver, aluminum, and

gold, schematically shown in Figure 3.4.

Ebeam evaporation was used for capping the nanoparticle/dielectric phase. The bulk metal was deposited at 1.0 Å/s until a layer thickness of 100 Åwas obtained, followed by deposition at 2.0 Å/s to 500 Åthen deposition rate was 4.0 Å/s thereafter until the final thickness of the bulk metal is reached. A proper deposition rate was required to ensure the nanoparticle/dielectric phase is uniformly capped. Too high of a deposition rate will give a low quality/density film since we can not use post-thermal treatments to improve the quality of the film due to possible disruption of the nanoparticle/dielectric phase. After running though a few iterations of device fabrication, we realized the optical properties of the nanoparticle/TiO_2 phase would change significantly if left out too long. This was due to excess water absorption to the surface that could significantly change the properties of the TiO_2. This was not too surprising as the TiO_2 is significantly oxygen deficient and these deficiencies allow for water absorption to the surface, thus altering its electron density and changing the electronic behavior between the nanoparticle/TiO_2 phase.

Spectra were fitted using the same method developed in Chapter 2, except now we have a bulk metallic capping layer, which also acts a mirror for optical frequencies, which allowed us to obtain reflectance spectra of the nanoparticle/metal-oxide phase, Figure 3.11. The transfer matrix method handles the change in sample configuration very nicely and no further modification was needed to obtain proper fits. Method for obtaining a closed funtional form of the optical constants for the bulk metals are shown in Appendix A.

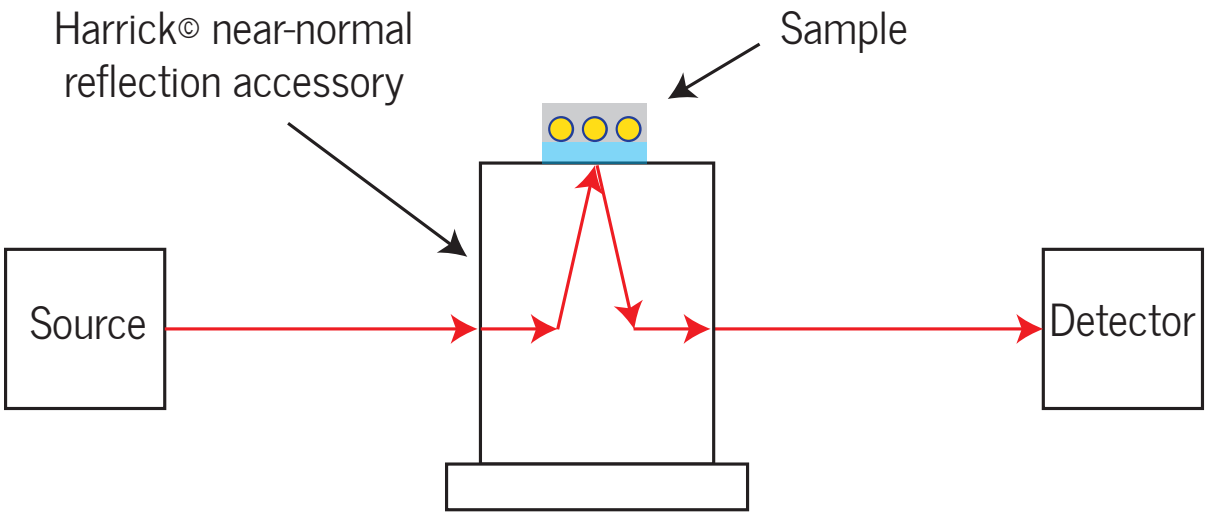

Figure 3.10: Simplified reflectance setup used for obtaining reflectance spectra of samples using Varian Cary UV-Vis-NIR 500 spectrometer. For clarity, the actual optical paths within the source and detector black box are not shown here but can be found from Varian's website.

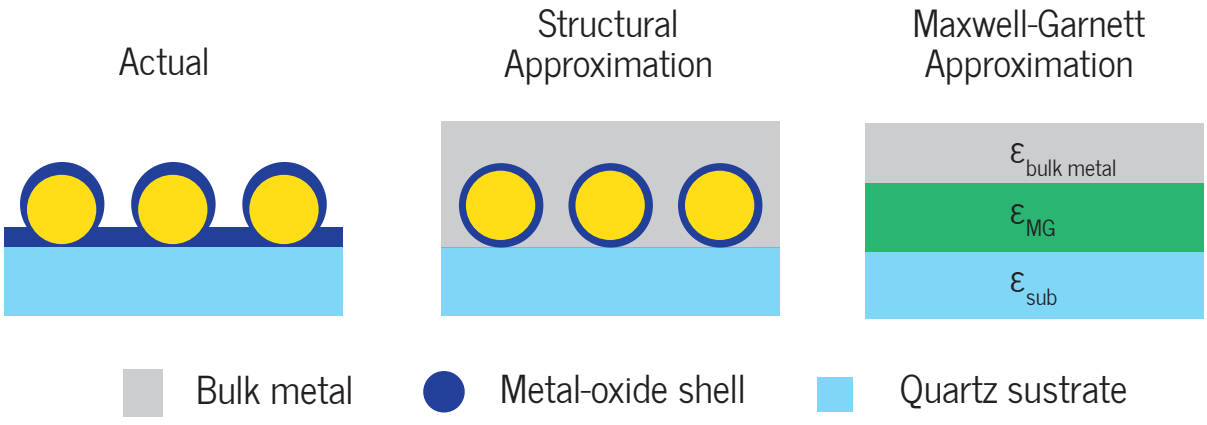

Figure 3.11: Schematic illustrating the structural approximations used in our proposed model to extract the effective dielectric function of the nanoparticle/dielectric shell.

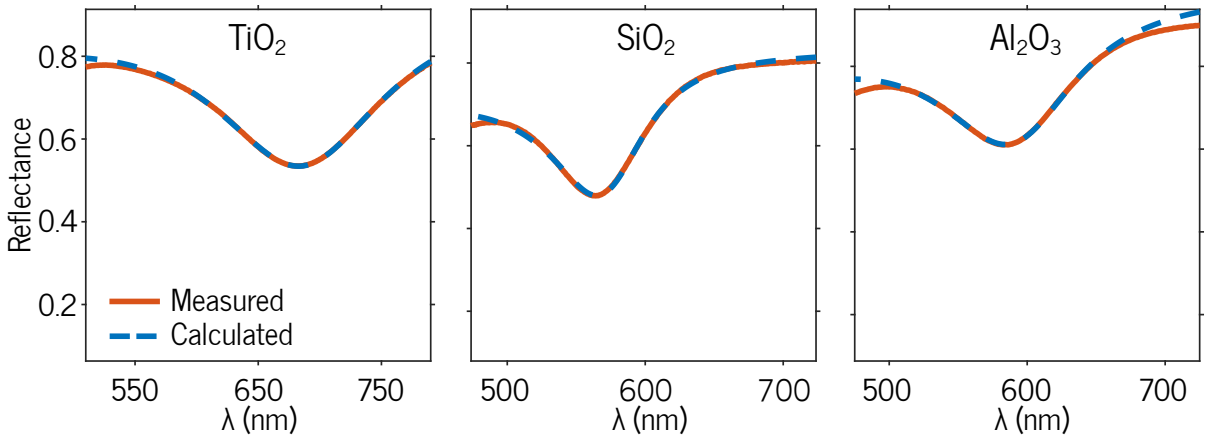

Figure 3.12: Measured and calculated reflectance spectra for core-shell nanoparticles with a silver bulk capping layer.

3.3 Results and Discussion

Spectra were obtained by using the same three metal-oxides and their respective thicknesses used in Chapter 2. Due to the opaque nature of the bulk metal deposited on the nanoparticle/metal-oxide phase, reflectance spectra were obtained instead of a transmittance spectra. Measured spectra and their corresponding fits for samples comprised of 2 nm TiO_2 or Al_2O_3 or 1.5 nm SiO_2 with a silver bulk layer are shown in Figure 3.12.

The extracted values (Table 3.1) show an increase in ω_p following the deposition of the bulk metal, implying an increase in the electron density in the gold nanoparticles. Assuming the effective electron mass is approximately unchanged by depositing the bulk metal the ratio of the electron density in the Au-NP after bulk metal deposition to its value before is given by,

$$\left(\frac{\omega_p'}{\omega_p}\right)^2 = \frac{N'}{N}. \tag{3.1}$$

At first glance, one might presume that this net charge transfer can be explained by the relative values of the work functions between the gold nanoparticle and the bulk metal. When two conductive materials with dissimilar work functions come to contact, their energy levels will equilibrate by electron charge transfer from the material with

		ω_p	ω_p'	N'/N	e^- trans./NP
TiO_2	Al	9	11.5	1.64	19,598
	Ag	9	11.4	1.60	18,639
	Au	9	11.9	1.74	23,074
SiO_2	Al	8.9	10.39	1.36	11,189
	Ag	8.9	10.64	1.43	13,263
	Au	8.9	11.6	1.70	21,548
Al_2O_3	Al	9	10.2	1.28	8,771
	Ag	9	10.3	1.6	9,551
	Au	9	11	1.74	15,228

Table 3.1: Extracted optical constants for gold nanoparticles before (ω_p) and after (ω_p') deposition of aluminum, silver, or gold bulk metal with 2 nm TiO_2 / Al_2O_3 or 1.5 nm SiO_2 shell. Included are calculated values of N and N' based on eqn. 3.1 along with calculated values of the number of electrons transferred per nanoparticle based on the extracted values of ω_p.

lower (ϕ_{m2}) to higher (ϕ_{m1}) workfunction, modifying the charge density of the materials in contact, as illustrated in Figure 3.13. Because gold has a larger work function than both silver and aluminum, we expect a net increase in electron charge density on the gold nanoparticles and an overall net positive charge on the bulk metal, as observed. The magnitude of this charge transfer will also depend on the electronic properties of the dielectric shell used.

Illustrated in Figure 3.14 a trend in the magnitude of the charge transfer tracked with the shell thickness, an acceptable trend if one considers the shell to be a material of constant resistivity throughout the thicknesses used, generally a good assumption for atomic-layer deposited films. Furthermore, the overall magnitude of the charge accumulation also tracks with the bulk properties of the dielectrics used. TiO_2, a conductive material due to the oxygen vacancies present after deposition, is expected to allow a higher charge transfer from the bulk metal to the gold nanoparticles.

When comparing the insulators, SiO_2 and Al_2O_3, there was a clear decrease in the magnitude of the charge transfer when using Al_2O_3 as the shell layer. This is expected due

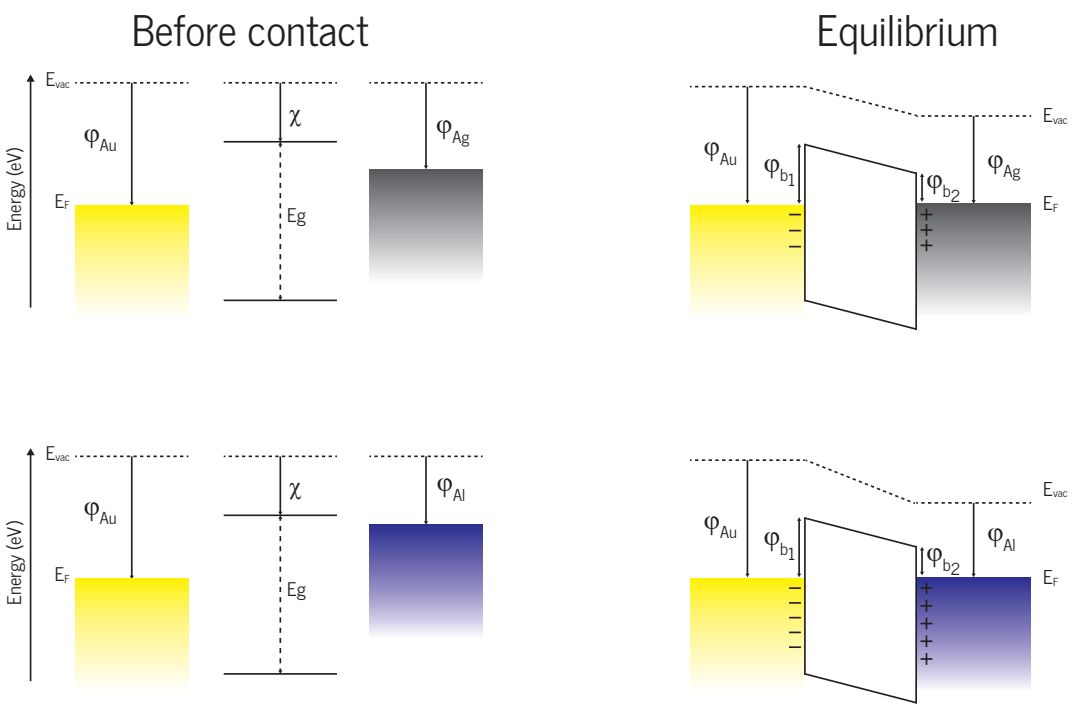

Figure 3.13: Relative energy levels of the system when using silver or aluminum as the bulk metal capping layer.

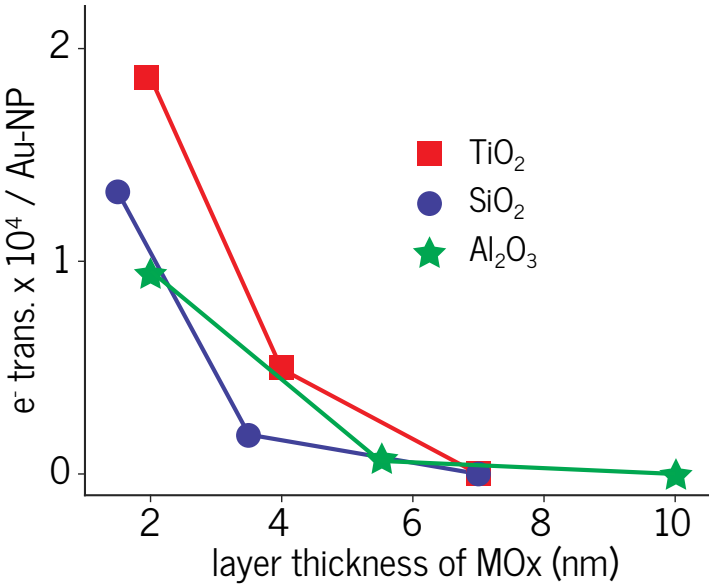

Figure 3.14: Caculated transfer of electrons per nanoparticle when in contact with a layer of bulk silver. Qualitatively, charge transfer trends with thickness of oxide deposited (t) as well as with the bulk electrical properties of the metal-oxide shell used with TiO_2 yielding the largest charge transfer due to its conductive properties and Al_2O_3 yielding the lowest charge transfer due to its higher dielctric constant and low electrical conductivity. Visual guides shown to aid in visualizing the trend and are not indicative of a fit to the data.

to the higher dielectric constant, bulk resistivity, and conduction band offsets of Al_2O_3 as compared to SiO_2. Although these values are not exactly quantified with respect to their bulk properties, if we consider the nanostructured nature of the composite and the approximations used to extract the optical parameters the values provide a very nice qualitative trend when comparing materials.

The most striking result noted from Table 3.1 is that the deposition of a bulk gold metal layer produces a charge transfer to the gold nanoparticles as large or larger than those produced by the other two metals. At first glance this might imply that the work function of the gold nanoparticles is larger than that of bulk gold. This, however, is not the case. Reported values for the work function or ionization values of gold nanoparticles indicate that for Au-NPs with radii $\approx$5 nm the work function is approximately equal

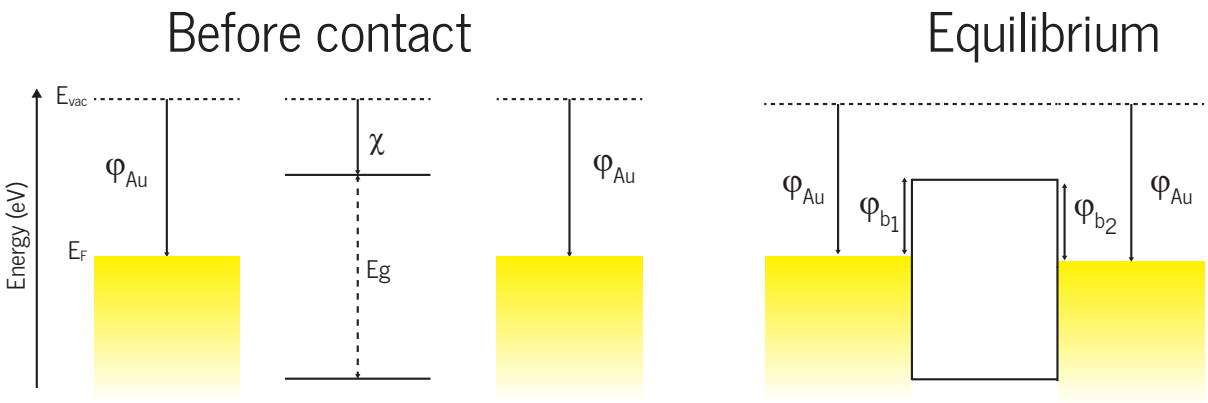

Figure 3.15: Demonstrating the negligible change in charge density when using the same metals.

to that of bulk gold. [38] We will show below that for the samples we produced, the relatively large charge exchange between the bulk metal layer and the gold nanoparticles is negligibly impacted by the difference in work function. We propose the large portion of the charge exchange is the result of the so-called palsmo-electric effect.

To justify the first statement we calculate the number of electrons transferred from the bulk metal to the gold nanoparticles using methods developed by Peljo et. al. [39,40] in which they use the capacitance matrix approach for calculating the surface charge on nanoparticles of varying size and workfunctions. The charges on two spherical conductors (q_i), A (Au-NP) and B (bulk metal sphere) of radii r_A and r_b, are computed by expressing the charges on each nanoparticle in terms of their outer electrostatic potentials (ψ_i) and the self and mutual capacitances given as follows,

$$\begin{bmatrix} q_a \\ q_b \end{bmatrix} = \begin{bmatrix} C_{AA} & C_{AB} \\ C_{AB} & C_{BB} \end{bmatrix} \begin{bmatrix} \psi_A \\ \psi_B \end{bmatrix} \tag{3.2}$$

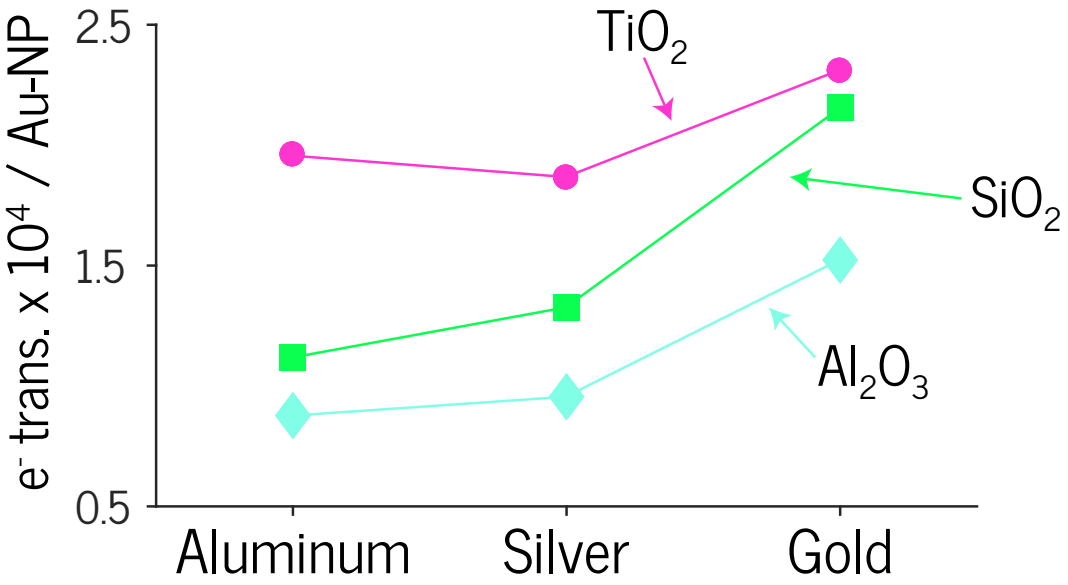

Figure 3.16: Measured charge transfer for all systems when using 2 nm of TiO_2 or Al_2O_3or 1.5 nm SiO_2.

Where the elements in the matrix are as follows:

$$C_{AA}(s) = C_0 \left[\lambda(s) - \psi_0 \left(x_b\right)\right] \tag{3.3}$$

$$C_{BB}(s) = C_0 \left[\lambda(s) - \psi_0 \left(x_a\right)\right] \tag{3.4}$$

$$C_{AB}(s) = -C_0 \left[\lambda(s) + \gamma\right] \tag{3.5}$$

Here, $x_i = r_i/(r_A + r_B)$, $2\lambda(s) = ln\left\{2r_a r_b/\left[\left(r_a + r_b\right)s\right]\right\}$, and $\psi_0(z) = d\left(ln\Gamma(z)\right)/dz$. Given a fixed spatial distance, s, between the nanoparticles and assuming the elctrostatic equilibrium condition, the following expression holds,

$$\left(\psi_B - \psi_A\right)_{eq} = -\left(\phi_B - \phi_A\right)/e \tag{3.6}$$

which implies the outer electrostatic potentials on each nanoparticle is dependent on the difference in their workfunctions (Figure 3.1).

Although our system consists of gold nanoparticles in contact with a bulk metal layer,

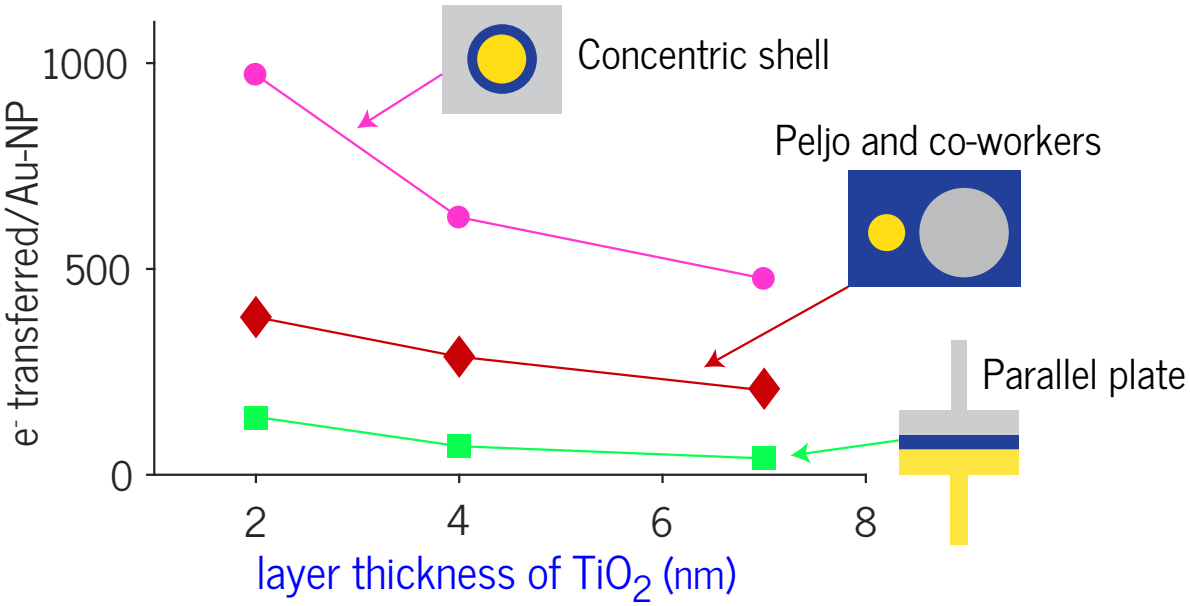

Figure 3.17: Calculated capacitance values assuming a 1 V potential difference between the silver and gold, based on the difference of their work functions.

the bulk metal layer to can be reliably approximated to be a particle of significantly larger radius than the gold nanoparticle (e.g. $r_b \approx 1000 \times r_a$). Accordingly, one can assume that the surface potential of the gold nanoparticle will be approximately equal to the difference in the workfunctions of the materials, in other words, in other words, $\psi_A = \phi_A - \phi_B$ and $\psi_B \approx 0$. This implies that the relative shift of the Fermi level of the bulk metal will be negligible compared to the shift of Fermi level of the gold nanoparticle. In the case of the gold nanoparticle, ($\phi_A = 5.3\ eV$) and silver bulk metal sphere ($\phi_B = 4.3\ eV$) with 2 nm TiO_2 shell and using Eqn. 3.2, we approximated using Peljo's approach that ≈ 400 electrons are transferred from the silver to the gold nanoparticle. This is significantly less than the 18,639 electrons transferred based on the shifts in ω_p in Table 3.1.

Clearly a model based on electrostatics cannot account for our observed results. We will now show that a phenomenon predicted and observed by Atwater and coworkers that they named the plasmoelectric effect does qualitatively account for our observations, and specifically, for the fact that bulk gold in proximity of gold nanoparticles results in charge

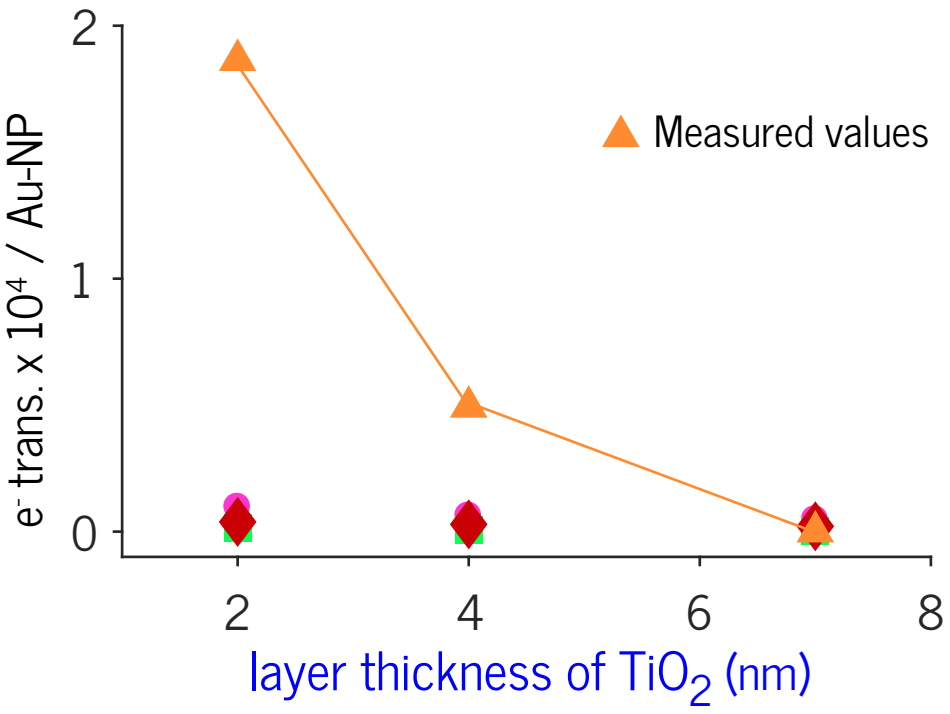

Figure 3.18: Comparing the measured and calculated charge transfer shown in Figure 3.17.

transfer, although, of course, only when the nanoparticles are illuminated. Even here, we show that the relative capacitances of the bulk metal and the nanoparticles play an important role, in that the electron transfer from the bulk metal to the nanoparticles is favored over the reverse process. In short, the plasmoelectric effect is an optically induced charging of nanostructured noble metals. This effect is observed when a nanoparticle electrically connected to ground, such as nanoparticles directly on a transparent conductive oxide, alter its charge density to attempt to match is resonance wavelength to the wavelength of the incident photon when the photon wavelength is slightly greater or less than the natural resonance of the gold particles. If the incident light is of a shorter wavelength than the natural resonance of the nanoparticle, the nanoparticle will transfer some of its electrons to ground; if the illuminating light is of a longer wavelength than the resonance of the nanoparticle, electrons from ground will flow to the nanoparticle until

its plasmon resonance wavelength matches the wavelength of the incident light. In brief, the plasmoelectric effect takes place because a system that absorbs light at resonance converting most of the absorbed energy to heat, increases entropy; hence when illuminated by light that is slightly off resonance a system might be induced to modify itself so as to come into resonance with the light, provided that the free energy decreases as result. Accordingly, the increased entropy due to light absorption predisposes the system to modify itself so as to be in resonance with the light illuminating it, provided that the energy associated with the modification does not overwhelm the entropic effect. Moving electrons to and from a conducting nanoparticle to ground normally requires relatively little energy; hence charge transfer to or from a particle illuminated by light slightly off plasmon resonance is not unexpected, as predicted and reported by Atwater and coworkers. By contrast, modifying a molecule to alter its structure so as to modify its electronic resonances would normally require a great deal of energy that would likely not be offset by the entropic effect; hence the equivalent process is not expected to be observed with most molecules. We ascribe the plasmon shifts, and the electron density changes on the Au-NPs, we observe when bulk metal is placed into contact with the Au-NP core-shell system to the plasmoelectric effect. As the light illuminating the NPs scans over the NP's resonances, electrons move from the bulk metal (at ground) to the nanoparticles when the light is of shorter wavelength than the resonance wavelength of the NP; and from the NP to the bulk metal when the NP's are illuminated with longer wavelengths than their resonance wavlengths. We further argue that the Schottky barrier between the metals and the oxide shell favors the process in which electrons are transferred from the bulk metal to the NPs over the reverse charge transfer process, accounting for our observation, that overall, when scanned with light of continously varying wavlength in the process of acquiring the system's spectrum, the plasmon blue-shifts for the samples in which the bulk metal is placed in close proximity to the Au-NPs.

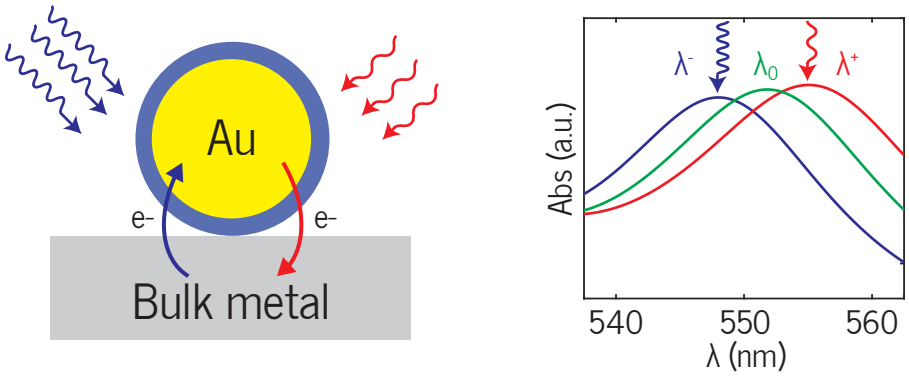

Figure 3.19: A qualitative schematic demonstrating the plasmoelectric effect; when illuminated with photons of wavelength shorter (λ^-) than the natural resonance of the gold nanoparticle the nanoparticle will accumulate charge whereas it will deplete charge if illuminated with photons of longer wavelength (λ^+). The sign on λ illustrates the resulting optically induced change in the charge of the nanoparticle as a result of the particle modifying it's electron density to allow it's resonance to match the wavelength of the incident photons.

These processes are illustrated in Figure 3.19 where the natural resonance of the nanoparticle is referred to as λ_0 and the resulting resonance due to illumination by shorter and longer wavelength photons are referred to as λ^- and λ^+, where the signs on λ indicate the resulting surface charge on the nanoparticles, i.e. λ^- implies a gain of electrons by the Au-NP with a blue shift in the NP's plasmon resonance, while λ^+ implies loss of electrons by the Au-NP causing a red shift in its plasmon resonance. Detailed background theory is reported in the seminal work by Atwater and coworkers.

The plasmoelectric effect was previously demonstrated with a system both gold nanoparticles on FTO or gold hole-arrays on quartz. In those reports the optically induced plasmoelectric effect yielded symmetrical surface charging about the natural resonance of the gold. [13] implying that when in direct contact with a conductive substrate serving as ground, the nanoparticles showed no net preference for either accumulating or depleting. This contrasts with our systems in which the gold nanoparticles are separated from ground by a thin, low conductivity shell with a rectifying contact due to the Schottky effect which is responsible for the lack of symmetry between our system's preference

of the gold NPs preference to acquire electrons from the bulk metal film over donating them to it. Referring to Figure 3.1, the potential barrier between the gold nanoparticle and the insulator (ϕ_{b1}) is larger than the barrier between the bulk metal and the insulator (ϕ_{b2}), which implies that over-the-barrier electron injection from the bulk metal to the gold nanoparticles is more probable to occur due to the smaller barrier. [41] For our samples, we observed that increasing the work function of the bulk metal (ϕ_{m2}) resulted in a higher degree of charging of the nanoparticle, further strengthening our conclusion that it is the plasmoelectric effect is mainly responsible for our observations rather than an electrostatic effect due to the relative values of the work functions of the Au-NPs vs the bulk metal film. Although the results track reasonably well with the known bulk dielectric properties and electron conduction properties for TiO_2, SiO_2, and Al_2O_3, the electrostatic model falls short in accounting for the charging effects of the gold nanoparticles.

3.4 Conclusions and Future Work

In conclusion, using a Maxwell-Garnett effective medium approximation, we were able to extract reliable ω_p values of gold nanoparticles which served as the core in core-shell particles embedded in dielectric and bulk metal media. Since ω_p is a measure of the electron density of the nanoparticles we determined that the proximity of a bulk metal (Ag, Al, and Au) produced an increased negative charge on the Au core. The observed results could not be accounted for using purely electrostatic arguments. However, our observations accorded well with what is predicted by the plasmoelectric effect, a phenomenon predicted and measured by Atwater and coworkers in which gold nanoparticles can acquire either positive or negative charges when illuminated by light whose wavelength is near but not coincident with the natural plasmon resonance of the mteal nanoparticle.

Although we demonstrated what we believe to be the plasmoelectric effect dominating the change in charge density of the gold nanoparticles by the observed increase in ω_p, I believe there are a few more experiments that can further support this conclusion. In particular, one experiment that can be done is performing a normal reflection UV-vis measurement, as we showed in this chapter, but perform the measurement with varying light intensities as Atwater and coworkers performed for their samples, Figure 3.20. [13]

If indeed our sample is dominated by the plasmoelectric effect, we should obtain ω_p values that correlate with the light intensities, as in, ω_p should increase with light intensity. Another possibility would be to fabricate an array of gold nanodisks into various layer thicknesses of similar dielectric oxides used in our study (Al_2O_3, TiO_2,SiO_2) onto FTO. This would allow for workfunction measurements, similar to those performed by Zhang and coworkers. [17] With this architecture, we could do the following:

- Workfunction measurements on the gold nanodisk to determine if the workfunction measurements correlate with the classical electrostatic models where we can vary the layer thickness of dielectric between the gold nanodisk and the FTO, or even use n-Si, as measured by Zhang and coworkers. These measurements will be performed with no illumination to determine the charge increase in the gold nanodisk from only the differences in the Fermi levels of the FTO and gold nanodisks.

- Perform light intensity measurements with KPFM to determine the change in charge density of the gold nanodisk with respect to various light intensities and wavlengths of light used. The change in charge density from these experiments would then be attributed to the plasmoelectric effect.

With this we could then separate the contributing effects from both electrostatics and the plasmoelectric effect with the same sample. Furthermore, since we would be directly probing the gold nanodisk through electrical measurements, it would no longer be neces-

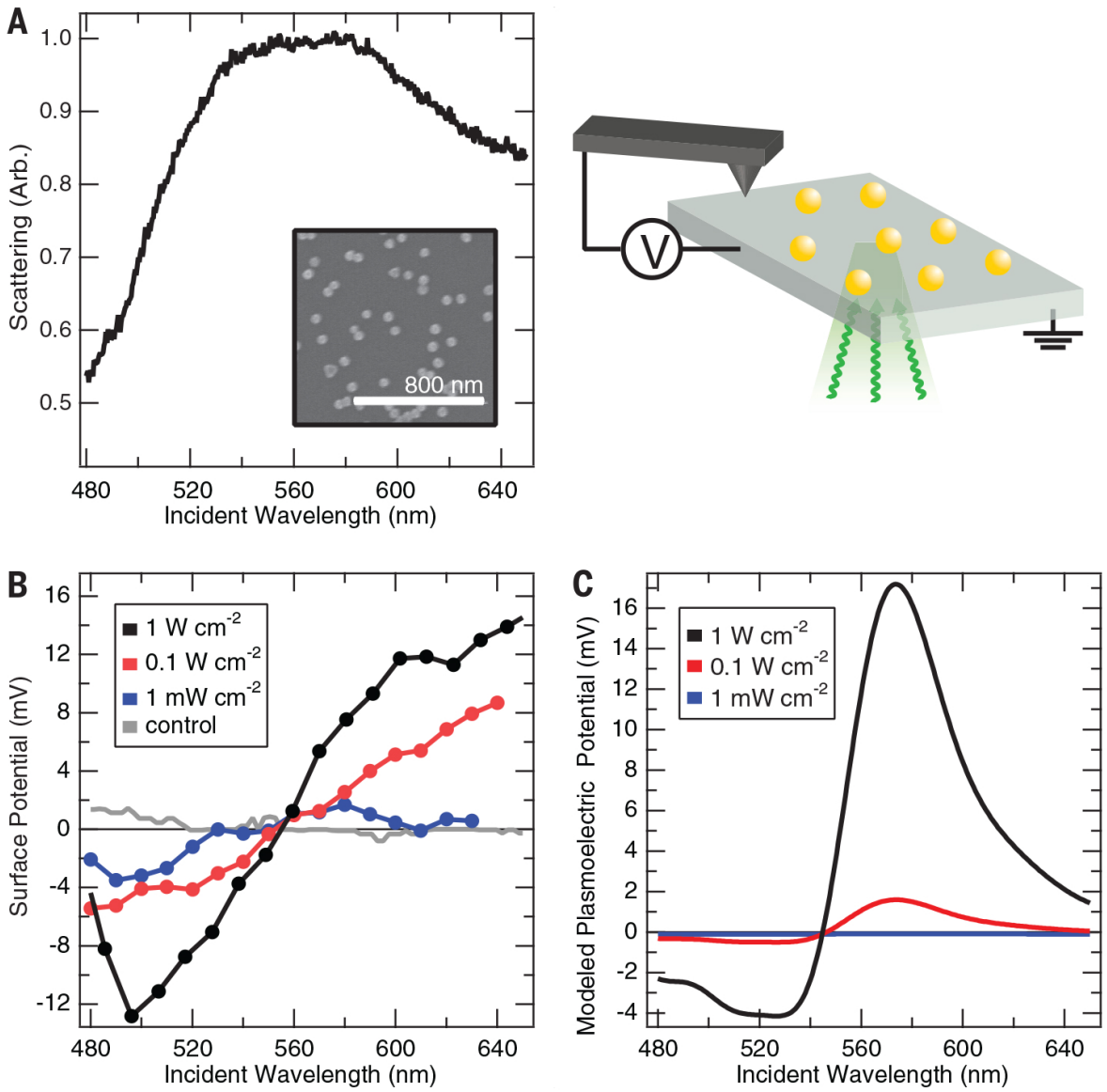

Figure 3.20: Plasmoelectric effect measured for an array of gold nanoparticles at varying light intensities by measuring the surface potential with KPFM. Shown also is the modeled plasmoelectric effect for the same measured array. Adapted from [13]

sary to perform a Maxwell-Garnett approximation model to extract ω_p, thus minimizing errors due to the approximations used for the calculations.

Chapter 4

Towards a gate-tunable heterogenous catalytic platform

4.1 Motivation and Background

4.1.1 Principles of metal oxide based catalytic sensors

The goals of optimizing catalytic reactions include generating faster, more efficiently, and cost-effective, metal-oxide supported catalytic platforms. Methods that have led to enhancing such reactions include nanostructuring of the metal-oxide support, introducing dopants into the metal oxide framework, and by depositing noble metals on the surface of the support. All these efforts have allowed chemist to develop an extensive library of physical parameters that can be tailored to provide the desired product with a given catalytic system. These efforts have allowed for the development of more efficient catalytic converters for automobiles where one wishes to minimize the toxic gases produced by the engine by converting the toxic gases into benign and non-toxic products. It has also allowed the chemical industry to produce valuable and highly desired products on the

large scale. Furthermore, an application of catalytic reactions with metal-oxide materials, apart from the chemical synthesis application, is that of gas sensors. Gas sensors work on the same basic working principles of catatlytic reactions with a metal-oxide support. However, unlike traditional catalysts, the support for gas sensors must be conductive to allow one to make electrical contact to the support since it is necessary to make contact to the support since by monitoring the current of the gas sensor, one can determine the surface chemistry occurring on the surface of the metal oxide support. [42] therefore, by using a semiconducting metal oxide, it would then be possible to monitor the surface reactivies occuring on the surface purely from a condumetric standpoint.

Typical requirements for a metal oxide material to be eligible to be used as a condumetric gas sensor include:

1. Reactions occuring on the surface must be reversible, otherwise the sensors will be useless once all reactive sites have been filled

2. Must be physically stable at elevated temperatures, usually greater than 100 °C

3. Electrical contact to active material without excessive contamination or damage to surface

4. Maintain conductivity during operation of the device, including during gas introduction

With these basic requirements, there have been a significant amount of oxides that have in some way been used as a condumetric gas sensors including: Cr_2O_3, Mn_2O_3, Co_3O_4, NiO, CuO, In_2O_3, WO_3, TiO_2, V_2O_3, Fe_2O_3, and many more. [43] While the above mentioned materials have shown to be sufficiently conductive to be operated as a gas sensor, not all exhibit the same surface chemistries nor do they exhibit they same sensitivites towards similar gases. With this in mind, many derivatives have been fabricated

that can be tailored towards specific applications such as:

- Medical applications for diagnostics and patient monitoring
- Use by military for detection of explosives
- Poisonous gas detection such as carbon monoxide in homes
- Detection of combustible gases in industrial applications

A general schematic for a condumetric deivce based on thin metal oxide is shown in Figure 4.1. Although nanotubes, nanowires, and other structures based on metal oxide materials have been synthesized and used as gas sensors, the primary focus of this dissertation will be primarily on thin films. [44] As mentioned in the requisites for a metal oxide material to be eligible to be used as a condumetric gas sensor, electrical contacts are necessary to probe the conductivity of the material when exposing to various gases. Shown in Figure 4.1 the metal oxide material is either grown or deposited onto an insulating substrate such as thick thermal oxide (SiO_2) on silicon. This prevents electrical shorting of the device where the conductivity of the substrate would be measured instead of the conductivity of the metal oxide material. For these devices, there are typically two electrical contacts made to the active metal oxide material, designated as source (S) and drain (D). The source is typically considered to be held at ground (0 V) potential to serve as the reference while the voltage is applied across the source and drain contacts which allows one to measure the conductivity while exposing the film to gases.

The conductivity in semiconductors can be attributed to two majority charge carriers: electrons and holes. When electrons are the majority carriers, the semiconductor is designated as an 'n-type' material whereas a semiconductor with holes as the major carrier is considered to be a 'p-type' material. [45] While the physics and properties of n and p type materials are not within the scope of this dissertation, it is important to

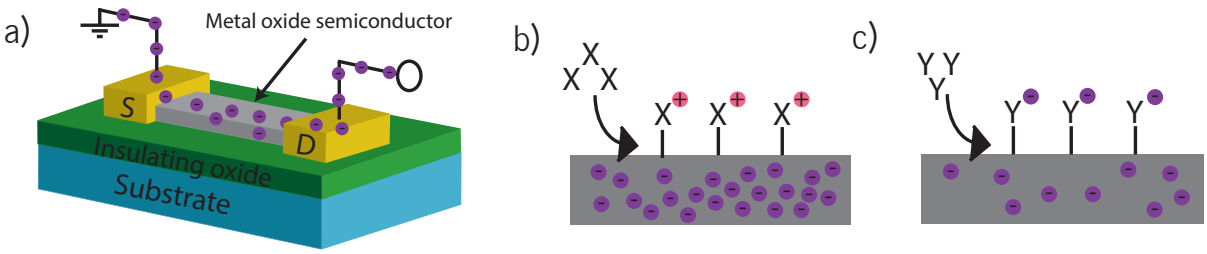

Figure 4.1: a) Basic schematic for a thin film device based on a metal oxide semiconductor on an insulating substracte with source (S) and drain (D) electrical contacts. Illustration depicting an electron b) donating or c) withdrawing gaseous species that can significantly modify the free charge carriers within the conduction channel of the material, thus modifying its measured conductivity.

know that gas sensors of both majority carriers have been synthesized. For the rest of this dissertation, n-type metal oxides will primarily be studied and characterized, therefore transport and current properties will be primarily addressed assuming n-type conductivity depicted in Figure 4.1.

For the materials studied in this dissertation, n-type conductivity arises from oxygen deficiencies in the metal oxide structurem, thus unintentionally electron doping the material. These oxygen vacancies allow for shallow donors slightly below the conduction band of the semiconductor that can be thermalized at room and elevated temperatures. [46] Due to the oxygen deficiency, TiO_2 is no longer fully coordinated and will thus donate its free electron to conduction in the bulk. Using the energy levels of TiO_2, it has been shown that oxygen vacancies introduce a shallow donor level band ranging from 0.75 to 1.18 eV below the conduction band. [47] Typically, the position of the donor levels will vary on the conditions used for synthesis of the material, even for TiO_2. It has been shown that donor levels and concentration can also be modified after the material has been synthesized, thereby expanding the accessibility to a wide range of desired characteristics. [48]

With regards to the energy levels of metal oxide system, one can even decrease the amount of free carriers within the material by introducing oxygen gas to the system.

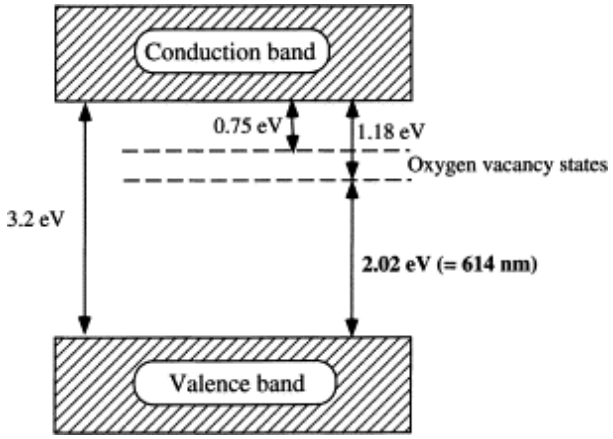

Figure 4.2: Position of donor levels due to oxygen vacancies for TiO_2 films, adapted from [47]

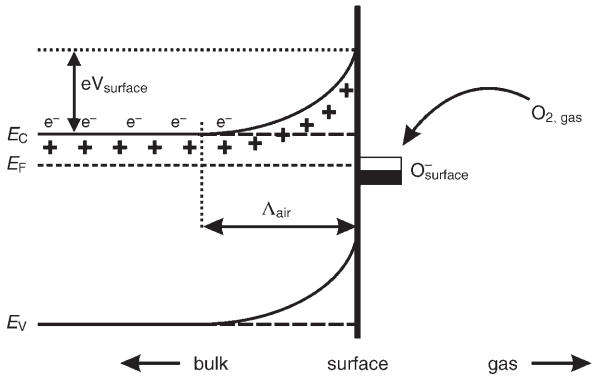

Figure 4.3: Band bending induced due to chemisorption, adapted from [49]

In one example, when oxygen gas is introduced at elevated temperatures, it will adsorb to the surface of the metal oxide resulting in extraction of a free electron that leads to electronic band-bending at the surface. The band-bending resulting from the adsorbed oxygen decreases the number of charge carriers in the material thus causing a decrease in the conductivity of the material shown by the model in Figure 4.3.

This is further illustrated by the schematic shown in Figure 4.4. Since many of the metal oxide films used for sensing are based on polycrystalline materials, the film is depicted here as a polycrystalline film with various size domains where conduction of charge carriers proceeds through the percolation path of the bulk material.

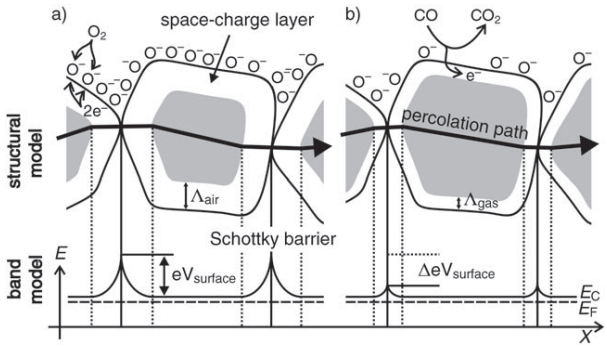

Figure 4.4: Conduction path associated with adsorbed oxygen assuming n-type conductivity.

4.1.2 Thin film devices towards heterogenous catalysis

In the studies discussed in this dissertation, we primarily focused our efforts on TiO_2. Although the true nature of the TiO_2 films in our studies are more like TiO_x due to the oxygen deficiencies within the lattice, the material will be simply referenced as TiO_2 to avoid confusion on the exact nature of 'x'. Furthermore, our studies will focus on three methods of fabricating TiO_2 films: a) oxidization of e-beam evaporated Ti films, b) atomic layer deposited films of TiO_2, and c) sputtered TiO_2 films. TiO_2 films in pristine, doped, and decorated with metal nanoparticles form, have been shown to be a highly tunable, selective, and robust chemical sensor. With the plethora of physical and chemical parameters that have been used to enhance the sensing properties of TiO_2 there has been little progress in recent years towards any new significant findings in the field of sensing. Of particular interest, we became interested in developing a platform that could not only be used as a sensing array, but also as a heterogenous catalytic array. The difference between sensing and heterogenous catalysis is quite vague as they both involve surface processes dictated by the surface chemistry of the metal oxide film. Attempts to clarify the difference will be made here. Sensing devices are primarily optimized to detect a compound from a background containing multiple analytes. This can be done by tailoring the metal-oxide material with certain dopants or metallic nanoparticles to

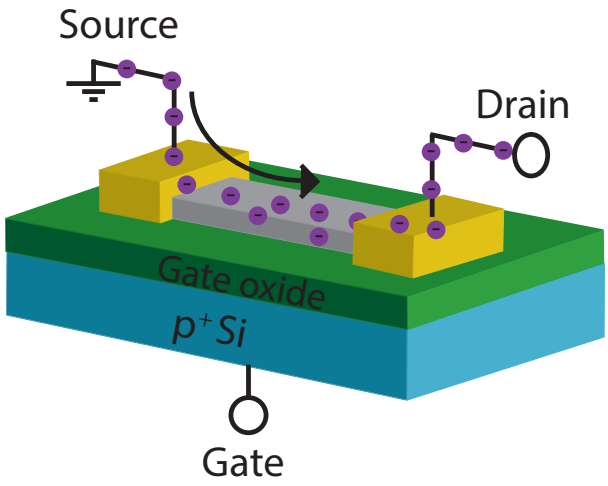

Figure 4.5: Schematic for proposed TiO_2 thin film device for a gate-tunable heterogenous catalytic platform.

increase the propensity for a particular analyte to react with the substrate and provide a measureable output, with no interest in determining, analytically, the products formed. However, for our proposed device, we wish to have a way to tune the products formed from the surface, schematically shown in Figure 4.5.

The device configuration in Figure 4.5 has been widely implemented to increase the sensitivity of gas sensors.

The device configuration shown in Figure 4.5 allows one to modulate the charge density of the active channel, in this case, any conductive metal-oxide one chooses to use and in turn, this will effectively modulate the chemical potential of the surface, ideally allowing one to modulate the products created at the surface of the metal-oxide as a result of simply applying a potential across the gate oxide. This can be further expanded by incorporating metallic nanoparticles where its chemical potential is in constant equilibriums with the chemical potential of the conductive channel, therefore, its chemical potential would in principle be modulated as a result of the charge modification within the active channel.

Modulation of the charge density within the active channel of the metal-oxide is

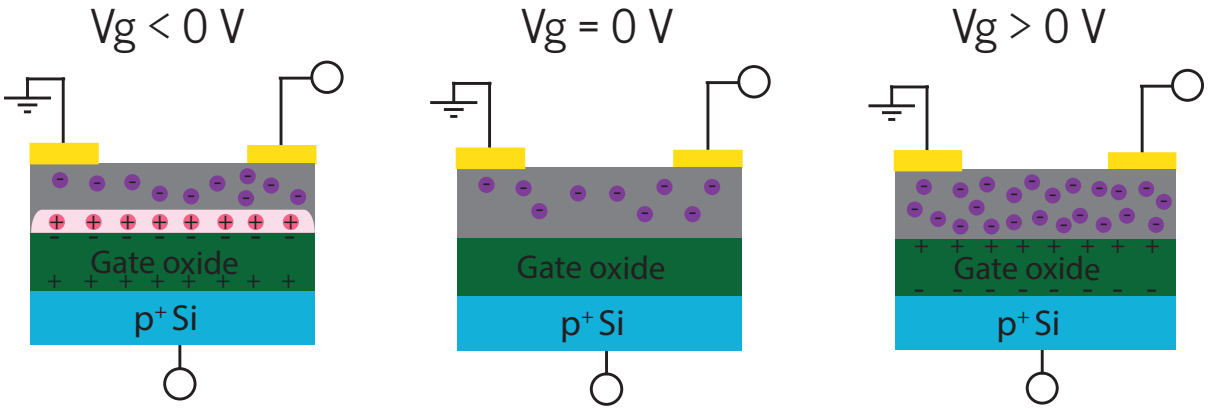

Figure 4.6: Gate-effects modulating the charge density of the active channel, shown in gray, by applying a potential across the gate oxide polarizing the insulator causing charge accumulation with the surface in contact with the conductive channel. Choosing a negative or positive gate potential allows one to fine-tune the electron density within the conductive channel.

schematically shown in Figure 4.6

Our proposed work was primarily inspired by earlier work performed in the Moskovits lab by Zhang and Kolmakov where they showed that the rates and extent of oxidation and reduction reactions can be modified by varying the gate potential on the nanowire, thus changing the electron density within the nanowire. [50]

The study by Zhang and coworkers concluded that the gate potential can have varying effects depending on what species are interacting on the surface of the oxide material. One important finding was that if the number of electrons within the nanowire are reduced, by applying a negative gate potential, the number of available electrons for surface chemistry is significantly impacted thus lowering the oxidation rate and the extent of oxygen adsoprtion.

Our proposed device towards development of a gate-tunable heterogenous platform is schematically shown in Figure 4.5. Catalytic reactions require elevated temperatures typically over 100 °C which will significantly impact our choice for the gate dielectric material. With this device, we hope to apply a potential across the gate dielectric for a

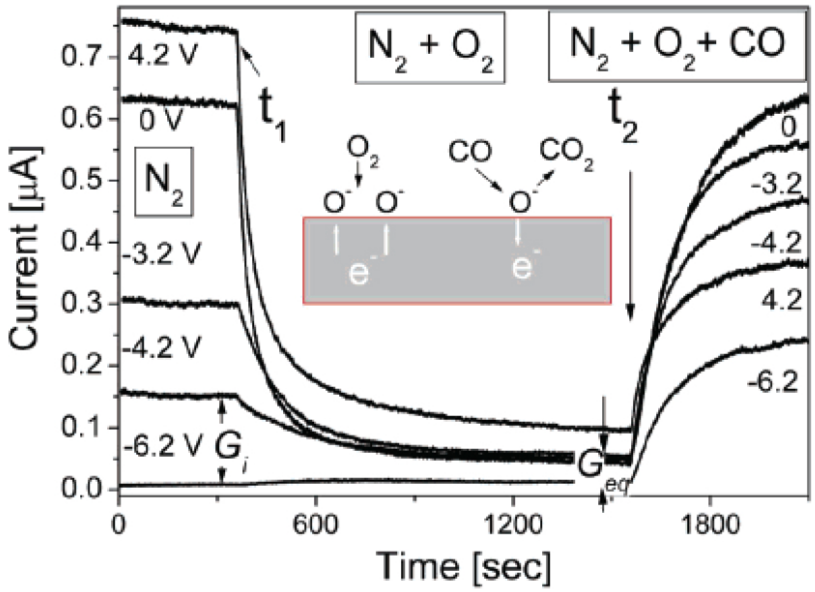

Figure 4.7: The current response at various gate potentials when adding oxygen, decaying exponential, followed by the addition of CO, rising exponential. Adapted from [50].

significant amount of time to measure the formation of its product with a quadropole mass spectrometer used in trace analysis. However, leakage current and dielectric breakdown become significantly pronounced at elevated temperatures necessitating the need for a relatively thin active channel to allow for proper modulation of the charge density within the active channel, in this case, TiO_2.

4.2 Results and Discussion

We chose three different techniques for fabricating TiO_2 thin films: thermal oxidation of ebeam deposited titanium films, atomic layer deposited (ALD) thin films, and reactive ion sputtered thin films.

All samples were tested in a custom made probe station schematically shown in Figure 4.8.

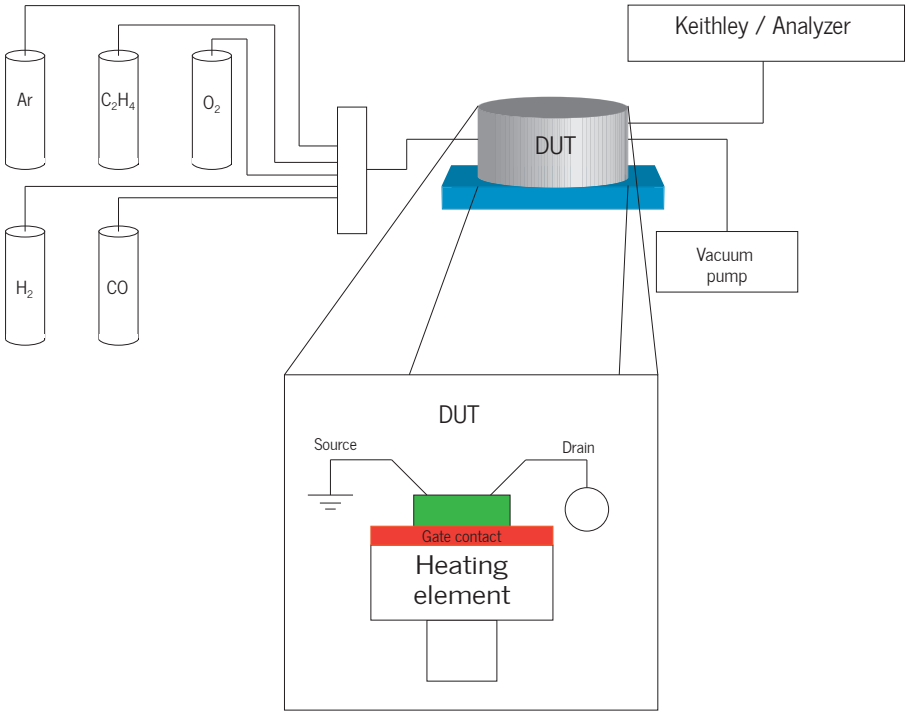

Figure 4.8: Schematic used for gas testing setup

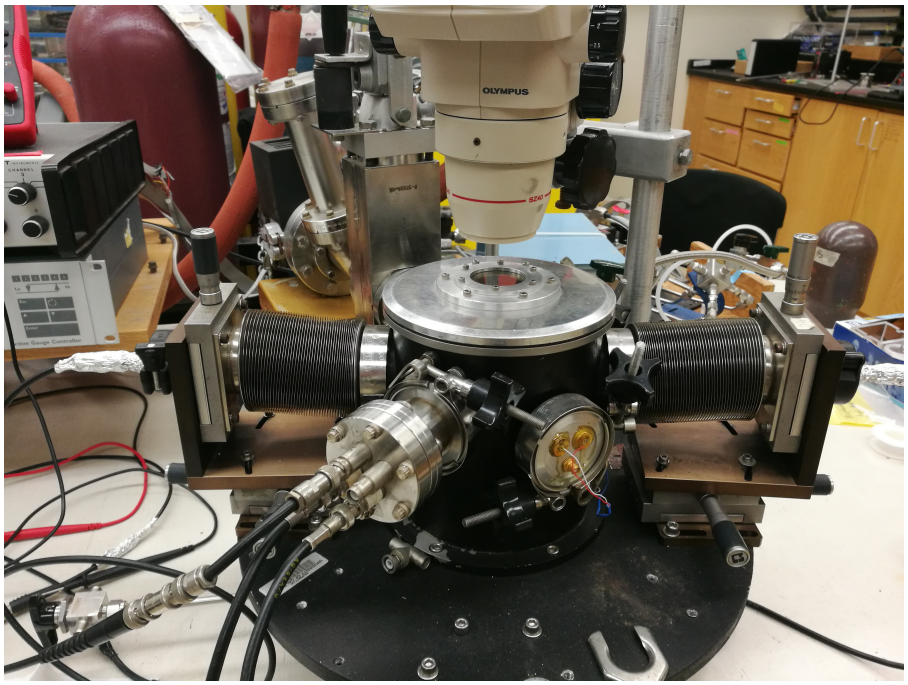

Figure 4.9: Custom built probe station used for gas testing of the TiO_2 thin film devices.

The custom amde probe station has a base pressure of approximately 9.5 x 10^{-4} torr after further modifications were made to the original configuration. Although this base pressure would arguable not be acceptable for surface chemistry reactions, we used a background flow of nitrogen as a baseline for our measurements. The chamber itself is sealed by a removable viewport that we use with a compound microscope to view the sample to make contact with the probes, Figure 4.9.

Although I show 5 separate gases connected through mass flow controllers to the testing chamber, we could only use three at one time. I had many issues with a few of the mass flow controllers, and I could not find any suitable replacements for them. We had considered buying new mass flow controllers but deemed it not necessary since we weren't sure about the longevity of this project, therefore making it irresponsible to purchase mass flow controllers if we were only going to use them during my time here. Therefore, we chose to always have the argon connected, since it served as our background and carrier gas, and switch the mass flow controllers to whichever gas was needed.

The sample stage was a ceramic block, built by the machine shop in the Chemistry department, where the heating element used was a basic lightbulb controlled by a PID controller coupled with a type K thermocouple. We found the lightbulb to be much more efficient for maintaing the elevated temperatures and it was very stable as we could run tests for many hours without worrying about the bulb burning out during a test run.

A copper plate was used as the gate electrode to which the lead from Keithley was attached by an alligator clip. To prevent loss of contract due to thermal oxidation of the copper plate, we used indium contact the copper plate and the sample under testing, this would ensure oxidation of the copper plate would not have an impact on the testing of the samples.

Micromanipulators were used with fine tip probes (Micromanipulator Company) allowing us to make electrical contact to the source and drain pads on the substrate. A

Keithley 2400 source-measurement unit integrated with a custom made Labview program was used for obtaining electrical measurements of the samples under test.

4.2.1 Thermal oxidation of ebeam deposited titanium films

TiO_2 films fabricated by thermal oxidation of ebeam deposited titanium were fabricated as shown in Figure **??**. We first begin with a degenerately doped p++ Silicon wafer that acts as the gate electrode. The silicon wafer wet thermally oxidized at 800 °C to yield a thermal oxide of approximately 300 nm. The thermal oxide was sufficiently thick to avoid any excessive leakage current during any applied gate potentials and was very stable with the thermal processes used in the fabrication of the thin films.

Upon the growth of the gate oxide, the samples were cleaned in acetone, isopropanol, followed by rinse in DI water. The substrates were then baked at 170 °C for approximately 5 minutes. LOL 2000 was spun at 2.5 krpm for 30 seconds followed by baking at 170 °C for an additional 5 minutes to yield 100 nm layer. For the lift off layer (LOL 2000), it's very critical to keep an eye on the baking times as the development and desired undercut of the lift off layer after exposure is very sensitive to the temperature of the baking time as well as the length. We found that 170 °C for 5 minutes with our recipe was ideal although lower baking temperatures can be used in case of possible surface reactivity or substrate compatibility. We considered the possibility that the LOL 2000 or the photoresist would in some way impact the performance or functionality of the devices since we are baking the exposed surfaces with an organic layer at relatively high temperatures. However, we ran a few experiments where we fabricated devices by use of photolithographic defined features and devices where we used a hard mask to deposit features. Both devices performed similarily, therefore, we determined the exposure of the active layer would be negligibly affected by the photoresist or the LOL 2000 in

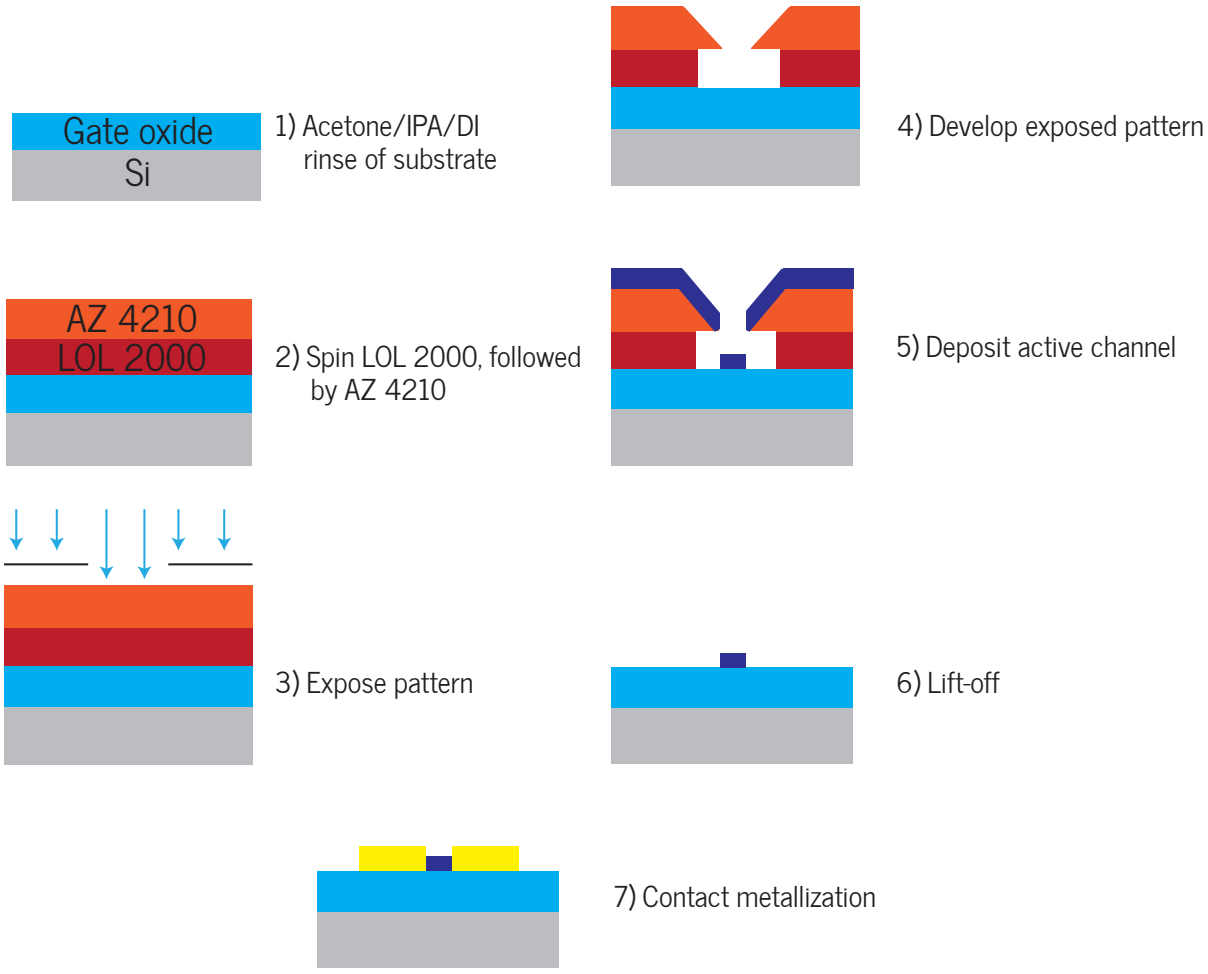

Figure 4.10: Polymer based photoresist used for defining features on the substrate using standard recipes developed at UCSB.

anyway. Also, when using LOL 2000, due to its low viscosity, the layer will appear to be visibly nonuniform throughout the surface, however, we determined through ellipsometry that the layer thickness did not vary significantly throughout a 1x1 cm sample. More importantly, we obtained consistent layer thicknesses in the middle of the sample, where the active area and probing contacts would be placed.

After applying the liftoff layer, we spun AZ 4210 photoresist at 4 krpm for 30 seconds, yielding a layer thickness of approximately 2 microns. We had difficulties measuring the layer thickness of the photoresist with ellipsometry, primarily due to the strongly absorbing nature of the resist, but layer thickness was confirmed independenty by a Michael Belt.

Samples were then baked at 90°C for one minute. The features for the active layer were then defined by contact lithography exposing for 13 seconds at 7.5 mW/cm_2 power. Samples were then developed in 1:4 MIBK:DI developer for 2 minutes and 15 seconds. The longer development time was required to appropriately etch the LOL 2000 layer to provide an ideal undercut for liftoff after active layer deposition, as shown schematically in Figure 4.10.

Titanium was deposited using ebeam evaporation (Temescal). Evaporation was held at a constant rate of 0.1 Å/s until the desired thickness of 15 nm was achieved. Following depositon of the titanium layer, the photoresist and LOL 2000 were removed by soaking the sample overnight in Nanostrip, a commercial solvent used for lifting off resists.

Once liftoff was achieved, the samples were removed from the Nanostrip and rinsed with copious amounts of isopropanol followed by a final DI water rinse. To remove any residual impurities, the samples were cleaned in a UV-ozone chamber for 10 minutes. Although this cleaning method will slightly oxidize the due to the high reactivity of titanium, we determined the extent of oxidation would negligibly effect the overall properties of the film after we perform the thermal oxidation.

After confirming the features on the substrates, the samples were placed in a tube furnace and annealed overnight at 500 °C in open atmosphere. We determined 16 hours annealing time was sufficient to obtain the desired conductivity although longer annealing times would of course further oxidize the film and cause a decrease in the conductivity. Ellipsometry was used to approximate the layer thickness of the TiO_2 upon thermal oxidation and we determined the film to be approximately 25 nm in thickness.

Ti/Au (10/1000 Å) ohmic contacts were deposited onto the active channel. Ohmic properties were confirmed by performing Id-Vd sweeps using the probe station in the nanofab.

Samples were then taken to the testing chamber, shown schematically in Figure 4.8.

Before testing, the sample was annealed in the probe station under vacuum for approximately 12 hours at 150 °C followed by 1 hour of UV (254 nm wavelength) exposure with 25 sccm (standard cubic centimeter) of argon. Since our samples are surface sensitive, these two cleaning techniques allow us to clean the sample of any residual solvent or surface contaminants introduced during previous steps.

UV exposure has been shown to excite electron-hole pairs in the film, that then react with organic or other contaminants on the surface to remove the material. [51] Typically after UV treatment, the number of oxygen vacancies tend to increase due to the removal of impurities at the oxygen vacancy site, thus increasing the measured current for at a constant voltage. UV treatment also yielded higher mobilities and lower 'off' currents due to the removal of the impurities.

Heating the sample for 12 hours also removes any weakly bounded water molecules that may be coordinated to the oxide surface. Along with the UV light, this also allows for removal of any residual materials.

After the treating the sample for contaminants we obtained voltage sweeps from 60 to 200 °C, Figure 4.11. This was done to confirm the semiconducting properties of the TiO_2

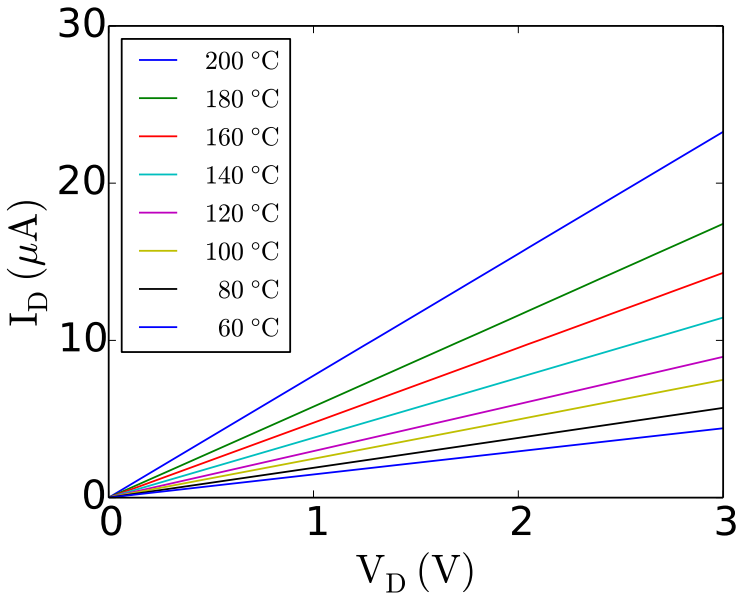

Figure 4.11: ID-VD of thermally oxidized electron beam evaporated titanium films showing ohmic and semiconducting properties.

film since the conductivity is exponentially dependent on the temperature, $I_D \propto e^{\frac{1}{kT}}$. Although not shown here, we performed an arrhenius fit to the current vs temperature plot by extracting current values at a particular voltage which allowed us to determine an approximate value for the position of the donor levels within the band gap of TiO_2. We obtained a value of approximately 0.21 eV, indicating that the donor levels reside predominantely 0.21 eV below the conduction band of TiO_2.

The samples demonstrated great stability, even at elevated temperatures, with leakage current approximately in the nano ampere range, acceptable for our measured currents here. Although we did find that the current-voltage characteristics could vary from the beginning to the end of the day at 200 °C, we attribute this to residual oxygen and water in our testing chamber that could very easily coordinate within the oxygen vacancy sites and alter the conductivity. It would become more obvious when no argon flow was used, further necessitating the use of the background argon flow to set as a baseline for testing.

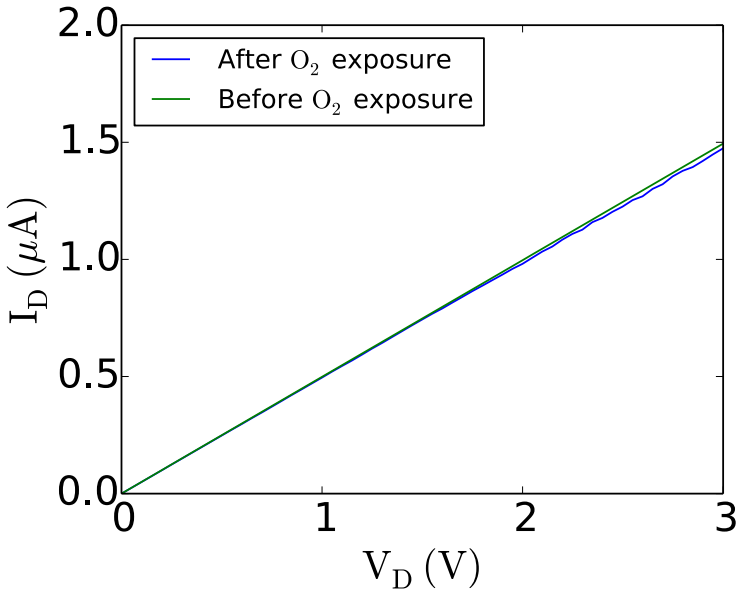

Figure 4.12: Room temperature voltage sweep before and after oxygen exposure at room temperature.

For the sensing experiments, we first measured the response of 10 sccm oxygen at room temperature, Figure 4.12, with background flow of 25 sccm argon. As the current-voltage measurement indicates, we observed no response to oxygen at room temperature since oxygen is not expected to appreciably react with the oxide surface at room temperature and yield a measureable change in current. [52]

After confirming that we are not observing any unusual response to the oxygen exposure, we first measured the response of our sample to various oxygen flows at 150 °C, Figure 4.13.

This temperature was chosen since it has been shown that oxygen readily reacts with the oxide surface at 150 °Cas the oxygen will react with the oxygen vacancies found at the surface of the oxide. At sufficiently elevated temperatures, the oxygen will adsorb to the surface of the oxygen by various mechanisms illustrated by Figure **??**.

Typically, at temperatures from 100 to 550 °C, oxygen will ionosorb as molecular

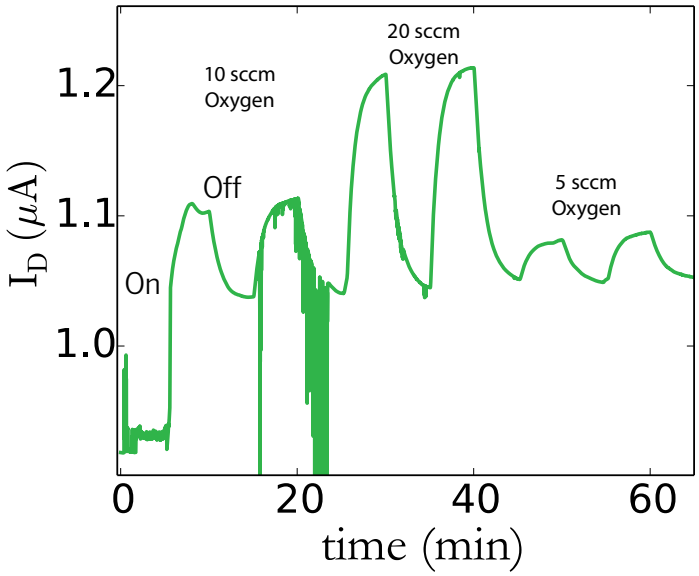

Figure 4.13: Oxygen response at 150 °C, noise in measurement was due to the probe vibrating from the gas flows and was eliminated by simply adjusting the probe position.

and atomic species, shown in Figure **??**. These species, as mentioned before, will either react with oxygen vacancies or will furth lead to a depletion fregion at the layer of the oxide, thus causing a decrease in the conductivity leading to a measureable response in the conductivity of the sample. The reactivity can be written as follows:

$$\frac{\beta}{2}O_2^{gas} + \alpha \cdot e^- + S \rightleftharpoons O_{\beta S}^{-\alpha} \tag{4.1}$$

where O_2^{gas} is the oxygen molecule, e^- is a free electron which can react with molecules, S is an unoccupied site for oxygen reactivity which are typically surface oxygen vacancies and other surface defects, $O_{\beta S}^{-\alpha}$ is a chemisorbed species where,

- $\alpha = 1$ for singly ionized forms
- $\alpha = 2$ for doubly ionized forms

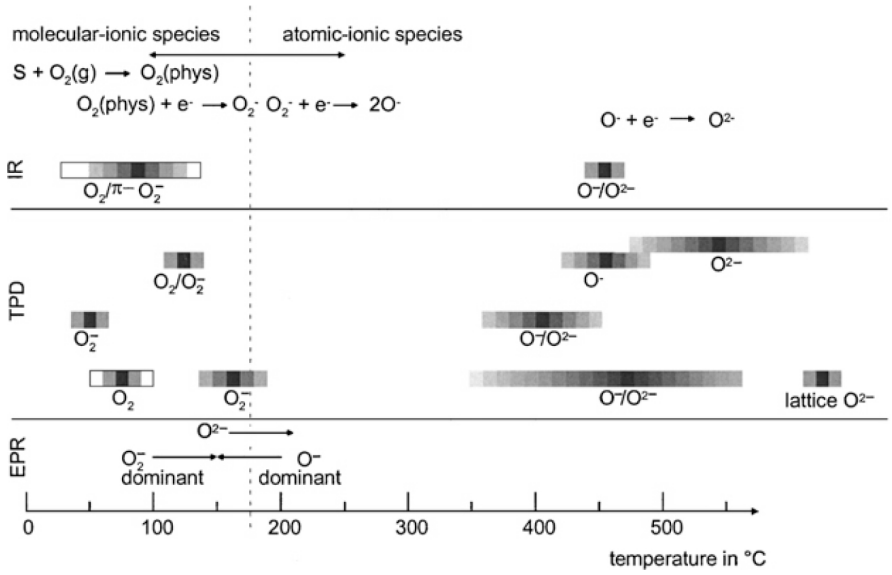

Figure 4.14: Oxygen species detected at different temperatures on oxide surface by use of infrared analysis (IR), temperature programmed desorption (TPD), and electron paramagnetic resonance (EPR). Adapted from [53].

- $\beta = 1$ for atomic forms
- $\beta = 2$ for molecular forms.

As is readily described in the literature, the chemisorption of oxygen is a process that involves both a chemical and electronic process. However, since the TiO_2 surface has essentially unlimited electrons (relative to molecules that can possibly absorb), the limiting factor is the chemical process of adsorption, hence the requirement of elevated temperatures to allow oxygen to adsorb to the surface.

However, even with the extensive research performed with oxide materials and their reactivities with oxygen indicating that the oxygen should lead to a decrease in the conductivity of the metal oxide, we instead observe the opposite, Figure 4.13. Initially, when we first obtained these results, we believed that we were observing some sort of error in our measurement. Therefore, we carefully revisted our fabrication procedure to determine if we were introducing any contaminates unintentionally.

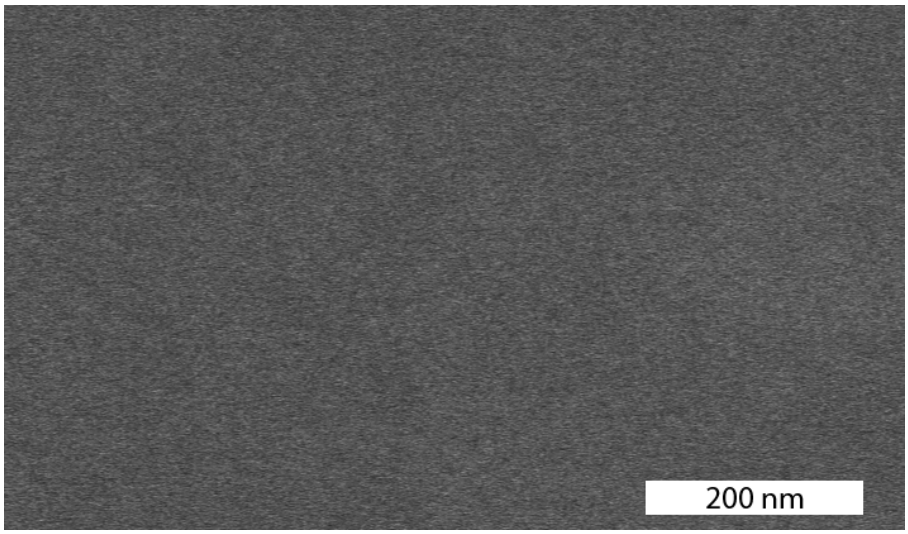

Figure 4.15: Scanning electron micrograph of oxidized titanium film before addition of contact pads.

As mentioned during device fabrication, we believed at some point that we were leaving residual photoresist or some other organic residue that was then reacting with the oxygen at elevated temperatures leading to an increase in conductivity. In particular, we soaked a few of the samples in various organic solvents over night and remeasured their oxygen sensing properties after extensive cleaning with UV ozone as well as elevated temperatures. We found however, there was no significant difference in the response towards oxygen from one set of films to another.

With bare metal oxides at elevated temperatures, ethylene gas will react with oxygen species on the oxide surface to form ethylene oxide, as was also observed for our films, Figure 4.16. [54] Ethylene, a reducing gas towards metal oxide films, yielded appropriate responses for our device system. As expected, we observed an increase in the conductivity of the thin film due to the ethylene reacting with various surface oxygen species that then allowed for a donation of an electron to the metal oxide film, yielding an increase in the conductivity of the system.

This of course still doesn't address our question as to why the film behaves normally

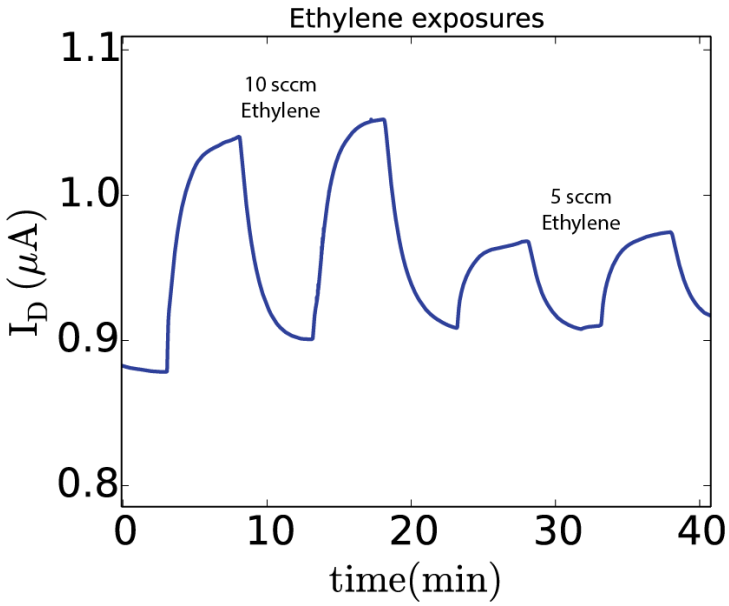

Figure 4.16: Response of thermally oxidized titanium films towards 10 and 5 sccm ethylene exposures with a constant background flow of 25 sccm argon at 150 °C.

with ethylene but not with oxygen. Although our film is approximately 25 nm in thickness of TiO_2, we didn't expect that this would lead to any significant differences in the behavior of the films towards the gases. We attempted to deposit thicker layers of titanium, followed by oxidation, but we could not obtain uniform samples as we noticed significant lack of uniformity after thermally oxidizing when trying to oxidize titanium layers greater than 50 nm. Therefore, we fabricated atomic layer deposited films for comparison to the oxidized titanium films.

4.2.2 Atomic layer deposited TiO_2 films

ALD is a monolayer-by-monolayer deposition technique that allows for a set of chemical precursors to be sequentially introduced into a reaction chamber containing the substrate. The precurors are designed to not react with each other only until they are introduced into the reaction chamber and react on the substrate through a cyclic

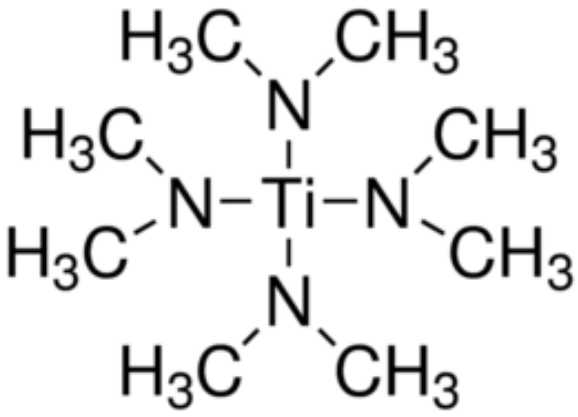

Figure 4.17: Tetrakis(dimethylamino)titanium precursor used for ALD deposition of TiO_2.

fashion. When properly designed, the film will grow one monolayer per cycle that allows for precise control of the final film thickness by simply varying the total number of deposition cycles. TiO_2 films were fabricated from atomic layer deposition from tetrakis(dimethylamino)titanium ($C_8H_{24}N_4Ti$), TDMAT) the titanium source and water served as the oxidaant, Figure 4.17. [55]The ALD recipe for our instrument (Oxford Instruments) was characterized and developed by Bill Mitchell. Growth rates were measured to be 0.6 Å/cycle at 300 °C, confirmed by ellipsometry.

The as-deposited films are of rutile / anatase mixture, with exact composition unknown since we were not able to obtain a clear XRD pattern to confirm the composition. We choose to deposit at 300 °C as we wanted to obtain dense films without causing significant damage to the gate oxide due to incorporated stress from the deposited films. However, prior studies suggested that depositing at this temperature would increase carbon and nitrogen contamination within the film. Although we have no reason to believe the incorporated carbon and nitrogen would contribute significantly to the performance of the thin films, we none the less took this into consideration for our analysis and post treatment of the films.

We deposited 333 cycles with the precursors was performed, yielding a total layer

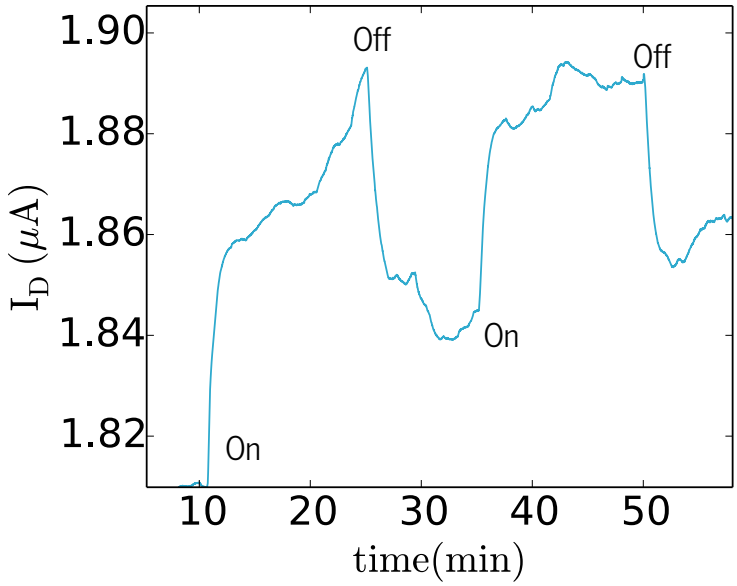

Figure 4.18: Response of 20 nm ALD deposited TiO_2 films towards 5 sccm oxygen.

thickness of 20 nm of TiO_2. For the ALD films, we did not define the active areas for the deposition of the TiO_2 films due to the conformal coverage of the deposition process which would significantly increase the difficulty of achieving a clean lift off. Therefore, we simply used a hard mask to cover the edges of the silicon wafers and allowed the film to cover all exposed areas. Contact pads of Ti/Au (100/1000 Å) were deposited using the similar process as for the oxidized titanium films, Figure 4.10.

As-deposited ALD films of TiO_2 were tested for their oxygen response, Figure 4.18 and 4.19. As with the thermally oxidized films of titanium, we obtained an increase in current for the devices when exposing oxygen gas with background argon flow. Once again contradicting prior observed oxygen responses for the films.

We considered the possibility of film contamination within the ALD films, since the film is fabricated from metallorganic precursors. We therefore annealed as-deposited films at various temperatures ranging from 300-500 °C for 1 hour in nitrogen atmosphere. For

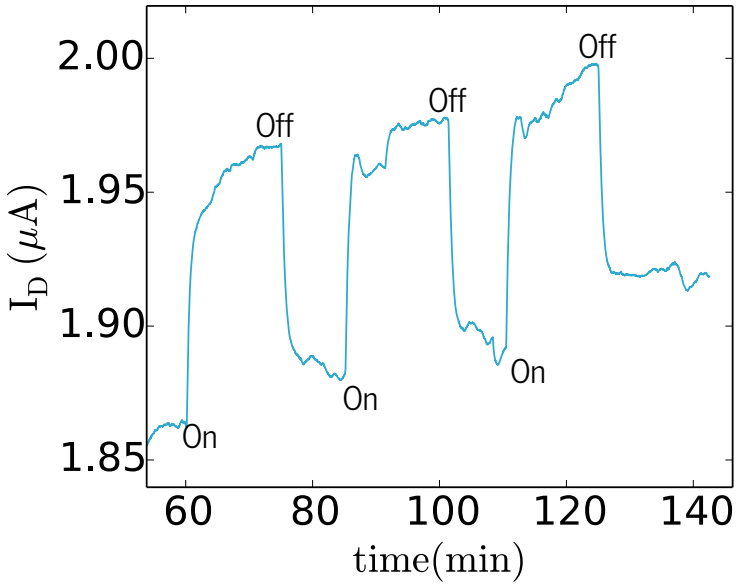

Figure 4.19: Response of ALD deposited TiO_2 films towards 10 sccm oxygen.

all the samples, we measured a decrease in the conductivity, but still observed the same response towards oxgyen. As a reducing gas, we then used hydrogen to probe the surface reactivity and observed the expected increase in conductivity for the sample.

To determine whether the ALD films were behaving electronically similar to the thermal oxidized titanium films we obtained temperature dependent current-voltage sweeps. A quick introduction behind the reason for such a measurement is given below.

The conductivity of a semiconductor is given by the following relation

$$\sigma = q(\mu_n n + \mu_p p) \tag{4.2}$$

where μ_n and μ_p refer to the mobilities of electrons and holes and n and p refer to density of electrons and holes. Because TiO_2 is an n-type material, where $n >> p$, we can simplify conductivity as $\sigma \propto n$.

In general, the intrinsic concentration of a semiconductor increases with increasing

temperature, as described by the following equation:

$$n_i(T) = 2\left[\frac{2\pi kT}{h^2}\right]^{\frac{3}{2}}\left(m_n^* m_p^*\right)^{\frac{3}{4}}\exp\left[\frac{-E_g}{2kT}\right] \tag{4.3}$$

In this equation, the exponential temperature dependence dominates the intrinsic concentration (n_i).

While this equation holds valid for the intrinsic carriers of semiconductor, it is necessary to determine the total carrier concentration (following space-charge neutrality) by the following expressions:

$$n(T) = N_D^+(T) - N_A^-(T) + \frac{n_i^2(T)}{n(T)} \quad \textbf{and} \quad p(T) = N_A^-(T) - N_D^+(T) + \frac{n_i^2(T)}{p(T)} \tag{4.4}$$

where $N_D^+(T)$ is the number of ionized donors and $N_A^-(T)$ is the number of ionized acceptors.

At sufficiently high temperatures, the level of the donors can be determined by plotting $\ln(\sigma) vs. \frac{1}{T}$, which will yield a slope equal to $-\frac{E_g}{2k}$. Therefore, by measuring conductivity at sufficiently high temperatures where dopant contribution to carrier density is minimized, the level of carrier density of the material can be determined, Figure 4.20.

The donor levels of the ALD deposited TiO_2 films are similar to those we obtained for the oxidized titanium films, showing similar electronic properties with regards to the donor levels from the oxygen vacancies. After exhaustively attempting various cleaning and postdeposition parameters, we determined that the increase in current due to oxygen exposure is in fact a real phenomenon we are measuring and not simply an accident. We are limited in the layer thickness of TiO_2 we can deposit using ALD as the nanofab staff does not allow us to grow significantly thicker films due to the expensive TDMAT precursor preventing us from performing thickness dependent measurements.

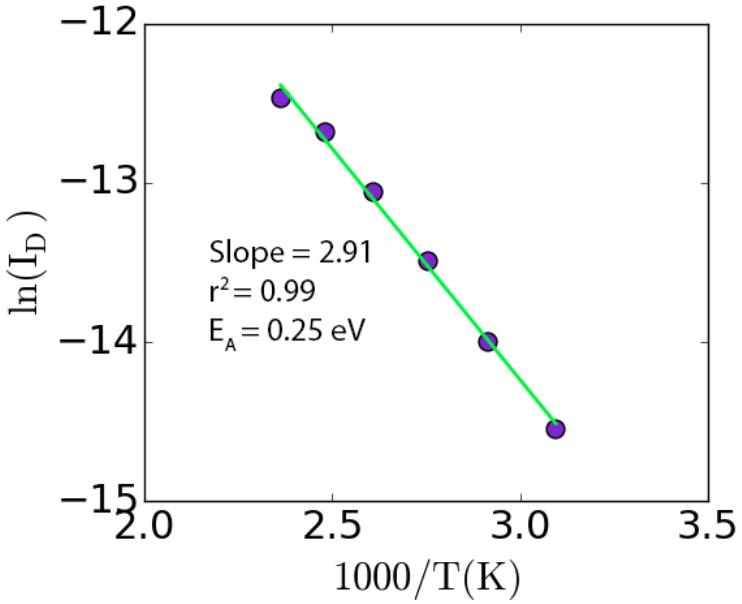

Figure 4.20: Arrhenius fit for conductivity of ALD films obtained at various temperatures with 1 V applied bias.

4.2.3 Sputter deposited TiO_2 films

Reactive ion sputtering is a widely used technique to produce thin films. By using the same titanium target, it is possible to obtain oxide, TiO_2 and nitride, TiN, films by simply changing the deposition atmosphere from oxygen to nitrogen although a compound target (TiO_2 or TiN) can also be used for depositing films. Sputtering also allows one to control the substrate temperature of the sample during deposition as substrate temperature has been shown to significantly impact the resulting crystallinity and surface morphology of the film. [28, 56, 57]

The sputter tool (AJA International ATC 2000-F) in the UCSB nanofab is a six target tool that is capable of handling both DC and RF sputtering. Ultimate base pressure of approximately 9.8 x 10^{-8} torr can be achieved. The system is setup with an adaptive pressure control that allows one to precisely adjust the chamber pressure without having to alter the mass flows of the gases. In our system, argon is used as the sputter gas with

Table 4.1: Example recipe used for depositing TiO_2 films on AJA International ATC 2000-F sputter system in the UCSB nanofab.

Power (Watts)	200
Oxygen flow (sccm)	3.0
Argon flow (sccm)	30
Pressure (mTorr)	2
Substrate height	25
Gun tilt	9
Feedback voltage	434
Deposition time (s)	600
Thickness (nm)	56
Rate (nm/min)	5.6
Refractive index @ 633 nm	2.4

nitrogen and oxygen gas available for depositing both nitrides and oxides. The tool also has a substrate heating element allowing for samples to be heated up to 800 °Cduring depositions.

The recipe shown in Table 4.1 was developed after we spent some time calibrating the recipe to obtain a proper deposition rate and desired conductivity. The as-deposited film from this recipe yielded conductivity in the microamp range with the same lithographic procedure illustrated in Figure 4.10.

Since we could control substrate temperature during the deposition on the sputter tool, we studied the response of films deposited at various temperatures towards hydrogen and oxygen, since depositing at various temperatures would favor the formation of mixed phases or rutile phase at elevated temperatures. [48, 58] Since all the films yielded the same trends with response, we only show the set for a sample deposited at 400 °C.

Films shown here are of 20 nm layer thickness, confirmed by ellipsometry with an index of refraction approximately 2.4 at 633 nm wavelength. As was observed for the ALD deposited and thermally oxidized films, we observed the expected response of the films towards hydrogen gas. The response of the films exhibits a sudden increase in the conductivity followed by a plateau effect.

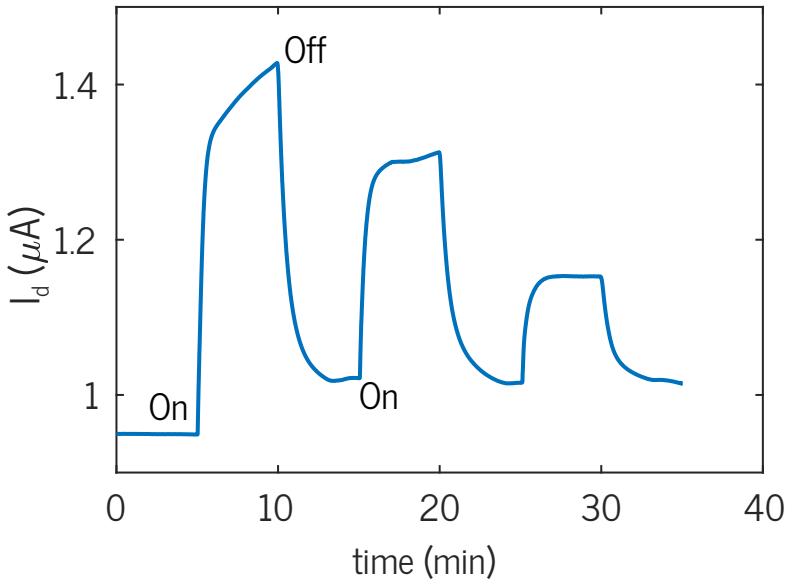

Figure 4.21: 20 nm layer thickness TiO_2 film behaving as expected in reducing conditions with 10,5, 2.5 sccm hydrogen gas at 120 °C.

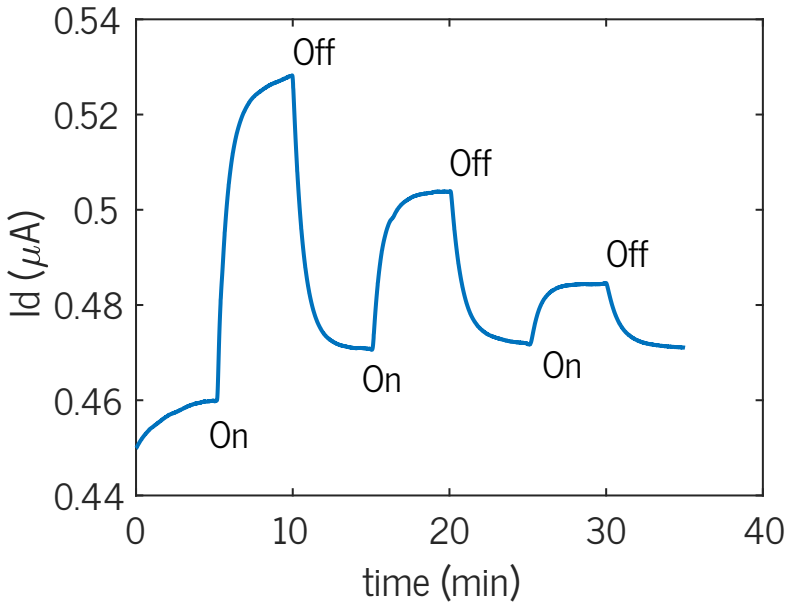

Figure 4.22: 20 nm layer thickness sputter deposited TiO_2 film exhibit unusual behavior towards oxygen flows of 15,10, and 5 sccm at 120 °C.

The oxygen response for these films, exhibited increses in conductivity once again after exposing the films to various concentrations of oxygen. These responses are very reproducible from sample to sample and we have tried various methods for ensuring they are clean before gas testing.

Suprisingly, all the films, whether sputter deposited at room temperature or 400 °C, showed similar reponses to oxygen and hydrogen for layer thicknesses of 20 nm. Our observations, which indicates that oxygen is reducing the TiO_2 surface simply contradicts essentially all of the literature studies regarding the oxidation of TiO_2 surfaces. Of course, we were skeptical throughout all of our samples when we observed this for all of our films. However, we event went as far as changing the oxygen cyclinder and reconfiguring the gas lines leading to the testing chamber. My wonderful undergrads, Chris and Sam, spent countless hours testing a wide range of samples with various deposition and post processing parameters, but we continued to observe the same trends with respect to hydrogen and oxygen response.

To suggest that both hydrogen and oxygen are reducing the TiO_2 surface is something that defies all logic regarding surface science. So with this in mind we had to ask ourselves, is this in fact a chemical property? Or there is another effect we have not considered?

One possibility we proposed may be affecting the response of the films is the use of the thermally grown SiO_2 as the gate oxide. While we have no real reason to believe this is in fact the culprit, we have no other evidence that would suggest otherwise. We assume the TiO_2 and SiO_2 surface are behaving ideally, but with such thin films of TiO_2 there's always a possibility something may in fact be affected by the substrate. Therefore, we fabricated devices with Al_2O_3 and Si_3N_4 gate insulators. However, we observed the same responses towards hydrogen and oxygen even when using other gate dielectric. With these experiments, we've eliminated the possibility of the substrate having an influence on the response of the films.

Next, we consider the layer thickness of TiO_2 being used. Although the ability to precisely deposited layers down to tens of nanometers has yielded significant improvement for the performance of transistors and other electronic devices, there have not been significant reactivity studies of such films since the development of nanowire and nanobelt 1-D materials. These materials have unprecedented responses and sensitivities towards gases due to their nanostructured properties which has caused research in thin film based sensors to significantly decrease.

As mentioned in the prior sections, we were limited to smaller layer thicknesses due to growth restrictions on the ALD and due to the lack of uniformity with thicker layers of oxidized titanium films. However, sputtering is capable of yielding growths on the order of microns. Although the nanofab at UCSB typically asks users to not exceed depositions longer than 12 hours, we can easily obtain thicker films within this time frame since our deposition rates are typically on the order of 6 nm/min.

By using the recipe shown in Table 4.1, we deposited films of TiO_2 approximately 100 nm layer thickness onto silicon wafers with 300 nm thermal oxide. Same lithographic procedure for defining the contact pads as used for the previous samples was used for the source and drain contacts.

The film's response towards oxygen is shown in Figure 4.23. The relatively thick layer of TiO_2 (100 nm layer thickness), exhibited a decrease in conductivity when exposed to an oxidizing atmosphere, precisely what should be expected for oxide materials. Hydrogen exhibited its usual reducing behavior towards the same film where the increase in conductivity can be seen towards the end of the oxygen testing in Figure **??**.

Since the 100 nm thick sputtered film is exhibiting 'normal' responses towards oxidizing and reducing gases this of course begs the question as to whether the change in response towards an oxidizing environment is due to the ultrathin properties of the film. Due to the difficulty of obtaining proper glancing XRD patterns that would indicate the

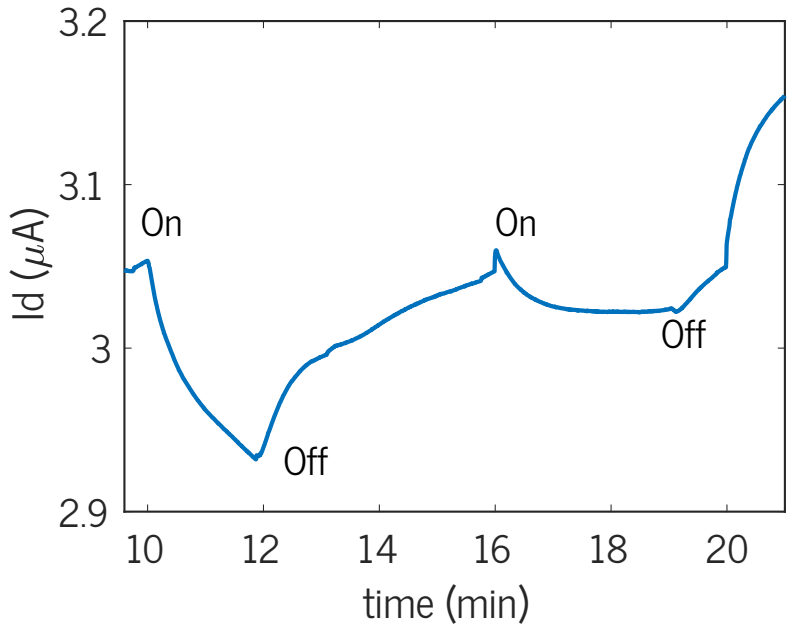

Figure 4.23: 100 nm thick sputter TiO_2sample exhibiting as expected response to an oxidizing atmosphere with 10 sccm mass flow of oxygen.

phase and strucutre of the ultrathin TiO_2 films, we decided to probe to electronic properties by finally fabricating a proper FET using the sputter oxide for the active channel. Because we were interested in testing the properties of films deposited at temperatures up to 400 °C, we were forced to develop a novel method for patterning substrates since traditional photolithographic techniques could not be used for fabricating such patterns. Here, we briefly show a hard mask technique we developed that was based on a similar method. [59]

High-vacumm depositions have been extensively used for depositing high quality, pure, and tunable materials. Examples such as sputter deposition, physical enhanced chemical vapor deposition, and electron beam assissted deposition quite often employ depositing material at elevated substrate temperature in order to achieve a particular crystalline phase or purity. Although operating at elevated substrate temperature ranges offers many benefits, such techniques are not practical when considering the delicate

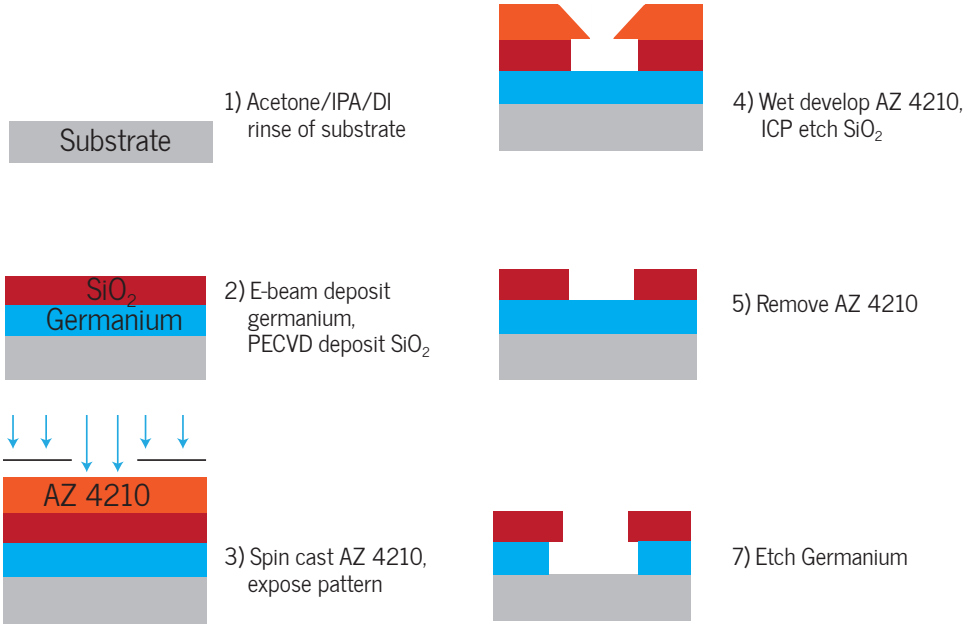

Figure 4.24: Hard mask method allowing for depositings of materials at temperatures up to 600 °C without causing diminishing the resolution of the features. Note that features used in this dissertation were significantly large, generally greater than 25 microns, smaller feature sizes were not tested.

surface of the substrate and the limited lithography techniques available for patterning at elevated operating temperatures.

In our process, we demonstrate a versatile hard-mask layer that will replace traditional photoresist lithographic processes for use in sputter deposition of various materials at substrate temperatures up to 400 °C. Due to the structural damage caused by high energy ions during sputtering, incorporation of atomic layer deposition (ALD) will be used towards protecting the substrate from extensive structural damage. This will be demonstrated by applying our method towards fabricating a back-gated thin film TiO_2 transistor with an active channel deposited at elevated substrate temperatures.

The germanium silicon nitride bi-layer mask was fabricated by a combination of PECVD and e-beam deposition techniques. The working substrate was composed of 40 nm Al_2O_3 dielectric deposited on a (100) p^{++}-Si wafer by atomic layer deposition. The

alumina layer served as the gate dielectric layer when operating the device as a back-gated FET. To ensure minimized leakage current and increase the quality of the dielectric material, the as-deposited Al_2O_3 film was annealed at 600°C in flowing nitrogen for 3 minutes. 200 nm of germanium was deposited by e-beam evaporation (base pressure of 3×10^{-6}) followed by deposition of 50 nm SiO_2 by PECVD. No post-deposition treatment was performed to the Ge and SiO_2 layers. Depositing at higher rates caused very uniform etching of the germanium, therefore, we determined depositing the germanium layer at 2.0 Å/s would yield the most consistent etch rates.

Contact lithography was used to define the areas for deposition of the active channel onto the Ge/SiO_2 bi-layer using UV photolithographic techniques. The pattern from the resist to the substrate was transferred by ICP etching of the SiO_2 with CHF_3 with minimal etching of Ge. Following removal of the photoresist after pattern transfer to the substrate, the exposed Ge was then etched with 30 % H_2O_2 at 50 °C for approximately 5 minutes. Undercut of the bi-layer was confirmed with an optical microscope.

Upon deposition of the active channel, the samples were lifted off overnight in room temperature 30% H_2O_2 and rinsed with DI water. Contact lithography was used to define contact pad features followed by Ti/Au (20/2000 Å) e-beam deposition for the contact pads. Samples were then cleaned in a UV-ozone environment to remove any residual contaminations from the surface of the TiO_2 film.

Charge transfer measurements (Id-Vg) for 20 nm layer thickness samples sputter deposited at 400 °C were obtained at both room temperature and at 150 °C, Figure 4.25 and Figure 4.26, respectively. The charge transfer measurements indicated n-type conductivity (electrons are major charge carriers), which agrees with the accepted models for charge transfers of TiO_2 films. There was no significant change in the electronic properties from room temperature to 150 °C, except for a slight change in the saturation current and threshold voltage, which is expected for elevated temperatures.

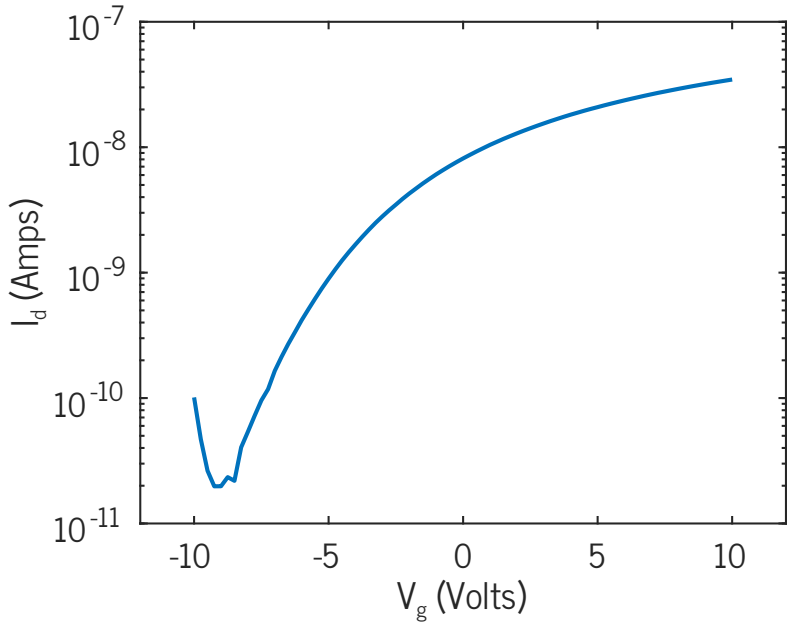

Figure 4.25: Room temperature transfer characteristics of the TiO_2 film deposited at 400 °C. The film exhibited n-type characteristics as expected for TiO_2 thin films.

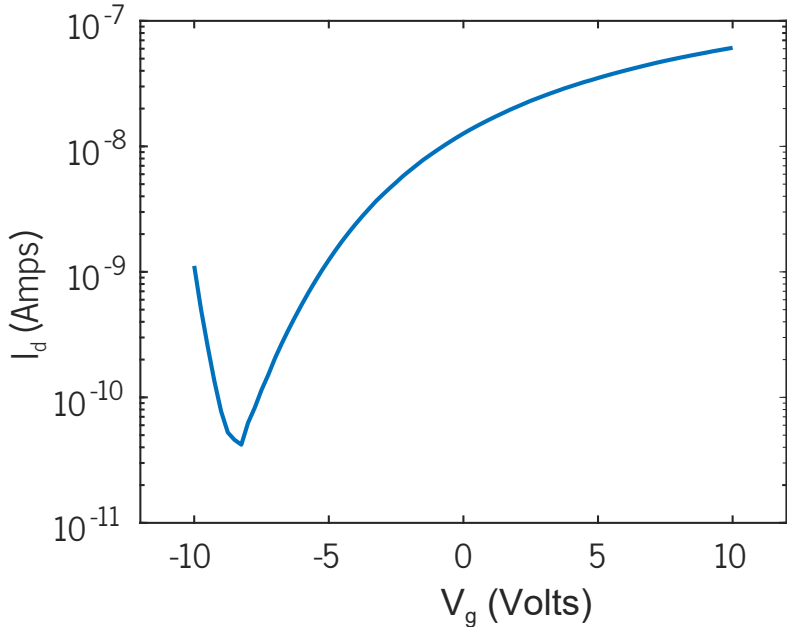

Figure 4.26: Transfer characteristics obtained at 150 °C for 20 nm layer thickness TiO_2 sample deposited by sputtering.

The charge transfer measurements confirmed to us that the ultrathin films are behaving as n-type materials, which would eliminate the possiblity of accidentally p-type behavior due to excess oxygen incorporated into the film. [45] Therefore, we cannot attribute some sort of mechanism where the ultrathin films are altering their electronic properties.

4.3 Future work and conclusions

Although we did not reach our goal to develop a gate-tunable heterogenous catalytic platform, we have encountered an interesting observation where both oxygen and hydrogen are reducing the TiO_2 surface for films ranging of layer thickness from 15-30 nm. We demonstrated these effect was observed for thermally oxidized titanium films, atomic layer deposited, and sputter deposited TiO_2 films.

We determined the response towards oxygen gas does not change its properties even with postprocessing of deposited films, suggesting the crystallinity of the film is not significantly impacting its behavior towards oxygen. Furthermore, we show that a 100 nm layer thickness film of sputter deposited TiO_2 exhibits its expected behavior when exposed to oxygen, thus leading us to believe that layer thickness of the film is somehow the major contributor towards its behavior with oxygen. Electronically, the ultrathin films exhibit normal n-type behavior, as expected for TiO_2 thereby eliminating the possiblity of any kind of anomolous electronic behavior at such low layer thicknesses.

Moving forward, we would need to perform a thorough evaluation on the TiO_2 films. For example, we could use XPS to probe the nature of the titanium coordination within the film. Also, we have primarily been assuming the response of the film has been due to a chemical interaction at the surface. While very unlikely, it could be possible that somehow the oxygen incorporates itself at the grain boundaries of the TiO_2 layer that

then allows for an improve electronic pathway for conductivity. While this is not very likely, due to the precise response of the films towards the various concentrations oxygen, it could somehow be a contributing factor.

Appendix A

Bulk metal optical constants

The optical constants for the bulk metals were fitting the following equation to optical constants provided by the references listed:

$$\epsilon(\omega) = 1 - \frac{\omega_p^2}{\omega^2 + i\omega\gamma} + \sum_j^N \frac{a_j}{\omega_{0j}^2 - \omega^2 - i\omega\Gamma_j} + \epsilon_\infty \tag{A.1}$$

A.1 Gold optical constants

Equation A.1 was used to fit the optical constant data provided by Johnson and Christy. [30]

Table A.1: Values resulting from least squares fit using 3 lorentzian oscillators and drude contribution, the following parameters were held **constant**: $\omega_p = 9.1\ eV$ and $\gamma = 0.0757\ eV$, however, ϵ_∞ was a free variable and was determine to be 4.308.

$j =$	1	2	3
a_j	-21.74	71.37	75.52
ω_{0j}	-2.06	-5.65	3.33
Γ_j	1.92	5.83	4.03

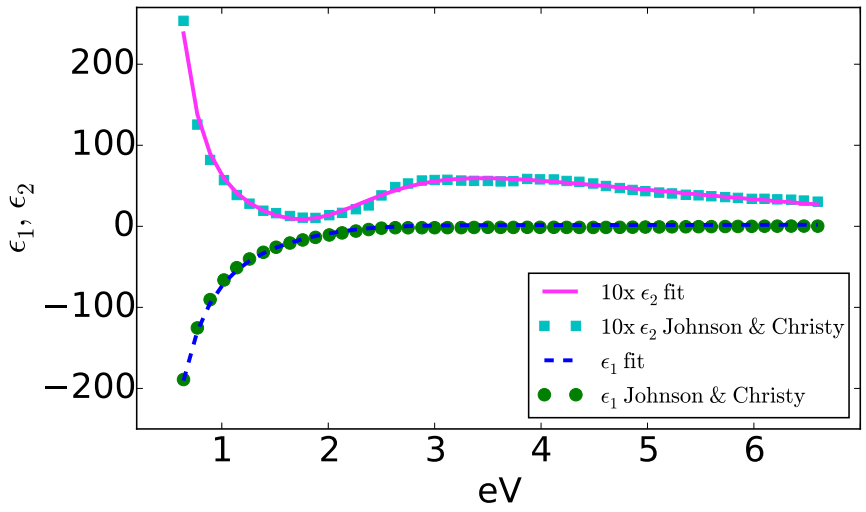

A.2 Silver optical constants

Silver optical constants were obtained from Johnson and Christy. [30]

Table A.2: Values resulting from least squares fit using 3 lorentzian oscillators and drude contribution, the following parameters were also found: $\omega_p = 9.18\ eV$ and $\gamma = 0.020\ eV$, and $\epsilon_\infty = 2.10$.

$j =$	1	2	3
a_j	48.315	-70.9657	75.6473
ω_{0j}	5.6449	4.1692	4.225
Γ_j	3.0219	1.195	1.1713

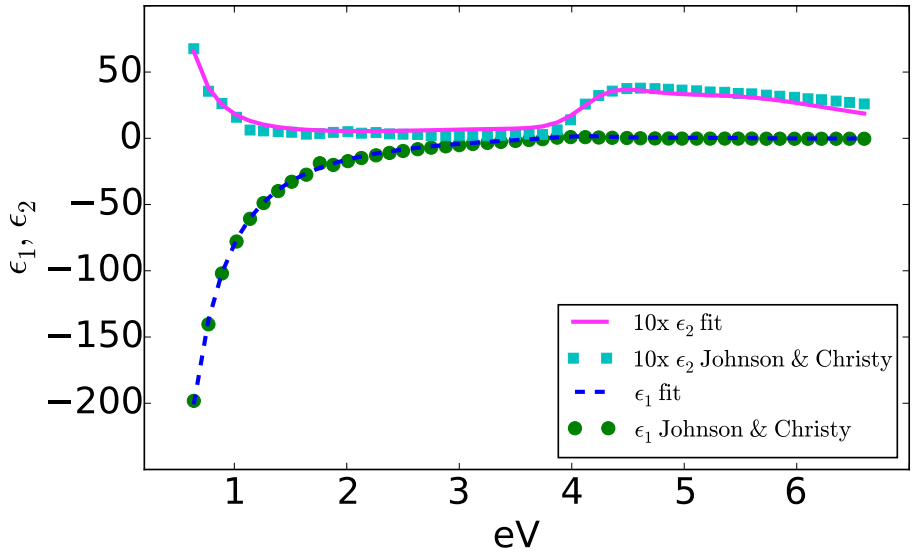

A.3 Aluminum optical constants

Optical constants were obtained from Rakic and Aleksandar. [60]

Table A.3: Values resulting from least squares fit using 3 lorentzian oscillators and drude contribution, the following parameters were also found: $\omega_p = 15.1\ eV$ and $\gamma = 0.605\ eV$, and $\epsilon_\infty = -22.34$.

$j =$	1	2	3
a_j	57.18	-849.436	-1464.88
ω_{0j}	1.5802	-0.6647	2.236
Γ_j	0.7617	3.848	-10.028

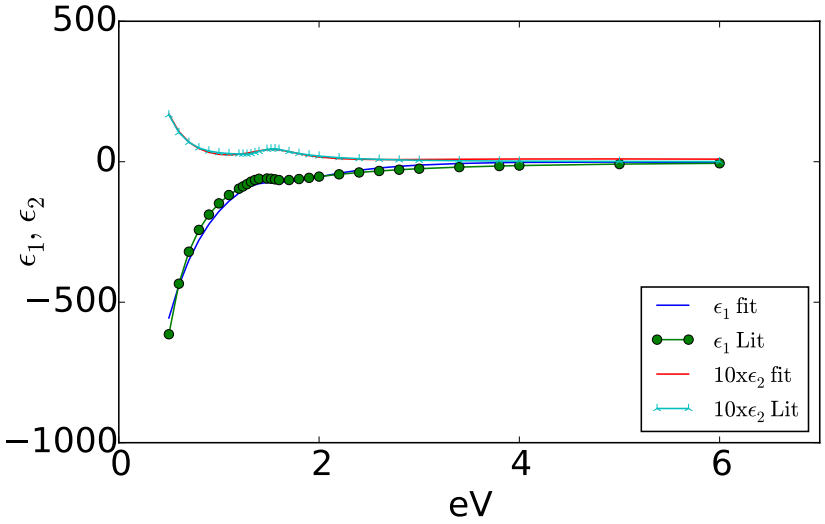
500
0
−500
−1000
0
2
4
6
eV
ϵ_1, ϵ_2
ϵ_1 fit
ϵ_1 Lit
10xϵ_2 fit
10xϵ_2 Lit

Bibliography

[1] C. Kittel, *Solid State Physics*. John Wiley & Songs, Inc., New York, 6th ed., 1986.

[2] P. Mulvaney, *Surface Plasmon Spectroscopy of Nanosized Metal Particles*, *Langmuir* **12** (1996), no. 3 788–800.

[3] M. C. Daniel and D. Astruc, *Gold Nanoparticles: Assembly, Supramolecular Chemistry, Quantum-Size-Related Properties, and Applications Toward Biology, Catalysis, and Nanotechnology*, *Chemical Reviews* **104** (2004), no. 1 293–346, [0403600v1].

[4] S. Link and M. A. El-Sayed, *Spectral Properties and Relaxation Dynamics of Surface Plasmon Electronic Oscillations in Gold and Silver Nanodots and Nanorods*, *The Journal of Physical Chemistry B* **103** (October, 1999) 8410–8426.

[5] P. V. Kamat, *Photophysical, Photochemical and Photocatalytic Aspects of Metal Nanoparticles*, *The Journal of Physical Chemistry B* **106** (August, 2002) 7729–7744.

[6] S. Underwood and P. Mulvaney, *Effect of the Solution Refractive Index on the Color of Gold Colloids*, *Langmuir* **10** (1994), no. 3 3427–3430.

[7] C. Novo, A. M. Funston, A. K. Gooding, and P. Mulvaney, *Electrochemical Charging of Single Gold Nanorods*, .

[8] A. M. Brown, M. T. Sheldon, and H. A. Atwater, *Electrochemical tuning of the dielectric function of Au nanoparticles*, *ACS Photonics* **2** (2015), no. 4 459–464.

[9] A. Marimuthu, J. Zhang, and S. Linic, *Tuning selectivity in propylene epoxidation by plasmon mediated photo-switching of Cu oxidation state.*, *Science* **339** (2013), no. 6127 1590–1593.

[10] M. Moskovits, *Surface-enhanced spectroscopy*, *Reviews of Modern Physics* **57** (July, 1985) 783.

[11] S. Mubeen, J. Lee, W. Lee, N. Singh, G. D. Stucky, and M. Moskovits, *On the Plasmonic Photovoltaic*, *ACS Nano* **8** (June, 2014) 6066–6073.

[12] H. A. Atwater and A. Polman, *Plasmonics for improved photovoltaic devices*, *Nature Materials* **9** (feb, 2010) 205–213.

[13] M. T. Sheldon, J. van de Groep, A. M. Brown, A. Polman, H. A. Atwater, J. V. D. Groep, and A. M. Brown, *Nanophotonics. Plasmoelectric potentials in metal nanostructures.*, *Science (New York, N.Y.)* **346** (nov, 2014) 828–31.

[14] Z. Zhang and J. T. Yates, *Band Bending in Semiconductors: Chemical and Physical Consequences at Surfaces and Interfaces*, *Chemical Reviews* **112** (oct, 2012) 5520–5551.

[15] V. P. Zhdanov, *Nm-sized Metal Particles on a Semiconductor Surface, Schottky model, etc.*, *Surface Science* **512** (jun, 2002) L331–L334.

[16] T. Ioannides and X. E. Verykios, *Charge transfer in metal catalysts supported on doped TiO2: A theoretical approach based on metal-semiconductor contact theory*, *Journal of Catalysis* **161** (1996), no. 2 560–569.

[17] Y. Zhang, O. Pluchery, L. Caillard, A.-F. Lamic-Humblot, S. Casale, Y. J. Chabal, and M. Salmeron, *Sensing the Charge State of Single Gold Nanoparticles via Work Function Measurements*, *Nano Letters* **15** (2015), no. 1 51–55.

[18] O. Schalm and M. Schreiner, *The colour of silver stained glass analytical investigations carried out with XRF , SEM / EDX ,*, *Journal of Analytical Atomic Spectrometry* **17** (2002) 321–328.

[19] J. C. Maxwell Garnett, *Colours in Metal Glasses and in Metallic Films*, *Philosophical Transactions of the Royal Society of London Series A* **203** (1904) 385–420.

[20] H. Lorentz, *Relation between propagation of light and density of matter*, *Wiedem. Ann., volume=9, number=4, pages=641, year=1880.*

[21] L. Lorenz *Wiedem. Ann.* **11** (1880), no. 4 70.

[22] M. Born and E. Wolf, *Principles of Optics*. The MacMillan Company, New York, second edi ed., 1964.

[23] C. A. Foss, M. J. Tierney, and C. R. Martin, *Template Synthesis of Infrared-Transparent Metal Microcylinders : Comparison of Optical Properties with the Predictions of Effective Medium Theory*, .

[24] C. A. Foss, G. L. Hornyak, J. A. Stockert, and C. R. Martin, *Optical-properties of composite membranes containing arrays of nanoscopic gold cylinders*, *Journal of Physical Chemistry* **96** (1992), no. 19 7497–7499.

[25] A. Incel, T. Güner, O. Parlak, and M. M. Demir, *Null Extinction of Ceria@silica Hybrid Particles: Transparent Polystyrene Composites*, *ACS Applied Materials and Interfaces* **7** (2015), no. 49 27539–27546.

[26] S. Mubeen and M. Moskovits, *Gate-Tunable Surface Processes on a Single-Nanowire Field-Effect Transistor*, *Advanced Materials* **23** (may, 2011) 2306–2312.

[27] Z. Shao, X. Wang, S. Ren, Z. Tian, S. Fan, S. Sun, S. Liu, and Q. Wang, *Improved visible solar absorber based on TiO2 nanotube film by surface-loading of plasmonic Au nanoparticles*, *Journal of Applied Physics* **114** (2013), no. 6 063510.

[28] D. Mardare, M. Tasca, M. Delibas, and G. Rusu, *On the structural properties and optical transmittance of TiO₂ r.f. sputtered thin films*, *Applied Surface Science* **156** (oct, 1999) 200–206.

[29] W. Cai and V. Shalaev, *Optical metamaterials: Fundamentals and applications*. 2010.

[30] P. B. Johnson and R.-W. Christy, *Optical constants of the noble metals*, *Physical review B* **6** (1972), no. 12 4370.

[31] L. A. Coldren, S. Corzine, and M. Mshanovitch, *Diode Lasers and Photonic Integrated Circuits*. John Wiley & Sons, Hoboken, N.J., second edi ed., 2012.

[32] A. Zangwill, *Modern Electrodynamics*. Modern Electrodynamics. Cambridge University Press, 2013.

[33] J. Lowell, *Tunnelling between metals and insulators and its role in contact electrification*, *Journal of Physics D: Applied Physics* **12** (1979), no. 9 1541–1554.

[34] J. Lowell, *Contact electrification of metals*, *Journal of Physics D: Applied Physics* **8** (1975), no. 1 53.

[35] C. Clavero, *Plasmon-induced hot-electron generation at nanoparticle/metal-oxide interfaces for photovoltaic and photocatalytic devices*, *Nature Photonics* **8** (jan, 2014) 95–103.

[36] S. Mubeen, G. Hernandez-Sosa, D. Moses, J. Lee, and M. Moskovits, *Plasmonic Photosensitization of a Wide Band Gap Semiconductor: Converting Plasmons to Charge Carriers*, *Nano Letters* **11** (dec, 2011) 5548–5552.

[37] R. Chapman and P. Mulvaney, *Electro-optical shifts in silver nanoparticle films*, *Chemical Physics Letters* **349** (2001), no. 5-6 358–362.

[38] O. D. Häberlen, S.-C. Chung, M. Stener, and N. Rösch, *From clusters to bulk: A relativistic density functional investigation on a series of gold clusters Aun, n=6,...,147*, *The Journal of Chemical Physics* **106** (1997), no. 12 5189–5201.

[39] N. Holmberg, K. Laasonen, and P. Peljo, *Charge distribution and Fermi level in bimetallic nanoparticles*, *Phys. Chem. Chem. Phys.* **18** (2016), no. 4 2924–2931.

[40] P. Peljo, J. A. Manzanares, and H. H. Girault, *Contact Potentials, Fermi Level Equilibration, and Surface Charging*, *Langmuir* **32** (2016), no. 23 5765–5775.

[41] Sze, *Physics of Semiconductor Devices Physics of Semiconductor Devices*, vol. 10. John Wiley & Sons, third ed., 1995.

[42] K. D. Schierbaum, U. Weimar, W. Göpel, and R. Kowalkowski, *Conductance, work function and catalytic activity of SnO2-based gas sensors*, *Sensors and Actuators: B. Chemical* **3** (1991), no. 3 205–214.

[43] C. Wang, L. Yin, L. Zhang, D. Xiang, and R. Gao, *Metal Oxide Gas Sensors: Sensitivity and Influencing Factors*, *Sensors* **10** (mar, 2010) 2088–2106.

[44] M. S. Arnold, P. Avouris, Z. W. Pan, and Z. L. Wang, *Field-Effect Transistors Based on Single Semiconducting Oxide Nanobelts*, *The Journal of Physical Chemistry B* **107** (jan, 2003) 659–663.

[45] A. T. Iancu, M. Logar, J. Park, and F. B. Prinz, *Atomic layer deposition of undoped TiO2 exhibiting p -type conductivity*, *ACS Applied Materials and Interfaces* **7** (2015), no. 9 5134–5140.

[46] E. Wahlström, E. K. Vestergaard, R. Schaub, A. Rønnau, M. Vestergaard, E. L\a egsgaard, I. Stensgaard, and F. Besenbacher, *Electron transfer-induced dynamics of oxygen molecules on the TiO2 (110) surface*, *Science* **303** (2004), no. 5657 511–513.

[47] I. Nakamura, N. Negishi, S. Kutsuna, T. Ihara, S. Sugihara, and K. Takeuchi, *Role of oxygen vacancy in the plasma-treated TiO2 photocatalyst with visible light activity for NO removal*, *Journal of Molecular Catalysis A: Chemical* **161** (2000), no. 1 205–212.

[48] S. Dutta, Leeladhar, A. Pandey, O. P. Thakur, and R. Pal, *Electrical properties of ultrathin titanium dioxide films on silicon*, *Journal of Vacuum Science & Technology A: Vacuum, Surfaces, and Films* **33** (mar, 2015) 021507.

[49] M. E. Franke, T. J. Koplin, and U. Simon, *Metal and metal oxide nanoparticles in chemiresistors: Does the nanoscale matter?*, *Small* **2** (2006), no. 1 36–50.

[50] Y. Zhang, A. Kolmakov, S. Chretien, H. Metiu, and M. Moskovits, *Control of Catalytic Reactions at the Surface of a Metal Oxide Nanowire by Manipulating Electron Density Inside It*, *Nano Letters* **4** (mar, 2004) 403–407.

[51] H. Y. Chong and T. W. Kim, *Electrical Characteristics of Thin-Film Transistors Fabricated Utilizing a UV/Ozone-Treated TiO2 Channel Layer*, *Journal of Electronic Materials* **42** (dec, 2012) 398–402.

[52] H. F. Lu, F. Li, G. Liu, Z.-G. Chen, D.-W. Wang, H.-T. Fang, G. Q. Lu, Z. H. Jiang, and H.-M. Cheng, *Amorphous TiO 2 nanotube arrays for low-temperature oxygen sensors*, *Nanotechnology* **19** (oct, 2008) 405504.

[53] N. Barsan and U. Weimar, *Conduction model of metal oxide gas sensors*, *Journal of Electroceramics* **7** (2001), no. 3 143–167.

[54] J. M. Baik, M. Zielke, M. H. Kim, K. L. Turner, A. M. Wodtke, and M. Moskovits, *Tin-Oxide-Nanowire-Based Electronic Nose Using Heterogeneous Catalysis as a Functionalization Strategy*, *ACS Nano* **4** (jun, 2010) 3117–3122.

[55] B. Abendroth, T. Moebus, S. Rentrop, R. Strohmeyer, M. Vinnichenko, T. Weling, H. Stöcker, and D. C. Meyer, *Atomic layer deposition of TiO2 from tetrakis(dimethylamino)titanium and H2O*, *Thin Solid Films* **545** (oct, 2013) 176–182.

[56] S. Berg, T. Larsson, C. Nender, and H.-O. Blom, *Predicting thin-film stoichiometry in reactive sputtering*, *Journal of Applied Physics* **63** (1988), no. 3 887.

[57] W. Shih, S. Young, L. Ji, W. Water, T. Meen, K. Lam, J. Sheen, and W. Chu, *Thin film transistors based on TiO2 fabricated by using radio-frequency magnetron sputtering*, *Journal of Physics and Chemistry of Solids* **71** (dec, 2010) 1760–1762.

[58] D. Wicaksana, *Process effects on structural properties of TiO2 thin films by reactive sputtering*, *Journal of Vacuum Science & Technology A: Vacuum, Surfaces, and Films* **10** (jul, 1992) 1479.

[59] D. J. Meyer, D. A. Deen, B. P. Downey, D. S. Katzer, D. F. Storm, and S. C. Binari, *SiN/Ge Lift-off: a method for patterning films deposited at high temperature*, 2013.

[60] A. D. Rakić, *Algorithm for the determination of intrinsic optical constants of metal films: application to aluminum*, *Applied Optics* **34** (1995), no. 22 4755.